Individual and collective motility in microbial systems : bacterial biofilms and fungal spore dispersal

Martina Iapichino

▶ **To cite this version:**

Martina Iapichino. Individual and collective motility in microbial systems : bacterial biofilms and fungal spore dispersal. Biomechanics [physics.med-ph]. Université Côte d'Azur, 2019. English. NNT : 2019AZUR4051 . tel-02613384

HAL Id: tel-02613384
https://theses.hal.science/tel-02613384

Submitted on 20 May 2020

HAL is a multi-disciplinary open access archive for the deposit and dissemination of scientific research documents, whether they are published or not. The documents may come from teaching and research institutions in France or abroad, or from public or private research centers.

L'archive ouverte pluridisciplinaire **HAL**, est destinée au dépôt et à la diffusion de documents scientifiques de niveau recherche, publiés ou non, émanant des établissements d'enseignement et de recherche français ou étrangers, des laboratoires publics ou privés.

UNIVERSITÉ CÔTE D'AZUR

ÉCOLE DOCTORALE
SCIENCES FONDAMENTALES ET APPLIQUÉES

THÈSE DE DOCTORAT

Motilité individuelle et collective chez les systèmes microbiens : biofilms bactériens et dispersion de spores fongiques / Individual and collective motility in microbial systems : bacterial biofilms and fungal spore dispersal

---

Martina IAPICHINO

Institut de Physique de Nice UMR 7010

Présentée en vue de l'obtention du grade de docteur en Physique d'Université Côte d'Azur
Dirigée par : Dr. Agnese SEMINARA
Soutenue le : 25/07/2019

Devant le jury, composé de :
Dr. Fabien HALKETT, INRA
Dr. Nelly HENRY, CNRS
Dr. Sigolène LECUYER, CNRS
Prof. Anne PRINGLE, UW-Madison
Dr. Eric RASPAUD, CNRS
Prof. Magali RIBOT, Université d'Orléans
Dr. Agnese SEMINARA, CNRS
Dr.Philippe THOMEN, UCA

Motilité individuelle et collective chez les systèmes microbiens : biofilms bactériens et dispersion de spores fongiques / Individual and collective motility in microbial systems : bacterial biofilms and fungal spore dispersal

Jury:

Rapporteurs:

Nelly Henry, Directrice de recherche, CNRS, Université Pierre et Marie Curie

Eric Raspaud, Directeur de recherche, CNRS, Université Paris Sud

Examinateurs:

Fabien Halkett, Chargé de recherche, INRA, Université de Lorraine

Sigolène Lecuyer, Chargée de recherche, CNRS, ENS de Lyon

Anne Pringle, Professeur des Universités, University of Wisconsin-Madison

Magali Ribot, Professeur des Universités, Université d'Orléans

Agnese Seminara, Chargée de recherche, CNRS, Université Côte d'Azur

Philippe Thomen, Maitre de Conference, Université Côte d'Azur

Résumé et mots clés

Motilité individuelle et collective chez les systèmes microbiens : biofilms bactériens et dispersion de spores fongiques

Le but de cette thèse est de développer des expériences pour comprendre la physique de la motilité dans deux systèmes microbiens, évoluant dans le domaine du faible nombre de Reynolds, c'est-à-dire lorsque les forces visqueuses l'emportent sur les forces d'inertie. La première partie de la thèse traite de la croissance de biofilms bactériens sur une surface solide. Les biofilms bactériens sont des communautés de cellules étroitement empilées dans une matrice polymère. Du point de vue physique, ces colonies se comportent comme des gels et la matrice polymérique crée des flux osmotiques qui permettent aux biofilms de se développer et de se déplacer sur une surface en tant que communauté. Ici, je développe une expérience pour explorer la motilité collective des biofilms au contact de gradients externes de pression osmotique. Pour produire des gradients osmotiques stables dans des gels d'agar, je développe une configuration sur mesure au moyen de techniques de millifluidique. Les biofilms répondent au gradient externe en développant une forme asymétrique, conforme aux attentes. La deuxième partie de la thèse aborde le mécanisme de décharge des spores chez les basidiomycètes à phylum fongique. Chez ces espèces, une goutte coalesce avec la spore, ce qui entraîne son écoulement à des accélérations énormes. Cette catapulte à tension superficielle atteint son efficacité maximale lorsque la taille de la goutte est comparable à celle de la spore. J'étudie les morphologies de plusieurs champignons branchiaux, où les spores sont conditionnées à la surface de branchies complexes. Je trouve que pour ces espèces, si les spores sont emballées au maximum comme il est généralement supposé, la taille de la goutte qui coalesce avec la spore doit être bien contrôlée. Cela pose la question de comment est-ce que le champignon peut contrôler un processus purement extracellulaire, face aux fluctuations environnementales.

Mots clés: biofilm bactérien, gradient de pression osmotique, millifluidique, champignons, décharge des spores, biomécanique

Abstract and keywords

Individual and collective motility in microbial systems : bacterial biofilms and fungal spore dispersal

The aim of this thesis is to develop experiments to understand the physics of motility in two microbial systems, moving in the realm of low Reynolds number, i.e. when viscous forces dominate over inertial forces. The first part of the thesis discusses the growth of bacterial biofilms over a solid surface. Bacterial biofilms are communities of cells closely packed together inside a polymeric matrix. From the physical viewpoint, these colonies behave as gels and the polymeric matrix creates osmotic fluxes that enable biofilms to grow and move on a surface as a community. Here I develop an experiment to explore biofilm collective motility in contact with external gradients of osmotic pressure. To produce stable osmotic gradients in agar gels, I develop a custom-made setup through millifluidics. Biofilms respond to the external gradient by developing an asymmetric shape, consistent with the expectations. The second part of the thesis discusses the spore discharge mechanism in the fungal phylum Basidiomycetes. In these species, a drop coalesces with the spore, which results in spore discharge at enormous accelerations. This surface tension catapult reaches its maximum efficiency when the size of the drop is comparable to that of the spore. I study morphologies of several gilled mushrooms, where spores are packaged at the surface of complex shaped gills. I find that for those species, drop size must be precisely controlled. This poses the question of how mushrooms may regulate a process that occurs extracellularly, despite fluctuating physical conditions.

Keywords: Bacterial biofilm, osmotic pressure gradient, millifluidics, Fungi, spore discharge, biomechanics.

Declaration of Authorship

I, Martina IAPICHINO, declare that this thesis titled "Motilité individuelle et collective chez les systèmes microbiens : biofilms bactériens et dispersion de spores fongiques / Individual and collective motility in microbial systems : bacterial biofilms and fungal spore dispersal" and the work presented in it are my own. I confirm that:

- This work was done wholly or mainly while in candidature for a research degree at this University.
- Where any part of this thesis has previously been submitted for a degree or any other qualification at this University or any other institution, this has been clearly stated.
- Where I have consulted the published work of others, this is always clearly attributed.
- Where I have quoted from the work of others, the source is always given. With the exception of such quotations, this thesis is entirely my own work.
- I have acknowledged all main sources of help.
- Where the thesis is based on work done by myself jointly with others, I have made clear exactly what was done by others and what I have contributed myself.

Acknowledgements

I've often been told that the responsibility of a successful PhD project relies on the PhD candidate. It may be true, but I would not be here today without receiving help from a lot of people who have been taking this journey with me for the last almost four years years. Here I would like to thank those who contributed and helped me reaching this result.

The Ministère de l'Enseignement supérieur, de la Recherche et de l'Innovation, for funding my PhD scholarship during the first three years; the Global Health Institute, for partially funding my project in Madison, and the Université Côte d'Azur, for funding the last nine months of my PhD.

The members of my committee Dr. Fabien HALKETT, Dr. Nelly HENRY, Dr. Sigolène LECUYER, Prof. Anne PRINGLE, Dr. Eric RASPAUD and Prof. Magali RIBOT for taking the time of reading and evaluating my thesis and to come to Nice to evaluate my defense.

The former director of my institute, Dr. Fabrice Mortessagne, for accepting me as a PhD student at the ex Laboratoire de la Matière Condensée, and the current director of the Institut de Physique de Nice, Dr. Guillaume Huyet. Despite being very busy people, you have always been very nice and open-minded with the students of the institute.

Dr. Agnese Seminara, my thesis director, for accepting me as your PhD student, for teaching me whatever you knew when I arrived here and for always taking the time to discuss with me whenever I had doubts or insecurities. If I reached this goal today it's mainly thanks to you and I can not forget all the times you encouraged me to see what I had achieved, despite my perfectionist (and sometimes disruptive) attitude.

Dr. Philippe Thomen, for helping me with the development of my experiments and for always giving me useful advises since your arrival at the beginning of the third year of my PhD, for taking the time to explaining things to me whenever I was stuck with some experimental issue.

Dr. Robert Arkowitz and Dr. Martine Bassilana, for hosting me in your biology lab during these three years of my PhD and for allowing me to use your equipment and material.

Prof. Anne Pringle, whenever I was visiting you in Madison you took me around with you in the woods around USA, you showed me a totally new side of science that I had never thought I would have explored and liked. The enthusiasm and kindness your show with your students and in every aspect of your life are something that I will never forget, together with the very nice moments I shared with you and your students during our field trips.

Danny Weng and Savannah Gentry, from the Pringle Lab, for dedicating part of your time to run experiments for me and helping me with my results and for your human qualities.

Drs. Xavier Noblin, Celine Cohen, Yann Bouret, Quang Tran Duc and Nicolas Bruot, the senior members of my team, for sharing their knowledge and time with me.

Greg Sauder, for developing the Labview program that controlled my setup. It worked so well I never had to come to you and ask for help about it.

Yaroslava Izmalov, for being a wonderful chemistry lab manager, teaching me how to use a lot of equipment and giving me a lot of suggestions. Your pedagogic way to explain things is a gift and you always found a way to make me see the funny side of things.

Last, but not least in my collaborators list, Dr. Cyrille Claudet and Stephanie Bogliolo, for being my mentors in the physics and biology experimental room, respectively. Cyrille, I know how busy you are, but you always took the time to help me and make whatever thing I asked you to do. I cannot count how many times your suggestions made this project advance, especially at the beginning of my PhD when I didn't know where to put my hands on. Stephanie, I know a couple of times I made you nervous for leaving stuff around the lab and not cleaning up my tubes, but you have always been very patient and kind to me, offering me your help and being an unlimited and precious source of useful tips.

In the InPhyNi, there are a lot of other people I worked with who deserve a thank you, even though they were not directly involved in my project.

Elizabeth Lemaire, for lending me the reflex camera I used for some of my images.

Christophe Raufaste, for lending me part of his lab spaces, some equipment that I used during the experiments and for being a very nice person to work and to teach with.

Ulrich Ulle, for being the calmest person I know, always helpful and supportive with the students and with whom I had the pleasure to teach as well.

Marie Gabrielle Medici and Frederic Blanc, for being very nice professors to assist during my TPs.

Denise Sidler and Madalena Neri, the administration managers of my team who helped me with whatever mission order and money refund I needed, together with all the other lovely secretaries Nathalie Koulechoff, Magali Varlet-Dusaucy, Christine Boudard-Morteau and Christine Chassagneaux.

Bernard Gay-Para and Jerome Mauro, the IT technicians, for saving my computer and my data several times and helping me with whatever informatics problem I had along my PhD.

There are also a lot of other people that deserve a huge thank you:

My office mates and friends I have met during these three years: Sihem Bounoua Nahed, Nino Kukhaleishvili, Julian Böhm, Martin Richter, Florent Mazeas and Khalid Oubaha; other PhDs, post-docs and students of the InPhyNi, of the IBV and of the Pringle lab: Chiara Scognamiglio, Panos Vergyris, Bruno Fedrici, Florian Kaiser, Guido Schifani, Dorian Oser, Djeylan Atkas, Emanuel Vermillac, Angela Guttila, Nicola Rigolli, Xin Hua, Francois Mondain, Elie Gouzien, Omar Boughdad, Enzo D'Ambrosio, Floriane Brunel, Pierrick Charlier, Nadia Formicola, Patricia Silva, Miguel Basante, Nora Duncritts, Daniel Levitis. Permanents of the InPhyNi: Sebastien Tanzilli, Florent Doutre, Claire Michel. With most of you, the relationship wasn't simply the one you have between colleagues, during these three years and half we shared a lot of very nice moments inside and outside of the lab, sometimes also outside of Nice and some of you were for me some kind of family during my three years and eight months in Nice.

Contents

List of Figures

Introduction

The aim of my thesis is to develop experiments to understand the physics of motility in two microbial systems, living in the realm of low Reynolds number. All biological systems live in a physical environment that influences their development. Fluids can bring information through chemical signals, or shape biological behavior transporting nutrients.

The Reynolds number is a dimensionless quantity that gives the ratio of inertial forces to viscous forces for different flow conditions and it is defined as:

$$\mathrm{Re} = \frac{\text{intertial forces}}{\text{viscous forces}} = \frac{\rho U L}{\mu} = \frac{U L}{\nu}$$

where ρ is the density of the fluid, U is the fluid velocity, L is the characteristic length of the body immersed in the fluid, μ and ν are the dynamic and the kinematic viscosity of the fluid, respectively. At low Reynolds numbers, viscous forces dominate and the flow is laminar (i.e. smooth); whereas if Reynolds number is high, inertial forces dominate and the flow is turbulent.

To give an idea of the order of magnitude of the Reynolds number in different system and how parameters change Re, I will give the example of a man, a goldfish and a bacterium swimming in water. At 20 °C, water has dynamic viscosity of $\mu \simeq 10^{-3}$ Pa $\cdot$ s and density $\rho \simeq 10^{3}$ kg/m^3. If we consider a 1.80m tall man who can swim at $U = 1.8$ m/s (World record for 50 m freestyle is 2.31 m/s), its Reynolds number is about $\mathrm{Re} \simeq 3.24 \cdot 10^{6}$. For a goldfish, $L \simeq 10^{-1}$ m and $U \simeq 0.3$ m/s [23] and the resulting $\mathrm{Re} \simeq 3 \cdot 10^{4}$. Finally, for a bacterium, $L \simeq 3 \cdot 10^{-6}$ m and $U \simeq 3 \cdot 10^{-5}$ m/s [117], giving $\mathrm{Re} \simeq 9 \cdot 10^{-5}$. Consequently, for a man to have the same Reynolds number as a bacterium, he should swim in water with a velocity of less than 1 Å/s, or try to swim in asphalt. More generally, when a body moves very slowly, or it is very small, or the viscosity of the fluid is very high, $\mathrm{Re} \to 0$. In this case, the inertial forces of the Navier-Stokes equation can be neglected.

In the limit of small Re, viscous drag and diffusion dominate. Forces exerted on the swimmer will not depend on time, and motion depends only on the forces exerted on the swimmer at a given instant. As soon as applied forces cease, motion ceases as well. If the bacterium we previously mentioned stops

moving, it will travel only 0.1 $\dot{A}$ in 0.6 μs before stopping [117]. But very small particles can experience high Reynolds number as well, for example fungal spores are ejected from the mushroom and are quickly brought to rest by drag, like a balloon that is thrown in the air. Their Reynolds number changes depending on the species, ranging from 0.1 to about 170 [38]. But later in time they are carried away from their source by strong and fast winds in the atmosphere where $\mathrm{Re} = 10^9$. A single bacterium swims with $\mathrm{Re} \simeq 9 \cdot 10^{-5}$, but bacteria expanding in colonies can reach $Re \simeq 1$.

During my thesis, I investigated the collective translocation of bacterial biofilms on a gradient of osmotic pressure and the spore discharge mechanism in the fungal phylum of basidiomycota. Bacterial biofilms are composed by both metabolically active cells and dormant cells [83], whereas spores are metabolically dormant with the potential to be reactivated. These are two very different biological systems, but they are both micron size particles (see Fig. 1A,D) and their Reynolds number is small, hence in both situations the fluid motion around them can be approximated by Stokes equation. As an experimentalist, my work consisted mainly in combining micro and millifluidics, microscopy and data analysis.

My manuscript is divided in two parts. In the first part I will discuss my main project, focusing on bacterial biofilm expansion over a gradient of osmotic pressure. This project took two thirds of my PhD thesis and was run in collaboration with the Arkowitz team at Institut de Biologie Valrose (Nice) and with Cyrille Claudet and Philippe Thomen from InPhyNi (Nice). For this project, I developed the experimental setup using micro and millifluidic techniques, I performed the wet lab experiments and I organized and analyzed the data-set. The main question was if a gradient of osmotic pressure can affect biofilm growth and, if yes, how. My experiments show that biofilms respond to the osmotic gradient by developing an asymmetrical shape. Biofilms initially expand slightly toward the osmotic gradient, but eventually translocate against the osmotic gradient (see Fig. 1C). We know from previous results that biofilms translocate toward or against external osmotic gradients depending on the relative importance of three effects. (i) The external osmotic pressure modulates the conditions for equilibrium. This effect causes the bulk of the biofilm to expand quicker *toward* the external osmotic gradient [129]. (ii) At the same time, biofilms produce more matrix at low osmotic pressure, where growth rate is larger. This effect pushes the biofilm *against* the osmotic gradient at initial stages as well as at late ones [129]. (iii) At late stages, gradients in the wetting properties of the substrate may also be relevant [153]. My results

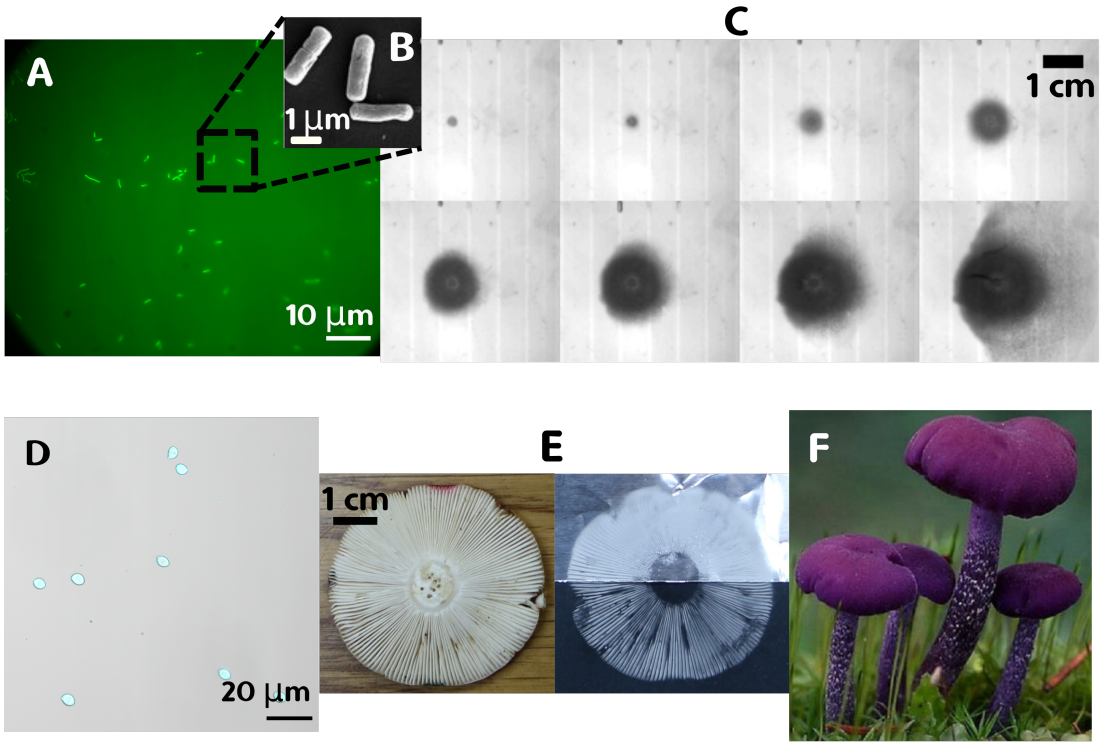

FIGURE 1: Top row: (A) microscope image of *Bacillus subtilis* cells labeled with GFP. Taken by Charlie Puerner at IBV. (B) SEM image of cells of *Bacillus subtilis*, readapted from [115]. (C) Example of result from my experiments of biofilm growing against a gradient of osmotic pressure. Bottom row: (D) confocal image of fungal spores of *Amanita lavendula*, (E) Spore print. (F) Some purple mushrooms (*Laccaria amethystina*, source: http://pixdaus.com).

suggest that (i) initiates biofilm tranlocation toward large osmotic pressure at early growth stages, then (ii) takes over, potentially together with (iii), and the biofilm translocates toward low osmotic pressure. These results open up further questions: (i) which genes are modulated during the experiments? (ii) how is biomass production rate affected by external conditions? (iii) how is the dynamics of the contact line affected by osmotic gradients?

In the second part, I will discuss my second project, that I conducted in collaboration with the Pringle lab at university of Wisconsin-Madison, where I spent eight months of my PhD. I investigated the spore release mechanism of a particular phylum of fungi, the basidiomycetes (see 1E). Fungi are an essential component of the Earth ecosystems, but they are usually difficult to study due to their hidden growth in tissues and soils. A common assumption among mycologists is that fungi can not control the fate of their spores, leaving it to chance and producing a large number of spores. The idea that I

have explored is whether fungi have evolved morphologies that maximize the number of produced spores investing the minimum amount of tissue for the production. For this project, I collected specimens, I elaborated a protocol to collect spores with the use of spore prints (Fig. 1E), I took confocal microscope images of spores (Fig. 1D) and I conducted data analysis. The data I collected and analyzed, as well as data taken from the literature, show consistency with the hypothesis of maximum packing. In order to achieve maximum packing, fungi must control the size of a droplet that grows extracellularly. Hence my results open up the question of how fungi regulate a process that is purely extracellular and depends on the varying external conditions.

Part I

Bacterial Biofilms

Chapter 1

A general introduction on bacterial biofilms

By IUPAC definition, a biofilm is an "aggregate of microorganisms in which cells that are frequently embedded within a self-produced matrix of extracellular polymeric substances (EPSs) adhere to each other and / or to a surface" [158]. Biofilms generally incorporate multiple species of bacteria, as well as fungi (including yeasts), algae or other microorganisms. As a group, bacterial communities appear to have several advantages over single cells: distinct cell types perform specialized functions and manage access to nutrients, and the matrix acts as defense mechanisms for desiccation and antagonists. As a result, these communities of cells live in a wide variety of habitats and they can potentially develop on every surface in a non-sterile humid environment, even at extreme conditions. They are present in all natural ecosystems except abyssal oceans and deep groundwater. In hospitals, they develop on various medical devices such as central venous catheters, mechanical heart valves, urinary catheters, and contact lenses. Biofilms are involved in the development of human hospital acquired infections such as cystic fibrosis, periodontitis and native valve endocarditis [31][49], causing additional medical costs to be more than 3 millions of euros per year in France only [24]. They are also present in industrial pipelines, causing clogging and increasing pipes corrosion rate. When they form on vessels, they favor the adhesion of other marine organisms to the metal surface. This reduces vessel speed, increases corrosion and requires additional costs for cleaning and repairing [31][13]. In food industry, they colonize both the industrial plants and the food, causing inefficiency in production and posing a health risk for the consumers [15][184]. Despite their dangerousness and harmfulness, biofilms can also be exploited for useful purposes such as waste-water treatment and ocean cleaning from petroleum oil spilling [101] [138]. They are also used to produce electricity from organic waste in microbial fuel cells [11] [181]. Historically, biofilms are observed for

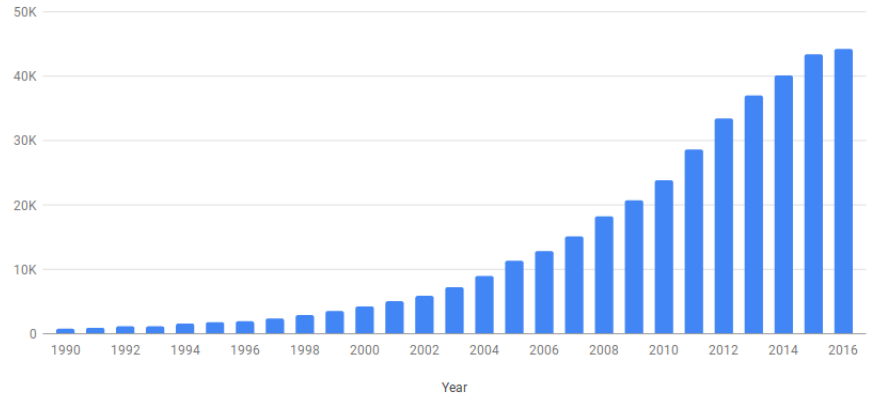

FIGURE 1.1: Google scholar results for 'biofilm' from 1990 to 2016. Data from https://csullender.com/scholar.

the first time at the end of the 17th century in the form of teeth plaque, but for most of the time bacteria have been studied in the form of single planktonic cells capable to swim in a fluid thanks to appendages called flagella. It is only after the arrival of electron microscopy that bacterial biofilms are studied in more detail and it is at the end of the 1970s that the theory of biofilm predominant growth state over free-floating planktonic form takes place [21]. The outburst in biofilm research starts at the end of the 1990's (see Fig. 1.1), when technological advances enable the use of laser scanning confocal microscopy and time-lapse video and genome sequencing platforms become more sophisticated and fast.

In this chapter I review the most important information about biofilms I have gone through during my PhD from both the biology and the physics perspective. I will conclude this chapter explaining what particular aspect of biofilm formation I investigated and the mathematical model applied. Before reviewing the biofilm mathematical model we decided to use, I will examine what are the features occurring in biofilms and which motility mechanisms they adopt, with a closer look on the most important genes expressed in *Bacillus subtilis*, the model organism I used for my experiment.

1.1 Biofilms in biology

1.1.1 Common features of biofilms

A very direct and common way to characterize bacteria is to distinguish them into two categories, depending on the Gram-stain test result they give: gram-positive and gram-negative bacteria. This classification eventually distinguishes the two categories according to the bacterial cell wall. The first are bacteria that give a positive result in the Gram-stain test and appear violet at microscope observation. This happens because the cell membrane of gram-positive bacteria includes a thick peptidoglycan layer that makes the cells able to retain the stain and appear violet after the discoloration phase of the test. Gram-positive bacteria include species such as *Streptococcus pneumoniae*, *Streptococcus mutans*, *Staphylococcus aureus*, *Streptococcus sanguinis* and *Bacillus subtilis*. The gram-negative bacteria have a much thinner cell wall and are not able to retain the violet stain after the discoloration phase, appearing red or pink when observed under a microscope. These category includes species as *Escherichia coli*, *Salmonella enterica*, *Legionella pneumophila* and *Pseudomonas aeruginosa*. All the microorganisms share the ability to form biofilm. Bacterial biofilms are communities of cells that appear to be extremely resistant to environmental stresses and antibiotic treatments, this thanks to the polymeric matrix that gives also structural integrity [89] [65] [131] [34] [80]. But molecular pathways regulating biofilm formation can differ a lot from species to species [137]. Sometimes differences can appear also in different strains of the same species. However, biofilm formation shows some general features common for all species and described here.

Metabolic pathways that activate biofilm formation are triggered by extracellular molecules. The extracellular molecules that trigger metabolic pathways activating biofilm formation are produced by cells themselves or by the external environment [72] [134]. These molecules can activate either a quorum sensing system response or genetic pathways independent from cell density [86] [160]. In biology, quorum sensing is the ability of a microorganism to coordinate gene expression and hence express specific genes as a response to cell population density. Signaling molecules that are produced in response to changes in cell-population density are called autoinducers. For *P. aeruginosa* and many other gram-negative bacteria, quorum-sensing systems respond to

a class of autoinducer termed acyl homoserine lactones (AHLs). For gram-positive organisms, autoinducers are usually peptides such as AIP or surfactin. Compounds triggering biofilm formation without involving quorum-sensing are usually secondary metabolites such as antibiotics or toxins produced by other organisms [7] [86].

Single species biofilms show cell heterogeneity. Single species biofilms are a clonal population and can start even from a single cell. However, single species biofilms show cell type differentiation. This means that the genotype (the ensemble of genes composing cells DNA) is the same for all cells, whereas the phenotype (the observable characteristics of an organism) changes from one cell to the other. These phenotypic differences arise from gradients in the extracellular conditions. These gradients can be of nutrient, available oxygen or osmotic pressure and create microenvironments stimulating different gene expressions [135] [139]. For example, in *Streptococcus aureus*, biofilms show two distinct strata: one in proximity of nutrients at the colony-agar interface, which is metabolically active, and one at the interface colony-air that shows no metabolic activity [122]. *Pseudomonas aeruginosa* biofilms have a stronger enzymatic activity for alkaline phosphatase, that has an oxygen-dependent activity, in cells closer to the oxygen-exposed areas [177]. Also *Bacillus subtilis* biofilms have subpopulation of cells expressing different functions such as sporulation, matrix production, and motility. It has been show that for this bacterium, distinct functions occur in distinct subpopulations within the biofilm [159].

Structural components of the biofilm consist in cells enveloped in a polymeric matrix secreted by cells themselves. The matrix is composed of polysaccharide biopolymers and other substances, such as proteins or DNA [171] [7] [77]. Despite the common presence of these components, the synthesis timing, the final composition and the architecture of biofilms show great variation depending on species, strain and environmental conditions. Cellulose is an important component of the extracellular matrix (ECM) of *E. coli* [183] [7]. *B. subtilis* undomesticated strain NCIB3610 secretes polysaccharide EPS [6], while the undomesticated strain RO-FF-1 produces poly-δ-glutamate (PGS)[136]. Polysaccharide intercellular adhesin (PIA) is produced by *S. aureus* [105] [90] [7] [86]. *Pseudomonas aeruginosa* biofilms synthesize polymers alginate, PEL and PSL, but their synthesis changes from one strain to the other [41] [94] [61] [7] [86]. Biofilm matrix includes also adhesive proteins, such as TasA for *B. subtilis*[6].

Straphilococcus aureus expresses multiple biofilm- associated proteins (Bap proteins) used to hold cells together. *Escherichia coli* produces Type I fimbriae, that help adherence on plastic surfaces [114] [175], and curli protein [16] [3] [86]. In *P. aeruginosa*, type IV pili or the CupA fimbriae allow adherence on surfaces [107] [155] [22] [71], while two lectin-binding proteins (LecA and LecB) help cell-matrix and cell-cell interactions [149] [27][86].

Examples of structural components of biofilm matrix

Species	Biopolymers	Proteins
B. subtilis	EPS, PGS	TasA
E. coli	cellulose	Type I fimbria
P. aeruginosa	alginate, PEL, PSL	type IV pili, CupA fimbriae, LecA, LecB
S. aureus	PIA	Bap

1.1.2 Generic biological model of biofilm growth

As biofilms of different species share common features, previous and current work is devoted to establish a developmental model of biofilm formation that could be valid across species. This model is based on changes in genetic expression and characterized by a multistage process that includes the following steps:

- initial adherence of free-floating bacteria cells to a surface or interface;
- cell-to-cell adhesion and formation of a monolayer of cells;
- formation of a multilayer colony;
- secretion of extracellular matrix;
- maturation of the biofilm 3-D structure into an architectural complex biofilm;
- detachment and dispersal of cells [82][50].

The molecular mechanisms that regulate growth vary from species to species. The initial phase of surface attachment is different between motile or non motile cells and between gram-positive and gram-negative bacteria. Motile species need to perform a switch from the expression of flagella genes to production of extracellular matrix. The presence of flagella seem to be anyway necessary for biofilm formation, as flagella-defective mutants present less structured

biofilms. Apparently this is because flagella movement overcomes repulsive forces between the bacteria and the surface [114] [165] [81] [82]. But flagella-mediate motility is not the only mechanism used. Some gram-negative bacteria such as *P. aeruginosa* use type IV-pili motility, which is absent in gram-positive bacteria like *B. subtilis*. On the other hand, non-motile cells raise adhesins expression when they encounter a surface to promote adhesion on the same surface [46] [78] [82]. An example of this is *S.aureus*, which produces Bap proteins when interacting with other cells or surfaces (Lasa and Penades 2006) [82].

1.1.3 Cooperative motility

One of the main focuses of this part of the thesis is bacterial biofilm motility. In many bacterial species, single cells are able to swim in liquid medium thanks to flagella driven by a rotational movement powered by transmembrane proton potential. Each flagellum is composed by a basal motor encased in the membrane and connected to a left-handed helical filament outside of the cell through a short curved external section, called the hook. The external filament is typically $5 - 10\mu m$ long with a diameter of 20 nm and can rotate counterclockwise or clockwise, which will cause the cell to undergo the typical run-and-tumble trajectories.

On the other hand, biofilms are communities of bacteria able to colonize surfaces and translocate collectively, using different motility mechanisms depending on the species. These communities can remain localized, or translate to colonize new surface, or produce fruiting bodies for spore release depending on the available nutrients and on the surface conditions. Mechanisms for cooperative surface motilities in biofilm formation include:

- *Swarming*. It requires presence of flagella and allows rapid movements ($2 - 10\mu m/s$) across solid or semi-solid surfaces. It can be viewed as a form of swimming on a surface. Swarmers' cells are hyperelongated, hyperflagellated and more localized at the edge of the colony. The hyperflagellation is probably because cells have to overcome higher surface friction and viscosities of the matrix than in the planktonic state. They usually move only in one direction and reverse only on impact with an obstacle on the outer edge of the colony. Cells in the inner part of the colony display less motility and switch to a vegetative state. Some of

the genera showing this kind of motility are *Bacillus*, *Escherichia*, *Pseudomonas*, *Salmonella*. In some species, swarming requires self-production of biosurfactant [52] [51].

- *Gliding/adventurous gliding*. It allows for colony extension rates of $0.025 - 10\mu m/s$ over surfaces of low aqueous films. A specific model for mechanisms involved in this type of motility was proposed and recently developed [145]. In this case, cells can move back and forward along their long axis. This kind of motility is observed in myxobacteria, cyanobacteria and the *Cytophaga-Flavobacterium* group [53].

- *Twitching/social gliding/retractile motility*. It is a jerky movement that requires presence of type IV pili that actively extend from the cell, bind to a surface and retract [95]. It allows for colony expansion rates of $0.06 - 0.3\mu m/s$ over moist surfaces both forward and backward. Pili are $4\mu m$ long with a diameter of 6 nm. In twitching, in case of nutrient depletion, cells accumulate together to form fruit bodies, while in nutrient-rich conditions it promotes outward movement of colonies. Examples of bacteria showing this kind of motility are: *Legionella*, *Pseudomonas*, *Streptococcus*. When establishing microcolonies, *P. aeruginosa* twitching cells slow down,accumulate and deposit further EPS components when they encounter high EPS deposition areas [182].

- *Sliding/spreading*. It is a form of passive translocation as it doesn't require motile organelles. It allows for expansion rates of $0.03 - 6\mu m/s$. Sliding involves production of biosurfactants as lipopeptides, lipopolysaccharides and glycolipids, that reduce surface tension. The reduction of surface tension combined with the expansion of growing biofilm mass produces sliding. It is observed in *Bacillus*, *Escherichia* and *Streptococcus*, among others [53][51].

In general, environmental conditions influencing motility are moisture, abundance of nutrients, matrix compounds, and temperature [51].

1.1.4 A case study: *Bacillus subtilis*

For our experiments, we decided to use *B. subtilis*. This is a non-pathogenic gram-positive bacterium found in soil and in the gastrointestinal tract of ruminants and humans. Its cells are rod-shaped and are about $2 - 4\mu m$ long and about $1.0\mu m$ in diameter [54] [64]. *B. Subtilis* is a model organism that has been broadly studied in the field of molecular genetics in the past decades. The

molecular pathway controlling endospore formation in single floating cells as a response to starvation and high population densities is very well known [9] [47] [133] [113] [82] and *B. Subtilis* biofilms have been recreated in the laboratory in form of pellicles and colonies [8]. *B. subtilis* strain NCIB 3610 (hereafter referred to as "wild type" (WT)) can form robust and highly structured biofilms both in liquid and on solid medium. Moreover, there is a particular solid agar recipe containing Minimal medium (MSgg)[8] that in *B. subtilis* promotes gene expression for extracellular matrix production. When placed on MSgg surface, cells develop into complex wrinkled colonies. Genomic data, ease of genetic manipulation, availability of experimental protocol and non-pathogenity make *B. subtilis* a very good candidate to study biofilm growth.

Several different cell types compose *B. subtilis* biofilm. Here I focus on three cell types: motile, matrix producers and sporulating. As I pointed out previously, single species biofilm can originate from a single mother cell, in which case they are a clonal population. However, in biofilms, the clonal population is composed by multiple subpopulations that are genetically identical (i.e. they have the same DNA) but phenotypically heterogeneous (i.e. each subpopulation expresses different genes). At first, cells express motility genes and produce flagella. Once they find a suitable host surface, they adhere to it and most cell differentiate into non-motile, matrix producing cells. At the initiation of biofilm formation, the cells that switched to matrix production form chains, grow and aggregate surrounded by the extracellular matrix. The latter is composed of EPS and proteins, protects the cells during the maturation of the biofilm and guarantees adherence to the surface. In mature biofilms, matrix producing cells eventually differentiate into sporulating cells. Eventually, biofilm disperse when nutrient resources begin to be limited and waste products accumulate (see Fig. 1.2)[160].

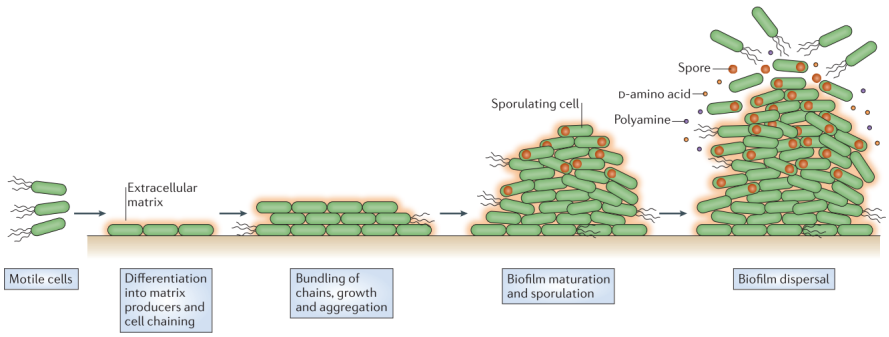

FIGURE 1.2: Life cycle of *B. subtilis* biofilm [160]

A complete survey of the genetic pathways involved in biofilm formation

by *B. subtilis* is beyond the scope of this thesis. However, I decided to summarize the most important molecular mechanisms involved for sake of completeness. In *B. subtilis* there are several regulatory pathways involved in control of biofilm formation and dispersal. The most important genes involved in motility are *hag*, *lytABC* and *lytF*, whereas for extracellular matrix production *tapA-sipW-tasA* and *eps* operons and *bslA* gene are involved. *hag* encodes flagellin. *lytABC* and *lytF* encode autolysins, needed for cell separation. *tapA-sipW-tasA* operon encodes TapA, a protein membrane needed for anchoring and assembling, the type I signal peptidase W, and TasA, a fiber component. *eps* operon encodes synthesis of EPS. *bslA* gene encodes biofilm surface layer protein, providing hydrophobicity to the biofilm (see Table 1.2)

Genes involved in ECM production in *B. subtilis* colonies		
Gene	**Role of encoded protein**	**Mutant phenotype**
eps operon	produces EPS	flat colonies
tapA	anchors TasA fibers to the cells	flat colonies
sipW	signal peptidase required for TapA and TasA production	flat colonies
tasA	major protein component of TasA fibers	flat colonies
bslA	provides surface hydrophobicity	flat colonies

TABLE 1.2: Genes involved in ECM production in *B. subtilis* colonies. Readapted from [160]

Multiple cues can lead to matrix production in *B. subtilis* biofilms. Below I describe the main pathways for this phenotypic transition, which undergoes three successive stages: (i) kinase activation, (ii) phosphorylation of Spo0A, (iii) upregulation of matrix genes (see Fig. 1.3).

Kinase activation. One of the possible ways to trigger matrix production is when a subpopulation of cells senses potassium leakage in their membranes. The leakage of potassium is induced by the lipopeptide surfactin, which is usually secreted by the biofilm cells (or by other organisms in soil) [86]. In *B. subtilis*, surfactin does not interact with all the cells at the same time. Instead, the subpopulation secreting surfactin is distinct from the subpopulation of cells that sense and respond to surfactin. Surfactin is a quorum-sensing molecule (i.e. a molecule that regulates gene expression and whose concentration is proportional to the cell population density) and is one of the primary inducers of

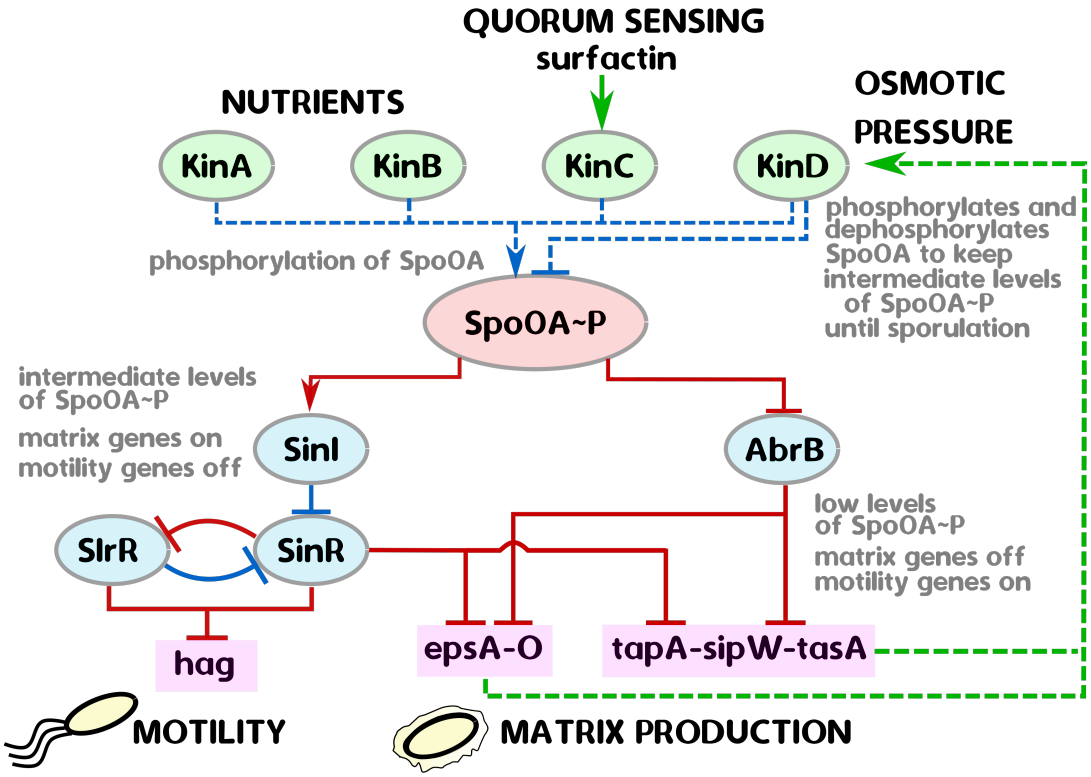

Red lines indicate transcriptional regulation; blue lines indicate protein–protein interactions; green lines indicate extracellular signals; solid and dashed lines indicate direct and indirect regulation, respectively. Pointed arrows indicate activation. Flat arrows indicate inhibition. Green circles are kinases; red and blue circles are proteins; pink rectangles are operons.

FIGURE 1.3: Simplified schematic of molecular pathways that lead to matrix expression in *B. subtilis*. Readapted from [160].

potassium leakage in cell membranes. Those cells where a membrane sensor kinase, KinC, detects potassium leakage from the membrane of the cell, activate KinC itself. Similarly, there are four other kinases (KinA, KinB, KinD and KinE) that are activated by extracellular signals, e.g. small molecules [130] and osmotic pressure [124]. These kinases also activate by phosphorylation a protein called Spo0A, see ref. [160] for a review of the molecular pathways leading to these phenotypic transitions in *B. subtilis* biofilms.

Phosphorylation of Spo0A. Spo0A is a central transcriptional regulator and controls the expression of many genes, counting those necessary in matrix development and sporulation [98]. Spo0A is activated with a phosphorelay, a multi-stage process where one of the kinases donates a phosphoryl group to an aspartate residue of Spo0A. Spo0A and its phosphorylated form Spo0A-P

are always present in the cell, but their concentrations vary and they regulate genes expression in the cell as described above. When Spo0A-P inside the cell overcomes a certain level, the gene production of matrix is activated. As biofilm maturation continues, Spa0A-P level raises further and subsequently sporulation is activated [160].

De-repression of SinR. Spo0A-P controls matrix gene expression though at least two parallel pathways involving (i) SinI/SinR complex and (ii)AbrB. In the first pathways, Spo0A activates protein SinI, that is the antirepressor (i.e. a protein that blocks or inactivates a repressor) of protein SinR. SinR is a master regulator that represses *tapA-sipW-tasA* and *eps* operons and the regulatory gene *slrR*. SinI binds to SinR and makes SinR incapable of binding to DNA, thereby de-repressing expression of *tapA-sipW-tasA* and *eps* operons.

There is a second independent pathway that leads to matrix production. In this second pathway, Spo0A represses AbrB, which is also a repressor of the two operons responsible for matrix production, *tapA-sipW-tasA* and *eps*. Additionally, AbrB also represses *slrR*, which works synergistically with SinI to represses SinR and ultimately upregulates expression of *tapA-sipW-tasA* and *eps* operons. Hence, when Spa0A-P represses AbrB, *tapA-sipW-tasA*, *eps* and *slrR* are expressed. Specifically when SlrR levels are low, SinR is active, matrix genes are off and cells are motile. When SlrR levels are high, it binds to SinR and blocks its activity, thus derepressing matrix genes.

Interestingly, the same pathways described above upregulate matrix, and at the same time repress motility and promote chaining. Indeed, the second role of the SinR-SlrR complex is to repress the motility gene *hag* and autolysins genes *lytABC* and *lytF*, thus allowing the formation of chains of cells. Hence, when SlrR levels are high, cells form chains and activate matrix production. This switch is made possible by a positive feed-back loop: Spo0A-P activates SinI, that represses SinR and allows accumulation of SlrR, that in turn reinforces inhibition of SinR.

I discussed above the transition between three different cell types: motile , matrix producers and sporulating cells. There are other phenotypes involved in *B. subtilis* biofilm formation, that I have not discussed. Here I will mention one additional cell type: the cannibal. Two operons encode secretion of toxin peptides Skf and Sdp and are upregulated at intermediate levels of Spa0A-P. The cells secreting Skf and Sdp are also resistant to the same toxins, hence Skf and Sdp kill most of the cells except their producers. Dead cells are then cannibalized by the toxin-producing cells. Interestingly, the subpopulation

of cannibals overlaps largely to the subpopulation of matrix producers [87]. Hence, only matrix producers survive to multiplicate themselves. This process is thought to be a mechanism to delay the onset of sporulation, as spore development is energy demanding [45]. Here I just resumed the main pathways that lead to biofilm initiation. For a more complete review of the other mechanisms involved, you can see [160].

1.2 Biofilms in physics

So far, I introduced a general description of what are biofilms and where we can find them. I described what general features can be found in all biofilms and what are the different stages of growth. Then I described in more detail the biological pathways involved in the model species we decided to use, *B. Subtilis*. Now I will shift the focus on what is the physics involved in biofilm development. I will briefly describe what are the artificial systems used to study biofilm growth. I will introduce how biofilms can be viewed in the context of soft matter physics, I will give some example of mathematical models that prove a direct connection between gene expression and the role of specific physics phenomena and I will conclude with the description of the model that we used for our experiments.

1.2.1 Biofilms in external environments and in the laboratory

I recalled previously how different biological pathways can regulate biofilm formation. Despite the biological differences, some general features are expressed across different species. As I have already underlined, biofilm formation as well as its final architecture depend on phenotypic differences in subpopulations of cells composing the biofilm. These phenotypic differences are triggered not only by biological signals, but also from physical constraints that depend on the physical environment, as flow rate and direction, or temperature. Biofilm 3-D structures show similarities when developing in similar physical conditions [111]. Submerged biofilms growing under the action of high-shear flows develop as filamentous streamers or in ripple structures. In the first case, microcolonies develop an upstream "head" attached to a surface and a downstream "tail" that oscillates freely in the fluid current [125] (see Fig. 1.4), whereas ripple structures show a wavy growing pattern [118] (see Fig. 1.5). Two examples in nature of these kind of biofilms are periphyton in rivers and in algal mats. On the other hand, when the biofilm grows in quiescent or

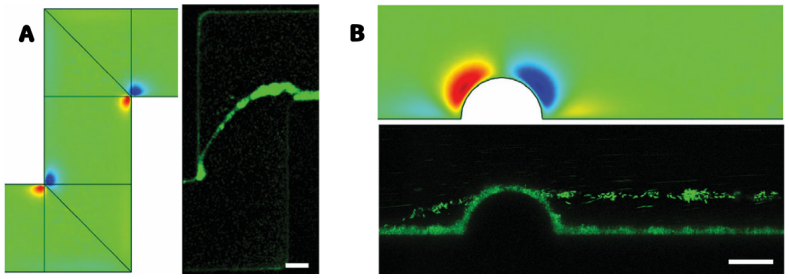

Species: *Pseudomonas aeruginosa*. (A) curved channel, scale bar 50 μ m (B) straight channel with a lateral hemi-cylindrical bump, scale bar 25 μ m. Red and blue colors indicate velocity components orthogonal to the plane of the channel, and directing, respectively, upwards (positive y) and downwards (negative y).

FIGURE 1.4: Comparisons between numerical simulations of the secondary flow and experimental observations of the streamers, from [125].

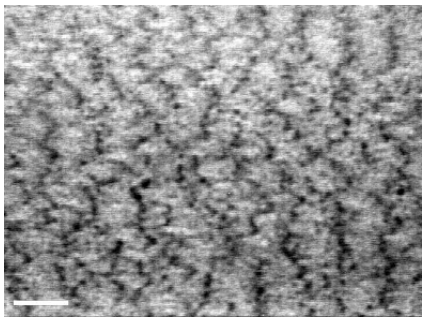

Biofilm growing in a turbulent flow cell taken at days 4. The ripples were aligned perpendicularly to the flow direction (right to left). Scale bar, 200 μm.

FIGURE 1.5: Image of *Pseudomonas aeruginosa* biofilm ripple structures. [118].

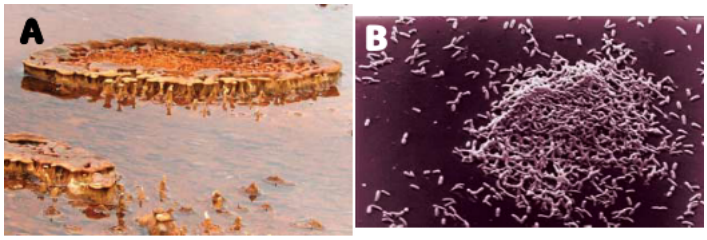

(A) Biofilms are from the Biscuit Basin thermal area, Yellowstone National Park, USA. (B)*Pseudomonas aeruginosa* biofilm grown in a flow cell with a flow of 0.03 m/s.

FIGURE 1.6: Biofilms growing in quiescent or low-shear environments. [49]

low-shear fluid, it develops a circular structure with isotropic patterns, both in the case of submerged biofilms and for biofilm growing at the interface with air [49] (see Fig. 1.6) This capability of changing their structure depending on the applied external stress condition can be reproduced also in laboratories. With time, four artificial systems have become of common use among the countless ways to generate biofilm formation in a laboratory, here described.

- **Flow cells.** They are used to study submerged biofilms. They consist of small chambers with transparent walls where the flow rate can be controlled in real time and flow is used to feed biofilms with fresh nutrients. This system can be easily adapted for real-time observation of biofilm evolution and placed on a confocal scanning laser microscope (CSLM) stage, but has the disadvantages of being a slow process to examine different mutants [17] [7] [82] and of being suitable only for the observation of the initial stages of biofilm formation.

- **Microtiter dishes.** They are also used to study submerged biofilm, but in batch culture under condition of no flow. The biofilm is visualized through microscopy and visualization is often improved by the use of a nonspecific dye. This system is easy to use and allows faster analysis for gene identification than in the case of flow cells [107] [106] [114] [165][166] [156] [82].

- **Standing cultures.** They are used to study pellicles, that is floating biofilms that develop at the air-liquid interface [8] [41] [48] [32] [82]. The combination between the absence of a solid surface and the slow-moving flow favor assembly of cells in complex structures at the interface between air and liquid. This system is easy to use and allows fast analysis for gene identification.

- **Agar-solified media.** They are used to study colonies, that is biofilms with highly structured morphologies. The level of complexity in biofilm morphology correlates with the levels of production of extracellular matrix [40] [179] [82]. Mutants defective of matrix production genes develop smooth and flat colonies. This system is highly versatile, easy to use and adaptable.

Unfortunately, no experimental approach among the four listed above enables to investigate at the same time all the processes involved in biofilm initiation and development. In the last decades, advancements in genome sequencing made it possible to broadly explore bacteria's genetic expression and

partially uncover the variety of processes involved in microbial communities. However, the physical aspects involved in gene regulation of microorganism are still inquired. At the present date though, it is still not clear which one between genetics (active response) and environment (passive response) has the major impact on the evolution of biofilm morphology. The two kinds of response seem to be somehow related and several research groups in the last two decades have tried to study them simultaneously. Despite the advancements in technology and research, no definitive answer has been given so far. [50]. Thoughtful experiments and interdisciplinary collaborations are needed to understand how the two interact and their relative importance in dictating biofilm morphology.

1.2.2 Biofilms as soft materials

Until now, I have listed the biological aspects of biofilm formation and I have given some examples about how physical environment can also shape biofilm growth. Now I will introduce tools from physics that can be applied to biofilm research to characterize and predict how a microbial community will evolve in time. Biofilm formation is a dynamic process that can be investigated from the perspective of soft matter physics. From this viewpoint, biofilms can be assimilated to hydrogels developing at the interface between a solid and a fluid and whose thickness ranges from tens of microns to few millimeters. From this colloidal gel perspective, bacteria are the microscopically dispersed insoluble particles and the extracellular matrix is a network of hydrated polymer chains held together by protein- and polysaccharide-mediated cross links. Bacterial cells can be viewed as spherical or rod shaped rigid particles that hardly deform under external stresses, but biofilms as a whole are dynamic materials that can adapt to the external environment. About the matrix, little is known about its mechanical properties, or about how the physical and chemical conditions of the external environment interact with its development, but it is suggested to be the source of bacteria cohesive strength [70][164][174] [112] and to offer protection from external agents. In this subsection, I will give an overview of biofilm mechanics and dynamics. The mechanical properties of hydrogels depend on their composition, in particular on the water content at equilibrium. Biofilms can regulate the composition of the extracellular matrix, thus regulating their water content and controlling their mechanical properties. Bacteria control also their interfacial properties, secreting surfactants to

promote cell-cell interaction within the biofilm. Local heterogeneities in polymer production, cell proliferation rate and biosurfactants secretion can determine changes in the biofilm life cycle. These changes are caused by local gradients in nutrient or oxygen concentration, or in osmotic pressure. Hence, identifying the physical cues that control bacterial gene expression is a key point in getting a better understanding of biofilm dynamics.

Viscoelasticity. It has been reported that a wide range of biofilms grown under the action of a fluid flow shows classic viscoelastic behavior [141][70] [73] [150] [49] like most soft materials. Accordingly, they present a time-dependent response to mechanical stress characterized by elastic shear modulus G, that is the relation between applied force and relative deformation, and relaxation time τ, that is the time necessary for a perturbed system to return to equilibrium. In soft matter physics, the elasticity of an hydrogel has the form of the thermal energy per unit volume of the empty space within the polymer mesh $G \simeq k_B T/\xi^3$, where k_B is Boltzmann's constant, T is the temperature and ξ is the polymer mesh size [43]. This relation arises from the contraposition between deformation of polymer chains and entropic fluctuations of the material. Biofilms can behave elastically over short time scales, absorbing rapid changes in shear stress like those expected in aquatic environments such as seas and rivers during stormy seasons. If shear stress loads the biofilm over long time scales, then viscous flow comes into play and the biofilm flows over the surface or reduces drag assuming a streamlined shape or ripple-like wave structure [118] [142] [49], with the viscous response of the biofilm depending on τ of the biofilm itself.

Importantly, viscoelastic properties of colloidal gels depend also on the fractions of liquid volume and colloidal volume in the material, which may be regulated by the biofilm. For spherical cells, like those of *S. Aureus*, when the colloidal volume fraction ϕ reaches an intermediate value ϕ^*, the surfaces of the colloidal particles begin to touch and the biofilm starts to show elastic behavior. For $\phi > \phi^*$, the elastic modulus G grows as a function of ϕ for a disordered system of repulsive spheres and the biofilm behaves like a solid paste, displaying stress relaxation on very long times. When $\phi < \phi^*$, the material is a liquid suspension. For rod-shaped cells like those in *B. Subtilis*, the same process occurs but the onset of elasticity happens at higher ϕ^*, as the rods are considered as anisotropic particles that can rotate when packed. In both cases, the elasticity at very high ϕ depends on the elasticity of the colloid. In biofilms, the bacterial volume fraction ϕ_b is considered the same as the volume fraction

ϕ of colloids. Indeed, although 80% of bacteria cells volume is made of water, that water is not freely available in the extracellular space. For pellicles, ϕ_b is usually less than 0.2 and the elastic properties of the biofilm depend mainly on the extracellular matrix [174]. For biofilms grown on agar gel, ϕ_b is high and the material complexity limits a well defined characterization. This complexity is reflected also on available data: for biofilms grown in vitro, G is $(10^{-1} - 10^{3})$ Pa and viscosity η is $(10^{5} - 10^{8})$Pa $\cdot$ s; for biofilms from natural hot springs, $10^{3} < G < 10^{5}$ and $10^{7} < \eta < 10^{8}$Pa $\cdot$ s [143] [56][49]. Also for studies involving single species biofilm as the one in [70] on *P. aeruginosa*, G can show complex behavior, such as hysteresis in stress-strain curves between loading and unloading sections. When subject to large deformations, some biofilms show an increase in G (strain-stiffening behavior) [55] [141], which is common in structural biopolymer network such as fibrin gels in blood coagulation [144],[62]. However, the physics behind this strain-stiffening behavior remains unclear.

Osmotic pressure. When put in contact with a liquid, a polymer chain in a good solvent spontaneously swells and eventually gets dispersed in the liquid to maximize entropy. If the polymer solution is separated from the solvent by a semipermeable membrane, i.e. a membrane that allows only the solvent to flow through it by diffusion, then the polymer inside the membrane exerts osmotic pressure on the membrane. If the polymer is entangled, water flows through the membrane from the outside to the inside, the polymer swells and chain cross-links get stretched until the osmotic pressure π and the elastic modulus G balance and the system reaches equilibrium. In this perspective, having $\pi \simeq G$ at equilibrium means that the water content of the polymer and its resistance to elastic deformation are directly interconnected and this can be applied also to biofilms. For pellicles and submerged biofilms, that have a much smaller volume than the water source they are in contact with, the limit on the uptake of water they can absorb is imposed by the number of cross-links. This limitation prevents complete dissolution into water [174].

Material heterogeneity. The material properties of a biofilm are heterogeneous in space and time. Indeed, extracellular polymers exert osmotic pressure on the medium where they grow in or onto. If the concentration of polymers within the biofilm is heterogeneous, gradients in osmotic pressure (and consequently in mechanical elasticity) arise and fluid flow through the matrix is inhomogeneous, creating local compression or expansion in the biofilm. Even

if the environment is initially perfectly homogeneous, like in a Petri dish or in a standing liquid culture, heterogeneity in the biofilm material arise due to gradients in nutrient depletion. When nutrients and oxygen diffuse though the matrix surface, the cells closer to the surface consume them at the expense of inner cells, posing a limitation on the transport of molecules across the matrix. As a consequence, a spatial concentration gradient of nutrient, gases and metabolites occurs, posing a limit on growth size and affecting the physiology of the whole biofilm [25] [139] [174]. The effects of these gradients are not clear, but a few examples can be cited. Stratified patterns of DNA Replication, protein synthesis, and oxygen concentration within bacterial biofilms reveal heterogeneity in their physiological states in *S. epidermidis*, *S. aureus*, *P. aeruginosa* and *B. subtilis* [163] [121] [159]. These heterogeneities in cellular composition and metabolic activities depend on the concentration of available nutrient, which depends on the penetration depth of the nutrient within the colony. The percentage of each cell type in the global population and their localization are dynamic.

Surface heterogeneity I have introduced in subsection 1.1.3 the different types of collective surface motility. Swarming and twitching depend on motor-driven cellular appendages as flagella or type IV pili. Whereas gliding and sliding are motor-independent and involve extracellular production of amphiphilic molecules such as fatty acids, proteins, biosurfactants, lipids etc.. In the view of complex fluids, the properties of these molecules give insights also on cooperative surface motility. Spreading forces can be generated from heterogeneities in concentration of surfactant at the surface. Gradients of surfactant concentration create gradients in surface tension. These gradients are the driving force of the Marangoni effect at the interface between fluids, that generates spreading forces [128] [1] [174]. It is recognized that biosurfactants influence surface tension gradients in biofilm, lubricating surfaces and helping colonies spreading [67] [68] [4] [153]. How the material properties of a biofilm depend on the presence of environmental gradients, rather than consumption driven gradients, has not been understood. In my thesis I will consider the effect of a different environmental gradient: a gradient in osmotic pressure.

1.2.3 Coupling Fluid Dynamics with Biofilm Structure

Biofilm development is a complex dynamical process influenced by physical and chemical principles and affected by biological variability. The role of mathematical models for biofilm formation has become essential to obtain a broader

understanding of biofilm development. Mathematical models can be used to test understanding of the mechanisms underneath biofilm formation, link phenomena occurring at different time and length scales, make quantitative predictions on the experimental results, create new experimental design and optimize operating strategies. The range of available models and their complexity have increased considerably in the last 30 years, becoming a multidisciplinary effort that usually combines microbiology, biochemistry, and fluid and solid mechanics. The level of model complexity depends on the chosen biofilm system and on the questions posed. In general, models can be classified as continuum models, diffusion-limited aggregate models, continuum-discrete diffusion model and biofilm-fluid coupled models. In this study, the used approach is the one coupling fluid dynamics with the biofilm structure. The main difficulty when using this kind of models is that they usually require material parameters such as elastic modulus, adhesive or tensile strength. These material parameters can vary enormously from species to species and are complicated to measure, requiring the use of nontraditional techniques such as microrheology [92] [123], atomic force microscopy [79], or microfluidics [55]. Recently, theoretical approaches have focused on modeling specific physical aspects, such as the wetting properties of the biofilm on the agar [152] [153], or surface tension driven flow [33]. In our case, we focus on the osmotic pressure in the extracellular matrix [174] [129].

1.2.4 A mathematical model to investigate the role of osmotic pressure

I have previously introduced the main characteristics of bacterial biofilms, their growth model and the mechanisms bacteria use to translocate as a community. I continued reviewing the main regulatory pathways that govern the transition from motility to matrix production and to sporulation in *B. subtilis*. I listed the main configurations used to study biofilms in a laboratory and introduced the idea that soft matter and fluid dynamics can be used to create a model for biofilm expansion. Given this global picture, I will now proceed to introduce the hypothesis at the base of this thesis.

Bacillus Subtilis is a gram-positive soil bacterium and it is a well known biological model. When it adheres to a moist surface, it starts downregulating flagella *hag* gene expression and initiates production of extracellular polymeric matrix through the *eps* operon. At first, the biofilm grows vertically until it

reaches a critical height, above which it starts expanding radially and eventually develops wrinkles [129], whether the biofilm is grown on agar surface [174] [2] or in floating pellicles [151]. During the first 24h, expansion happens by spreading motility and is driven by the difference in osmotic pressure exerted by the matrix and the agar media. To confirm this, experiments were conducted using three different strains: *B. subtilis* WT, flagellar mutant *hag* and *eps* mutant [129]. The WT strain and the *hag* mutant show no difference in colony behavior, whereas the *eps* mutant, the one unable to produce matrix, displayed a dramatically slow expansion. These experiments demonstrated that there is a relation between the presence of the matrix and the expansion. To confirm that osmotic pressure is the physical mechanism driving expansion, as the biofilm absorbs water from the agar and swells, the authors developed a mathematical model that predicts the evolution of the cross-section profile of the biofilm in response to osmotic pressure gradients raising up by secretion of EPS.

In this model, which is inspired by similar models in [19] [147] [148] for a polymer in contact with a solvent, the colony is considered as a two phase mixture of biomass and extracellular water that behaves like a gel. At equilibrium, the biomass volume fraction is constant $\phi = \phi_\infty$ and the osmotic pressure is the same in biofilm and in agar. As cells deplete nutrient and water to produce biomass, ϕ varies and the osmotic pressure in the biofilm changes accordingly. An increase in osmotic pressure causes intake of water from the substrate to reestablish osmotic equilibrium. Throughout this process, the mass of water and biomass are conserved. At quasi-static conditions, minimizing the sum of free energy change and dissipation gives two equations of motion for the relative motion of water and biomass. Because the biofilm is much larger than it is thick, equations of motion yield a single partial differential equation for biofilm shape, i.e. for the height of the biofilm as a function of the distance from the center and time.

$$\partial_t h - K\frac{R}{r}\left[rh^3(gh)_r\right]_r = g(r)h \tag{1.1}$$

where $h(r,t)$ is the height of the biofilm at distance r from the center and time t; $g(r,t)$ is biomass production rate; R is biofilm radius and K is the sole non-dimensional parameter of the theory and depends on the equilibrium with the external environment. This equation demonstrated that a biofilm in contact with agar will first swell vertically, and eventually start to expand horizontally.

The predicted transition is observed at the early stages of *B. subtilis* development, and is reproduced quantitatively by this simple model, using a single non-dimensional parameter:

$$K = \frac{1}{3(1-\phi_\infty)^2}\frac{\mu_w}{\mu_b}\frac{h_0^3}{\xi_\infty^2 R_0} \tag{1.2}$$

Here ϕ_∞ and ξ_∞ are the biomass volume fraction and mesh size in the biofilm when this is in equilibrium with the agar, hence these quantities depend on the environmental conditions; μ_b and μ_w are the dynamic viscosities of biomass and water respectively; h_0 and R_0 are the initial height and radius of the biofilm. At long times, biofilm expansion appears to be driven by the contact line, rather than the bulk. The behavior of biofilm's advancing front was recently modeled in [153], where the surface tension was introduced to explain why surfactin mutants expand slower than the wild type.

The osmotic spreading mechanism proposed in [129] was then found to drive expansion in other species: for example, *Sinorhizobium meliloti* spreads under osmotically driven mechanisms [28]. Osmotic swelling drives expansion in colony-biofilms of *Vibrio cholerae* as well [178]. In [178], osmotic expansion was quantified directly, by allowing biofilms grown on agar to sit overnight on standing medium at 4 °C where no cell growth was measurable. The radius grew of 16%, compared to 38% when growth was resumed, demonstrating that biofilm expansion does not need growth. Osmotic forces are potentially relevant for expansion in other species: Cyanobacteria have been observed to spread preferentially where extracellular matrix is excreted, although the physical mechanism is not understood [154]. Enterobacter species and Stenotrophomonas species isolated from plant roots showed a dependence on external osmotic pressure as well [66]. The aim of my thesis was to investigate the following questions: if *B. Subtilis* biofilm is able to spread thanks to the difference of osmotic pressure between the agar media and the matrix, what happens when it grows in contact with a gradient of osmotic pressure?

Chapter 2

Methods

In this chapter I will explain the methods I used to realize my experiments before I expose my results. Most of my PhD consisted in developing an experimental setup that enabled to test the hypothesis that osmotic spreading can cause net translocation when the biofilm grows in contact with external gradients. The development of the experimental setup required almost two years of work before I could run production experiments. Methods that I developed but discarded for technical reasons are described in annex A.

2.1 Properties of agar gel

I have pointed out already that the physical environment where biofilms develop seems to be connected to biofilm growth. In my experiments I used solidified-agar gel, and here I spend a few words about properties of agar gels, which are essential to understand how environmental gradients affect osmotic expansion. One of the most common protocols for studying microbial colonies consists in plating a drop of bacteria on a Petri dish $9cm$ in diameter containing a growth medium solidified with agar. Popularity of this tool stems from its adaptability, which makes it possible to easily add selected compounds to the growth medium, and monitor how they affect growth. Petri dishes are easy to prepare and can be stored wrapped in parafilm at $4°C$ for a long time, even months, before use. Petri dishes are shallow cylindrical glass or plastic lidded dishes commercially available in multiple dimensions. Agar is a thermosetting polysaccharide extracted from red seaweed that gelifies when is put in solution, boiled and cooled below ~$40°C$, via formation of hydrogen bonds [10] [146]. Once gelified, agar gel is thermoreversible and can melt again above $80°C$ temperature [102]. Agar gels show a porous microstructure filled with water, with pores distribution ranging from 50 up to hundreds of nanometers depending on the agar concentration [12] [18] [110] [119] [176] with clusters of non- covalently crosslinked polysaccharides of about 1 nm diameter [173].

They behave as viscoelastic soft solids whose mechanical properties such as elastic modulus mainly depend on the amount of agar dispersed in the gel [104] [120]. The capacity to hold water in the gel depends on the internal chemical structure [93], and loss of water content due to evaporation over long times shrinks the gel and eventually detaches it from the walls of its container [29]. Agar shows a toughness increasing linearly with agar concentration for concentrations up to 5% and brittle failure behavior [108]. In particular, the value of the critical yield strain depends on the molecular weight of the polymer [104] [91]. When multiple colonies are present in a Petri dish, the distribution of the diameters of the colonies is similar to a Gaussian distribution and changes with the conditions of the plate. The average diameter decreases as the number of colonies in the plate increases, suggesting that the factor for limiting growth is the depletion of a component in the plate. In particular, final rate of growth is limited mainly by diffusion of nutrients, and the finals size depends on the number of colonies in the plate [20]. For my experiments, I chose to solidify the agar medium with a 1.5% w/v concentration of agar and to maintain this concentration constant with time. From my experiments and trials, I could observe that adding to the medium a final concentration of PEG higher than 5% made it impossible for the agar to polymerize, independently from the molecular weight of the PEG. I got inspired by [126] and [57] to try to create a linear osmolarity gradient directly in a Petri dish, that I describe a little bit more in detail in annex A. From my observation, this technique is very useful to get preliminary results, as it is very easy to realize, but the surface of the Petri dishes gets often irregular during the preparation and it doesn't offer much choice over the desired shape of the gradient, as it is limited only to the linear shape. Moreover, the agar limits the final concentration of PEG in the medium, making the gradient not very steep. That is why in the end we decided to do my experiments with a more developed setup that offers a better control over the shape of the gradient and the surface of agar.

2.2 Properties of Poly(ethylene glycol)

Poly(ethylene glycol) (PEG) is a flexible polymer soluble in aqueous solutions and in organic solvents. It is relatively cheap, commercially available with different molecular weights and biocompatible. We decided to use PEG to generate osmotic pressure gradients for these reasons, and also to have a reference with a previous study [124] that analyses the influence of osmotic pressure on *B. subtilis* growth using PEG of different molecular weights. A particular

property of PEG is that it does not show a linear relationship between concentration and osmotic pressure like the one usually depicted by van't Hoff equation $\pi = iCRT$, where π is the osmotic pressure, i is the van't Hoff factor, C is the molar concentration of the solute in mol/L, $R = 8.314\ \mathrm{J/(K \cdot mol)}$ is the universal gas constant and T is temperature in K, as it can be seen in Fig. 2.1. That is because for polymers, van't Hoff equation is valid only at low con-

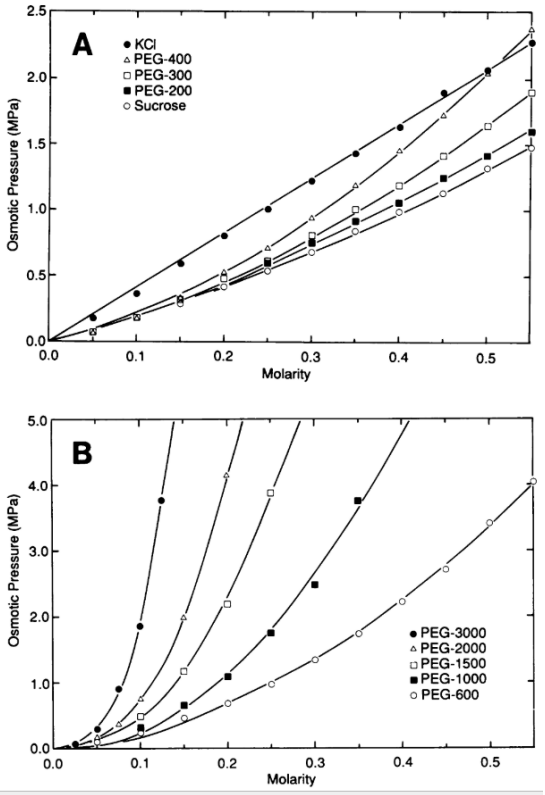

(A) Osmotic pressure vs concentration (mol L) for PEG-200 through 10k, sucrose and KCl

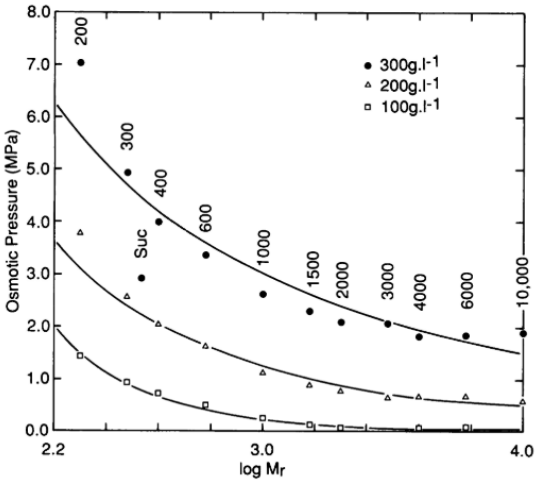

(B) Osmotic pressure vs average molecular weight for three different concentration of polymer. Sucrose shown for reference.

FIGURE 2.1: Osmotic pressure reference data of aqueous solutions of PEG measured using vapor pressure osmometry. The same concentration of different polymers in solution does not generate the same osmotic pressure. Data from [100].

centrations, whereas at high concentrations osmotic pressure depends not only on the concentration, but also on the polymer molecular weight and on the solvent used. One way to model this is by the Flory-Huggins mean field theory, where the polymer solutions are characterized as a periodic lattice where each site is occupied either by one chain monomer or by a solvent molecule. In this model, the free energy $F = U - TS$ of the system depends (i) on the interaction energy between adjacent molecules and (ii) on the entropy related to the number of possible chains configurations for a given polymer volume fraction,

$\Phi = ca^3$, where c is the concentration (number of monomers per cm^3) and a^3 is the volume of the unit cell in the cubic lattice. For the energy, the Flory interaction parameter χ describes how good the solvent is and depends on van der Waals attractions between molecules, temperature and pressure. However, Flory-Huggins theory is valid only in the limit of ideal chains, i.e. chains where monomers do not interact with each other and steric effect are not taken into account. Scaling laws are much more suited to describe real polymers, but they use similar notation to the Flory-Huggins theory. If χ is close to 0, the solvent is very similar to the monomer, hence it is good solvent and temperature has no effect on the solution structure, so that the solvent is "athermal". For real chains in good (athermal) solvents, $\chi \ll 1/2$. In this limit, there are two regimes: diluted solutions and semi-diluted solutions, where the limit between the two is set by a threshold concentration $c^* = 1/(a^3 N^{4/5}) = \Phi^*/a^3$, where N is the number of monomers per chain. When $c < c^*$, the solution is diluted and can be considered as a perfect gas, and

$$\pi = \frac{c}{N}T \quad for \quad c \longrightarrow 0$$

or, if the interaction between coils is considered:

$$\pi = \frac{c}{N}T + \frac{c^2}{N^{1/5}}T$$

For $c > c^*$ and $\Phi^* \ll \Phi \ll 1$, the solution is semi-diluted and the monomers overlap even though the volume fraction of polymers is low. In this case:

$$\pi = \frac{k\Phi^{9/4}}{a^3}T$$

or, if we look at the solution as a network with average mesh size $\xi(\Phi) \simeq \frac{a}{\Phi^{3/4}}$

$$\pi \simeq \frac{T}{\xi^3}$$

When $T = \theta$,the van der Waals attraction and the steric repulsion balance each other and dilute chains are nearly ideal, then $\chi(T = \theta) = 1/2$. When $\chi > 1/2$ the solvent is a poor solvent and a two phase region appears, as polymers tend to segregate in the solution. For semi-dilute solutions in poor solvent close to $T = \theta$, the osmotic pressure becomes:

$$\pi \simeq \frac{\Phi^3}{3a^3}T$$

which can be written again as $\pi \simeq T/\xi^3$, but in this case ξ is the correlation length and is given by $\xi \simeq \frac{a}{\Phi}$. In our case, we are in the good solvent regime, or in the limit of bad solvent regime at $T \simeq \theta$ [43].

This premise is to explain why we decided to use PEG 200 Da for my experiments. Previous works use PEG 20 kDa solutions at 15% m/v to demonstrate that *B. subtilis* pellicles respond to the external osmotic pressure. The scaling arguments summarized above imply that the osmotic pressure exerted by 5% m/v of PEG 200 Da is similar to the one exerted by a solution with 15% m/v PEG 20 kDa solution, with the advantage that PEG 200 Da is liquid, whereas PEG 20 kDa is solid, so the chance to make mistakes due to serial dilution is lower. Moreover, PEG 200 Da has a much lower viscosity than a solution with 15% m/v. In fact we measured viscosity of a range of PEG solutions, and we determined that a 5% v/v PEG solution has viscosity identical to that of water(data not shown).

2.3 A robust method to develop centimeter scale gradients in agar gels

While multiple setups have been proposed to create microscopic gradients, in my thesis I developed a setup to create stable gradients of various shapes over several cm, and for several days. The possibility to create a defined surface or solution gradient for biological and chemical applications has been an interesting experimental challenge. The experimental set-up and protocol I describe here is the last of a long list of trials I made during my thesis. For details about the trials not listed here, you can see Appendix A.

2.3.1 Microfluidic setups

Microfluidic setups have long been proposed to generate controlled gradients at small scales. To realize that, these systems employ a network of microchannels where two different concentrations of a given chemical are imposed at either side of a microfluidic setup. The two solutions of different composition flow laminarly side by side and get mixed thanks to lateral diffusion. Hence, by diffusion, the chemicals create a gradient interpolating between the two conditions [60]. With the same principle based on lateral diffusion, more complex gradients have been created by using micromixers that take three solutions as input and through a series of serpentines interpolate, either linearly or non-linearly, the inputs to create the desired gradient [63] [26] (see Fig. 2.2).

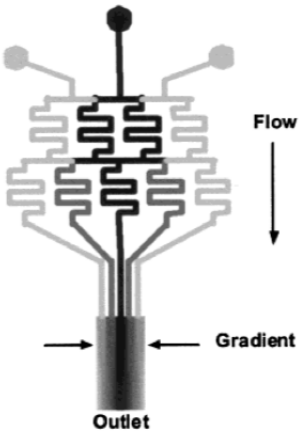

FIGURE 2.2: Schematic design of a representative gradient-generating microfluidic network [63].

Also in this case, the different solutions flow side by side in a chip, and lateral diffusion smooths out the desired gradient. As these approaches are based on diffusion, the characteristic timescale to create the steady gradient is equal to $\tau = L^2/D$, where L is the lengthscale over which the desired gradient is needed and D is the diffusion coefficient. For small molecules, $D \simeq 10^{-9}\ m^2/s$, hence diffusion will create a gradient across 4 cm in about 18.5 days. As this experiment timescale is rather impractical, we changed perspective to shorten it: instead of relying on lateral diffusion we will impose the desired gradient at the bottom of the agar gel and we will let diffusion transmit the imposed gradient *vertically* and smooth it out horizontally. In this configuration, as the agar layer is only 5 mm thick and the diffusion time scales as L^2, the diffusion timescale is reduced of a factor ~64 from 18 days to about 7 hours.

2.3.2 Numerical simulations

The goal of this project is to observe biofilm growth on osmotic gradients. In the next few paragraphs I describe an experimental setup using millifluidics to impose a gradient of PEG at the bottom of a custom made Plexiglas dish. To design the geometry of the setup, so that the gradient of PEG imposed at the bottom of the agar will diffuse to the upper surface of the agar without being deformed too much, I ran numerical simulations to predict the concentration of PEG diffusing through agar. The simulation solves a 2-D Laplace equation by the Finite Difference Method. The numerical scheme used is a second order

central difference in space (5-point difference). The equation solved is

$$\nabla^2 c = 0$$

where c is the PEG concentration in adimensional units and I imposed no flux boundary condition on the sides and top of agar, and a given concentration, following the desired horizontal gradient at the bottom.

$$\frac{\partial c(z, x = -L/2)}{\partial x} = 0 \qquad \frac{\partial c(z, x = L/2)}{\partial x} = 0$$

$$c(z = 0, x) = -\alpha x + \frac{\alpha}{2} \qquad \frac{\partial c(z = H, x)}{\partial z} = 0$$

The equation is solved in two dimensions $x \in [-L/2, L/2]$ and $z \in [0, H = \epsilon L]$, where L represents the width, H is the thickness of the gel, α is the rate of change of the concentration along the width of the agar and ϵ is the aspect

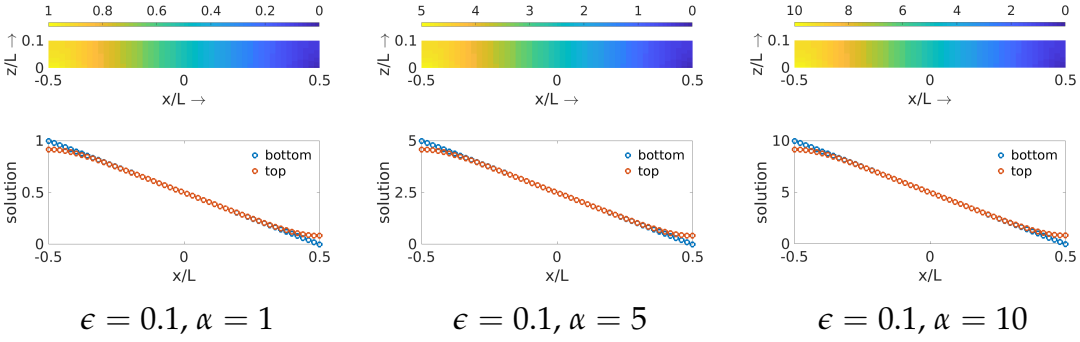

$\epsilon = 0.1, \alpha = 1$ $\epsilon = 0.1, \alpha = 5$ $\epsilon = 0.1, \alpha = 10$

(A) Results of numerical simulations of diffusion in agar with aspect ratio $\epsilon = 1/10$ and for different slopes α of the gradient. Top row: color plot of concentration for aspect ratio 0.1 and slope of the gradient imposed at $z = 0$, $\alpha = 1$ (left), $\alpha = 5$ (center), $\alpha = 10$ (right). Bottom row: concentration at the bottom (blue) and a the top (red).

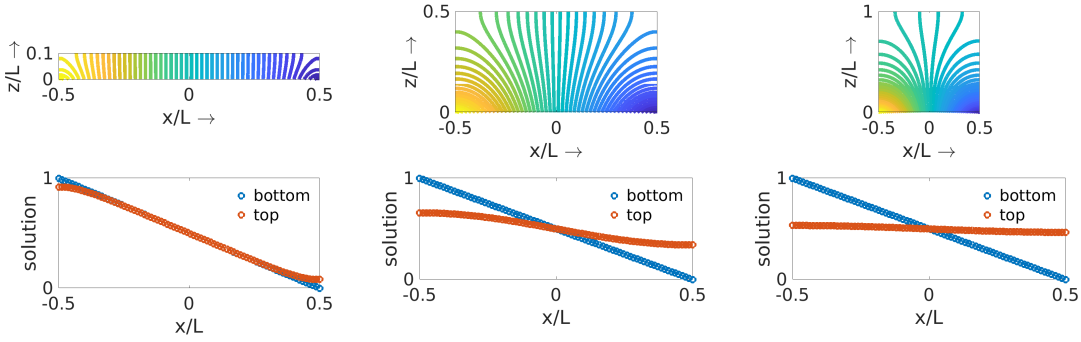

$\epsilon = 0.1, \alpha = 1$ $\epsilon = 0.5, \alpha = 1$ $\epsilon = 1, \alpha = 1$

(B) Results of numerical simulations of diffusion in agar as in panel (A), at different aspect ratios from 0.1 (left), 0.5 (center), 1 (right) and constant slope of the gradient at $z = 0$.

FIGURE 2.3: Simulations of $\nabla^2 c = 0$ imposing a linear gradient at the bottom of the cross section

ratio of the agar gel. Simulations are run in adimensional units where the coordinate x and z normalized with respect to the width L of the agar gel. Fig. 2.3 represents the results of the simulation. In every subfigure, the top row represents the concentration of polymers throughout the cross section of the agar gel color coded from 0 (blue) to $-\alpha L$ (yellow). The bottom row represents polymer concentration at the bottom $z = 0$ (blue) and at the top $z = H$ (red). The simulations show that at small aspect ratio (here $\epsilon = 0.1$) the concentration of polymers imposed at the bottom diffuses to the top without much change (Fig. 2.3a) independently on the slope of the concentration imposed at the bottom. If the aspect ratio changes, it severely affects the slope of the solution at the top of the cross section (Fig. 2.3b).

2.3.3 Final setup

To observe bacteria growth in presence of a gradient, I developed an experimental setup where I impose an external gradient of PEG, causing a corresponding osmotic pressure gradient of a desired shape in the agar substrate where biofilms grow. We designed Plexiglas rectangular dishes of internal dimensions $(7 \pm 0.2)cm \times (10 \pm 0.2)cm$ and fabricate them at InPhyNi together with their cover with drilling techniques (see Fig. 2.4). Eight equidistant holes for each short side were drilled, to connect a dispensing needle of 17 GA 1/2" diameter which was sealed to the Plexiglas using epoxy glue. Eight parallel channels were cast directly in agar, going from one short side to the other. To create the channels, eight metal sticks of $1mm$ diameter and length $(13 \pm 1)cm$ were inserted in the eight dispensing needles encased in each of the short sides, and connected the eight inlets and the eight outlets. I then tested the presence and stability of these channels by placing the sticks prior to pouring the agar, and then pouring 1.5% agar dissolved in distilled water. The agar was then left to dry at room temperature for 24h. Metal sticks were removed after 24h once the medium was dried. The removal of the sticks resulted in channels carved directly into agar. I verified that it was possible to flow water from the inlet to the outlet through the channels without breaking them apart. For the biofilm experiments, the setup and the metal sticks were sterilized with EtOH and exposed under UV light for 30 minutes before pouring MSgg medium with 1.5% agar [8]. For each test, one setup was used; for each experiment with bacteria, two setups connected in series to accumulate more statistics. To create the gradient inside the growth medium during the trial test, different solutions of distilled water and PEG 200 Da, each one with different concentrations of PEG 200 Da going from 0% to 5%v/v, were injected inside the channels going through

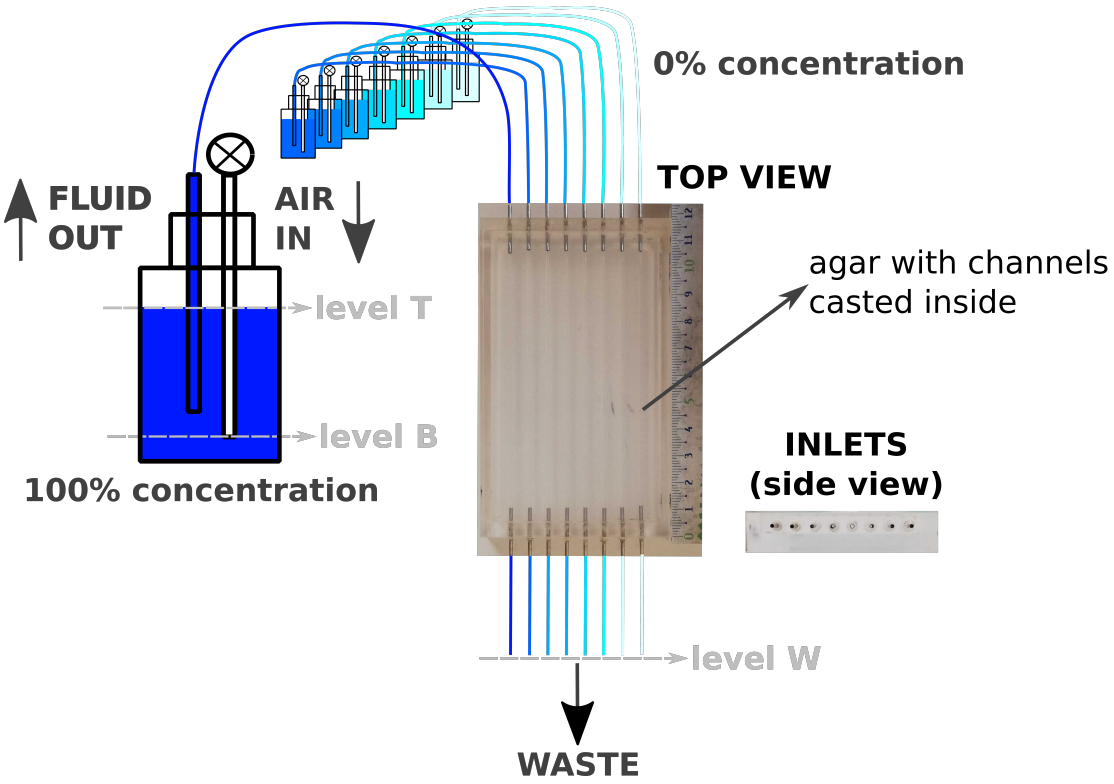

FIGURE 2.4: Sketch of the experimental setup with picture of a top view and side view of the setup dish. Solutions go from 0% concentration (light blue) to 100% concentration (dark blue)

the growth medium gel. For the biofilms experiments, the same procedure was followed flowing MSgg solutions with PEG 200 Da in the channels. In the channels, PEG 200 concentration ranged from 0% to 5% v/v. Clearly, to avoid diluting the growth medium, when PEG was mixed with liquid MSgg, the corresponding volume of water was removed from the original recipe. During the tests and the experiments, the dishes were kept inside a Plexiglas chamber where temperature was controlled and maintained at 30°C. To maintain and control the flow rate inside channels for at least 36h hours, I used a system of eight Mariotte's bottles (the principle behind Mariotte's bottles is explained in the following subsection). Each bottle was connected to a different channel. The difference in height between the entrance of the siphon and the outlet point of the fluidic circuit was kept at $(30 \pm 5)cm$. The eight Mariotte's bottles filled with MSgg medium with no agar and different PEG concentration were then connected to the eight inlet dispensing needles (see fig. 2.4) of the first dish through $(60 \pm 0.5)cm$ long flexible tubes of inner diameter $0.5mm$. The two dishes were connected in series with each other with $(10 \pm 0.5)cm$ long flexible tubes of inner diameter $0.5mm$. The outlet dispensing needles of the

second dish were then connected to a waste reservoir through $(55 \pm 0.5)cm$ long flexible tubes (fig. 2.4 shows only one dish for simplicity).

Concentration of PEG 200 Da used during experiments								
Linear gradient			**Step gradient**			**Spiked gradient**		
# Chan	**% v/v**	**% w/v**	**# Chan**	**% v/v**	**% w/v**	**# Chan**	**% v/v**	**% w/v**
1	0	0	**1**	0	0	**1**	0	0
2	0.625	0.7025	**2**	0	0	**2**	0	0
3	1.25	1.405	**3**	0	0	**3**	5	5.62
4	1.875	2.1075	**4**	0	0	**4**	0	0
5	2.5	2.81	**5**	5	5.62	**5**	0	0
6	3.75	4.125	**6**	5	5.62	**6**	5	5.62
7	4.375	4.9175	**7**	5	5.62	**7**	0	0
8	5	5.62	**8**	5	5.62	**8**	0	0

TABLE 2.1: Concentrations of PEG used in tests and experiments with bacteria.

Mariotte's bottles. The Mariotte bottle is a tool that supplies a liquid with constant flow rate [162] [96]. In a normal bottle with a hole at the base, as a liquid flows out, the change of liquid free surface height changes the hydrostatic pressure at the bottom of the bottle. Consequently, in this configuration, the flow rate decreases with time. On the contrary, this is not the case for a Mariotte's bottle. This device provides a constant pressure and consequently a constant rate of flow. It consists of an airtight bottle where two vertical tubes cross the stopper. The lower end of the tubes reaches the bottom of the bottle. One tube lets air into the bottle through an air filter, the other one lets the solution in the bottle flow outward into an external channel that goes into the millifluidic circuit. The flow rate does not depend upon the height of liquid column within the bottle, but rather on the difference in height between the bottom of the vertical tube connected to the air and the lower point of the millifluidic circuit, corresponding to the lower points of the tubing through which solutions flow to waste.

The principle governing the Mariotte bottle is the Bernoulli's equation. Initially, the air tubing is filled with solution at the same level as the rest of the bottle (Fig. 2.5A). At this time, at the bottom of the air tubing the pressure is $p_B = p_T + \rho g h$, where p_B and p_T are the pressures at the bottom and top of the bottle (levels B and T in Fig. 2.4), ρ is liquid density, g is gravity and h is

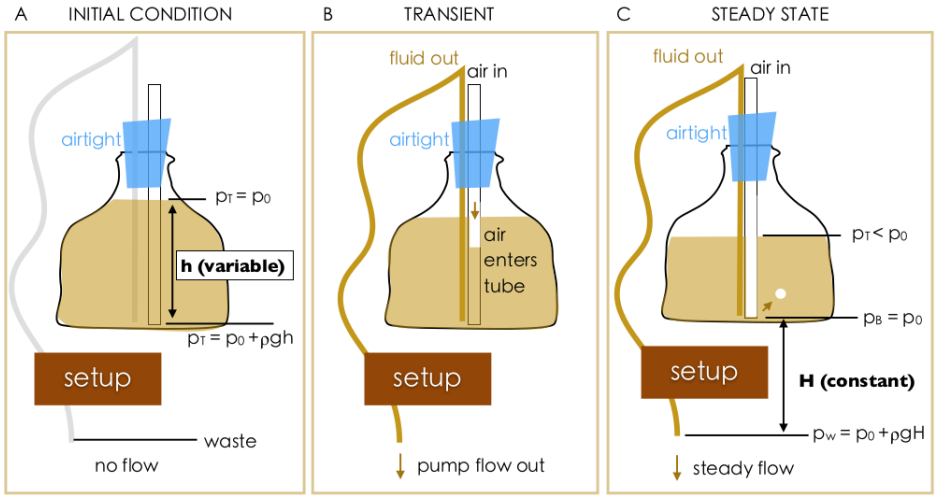

(A) Initially, the air tubing is filled with solution at the same level as the rest of the bottle. (B) Bottle is sealed and solution is forced to flow out, the level of solution within the air tube lowers and air fills the tube little by little. (C) Air tube is entirely filled with air. Flow rate does not change and depends on the vertical distance H. As p_T goes down an air bubble enters from the tube at the bottom of the bottle and travels upward.

FIGURE 2.5: Sketch of Mariotte's bottle functioning.

the height of the liquid column within the bottle (difference between height at level T and height at level B). At the same time, pressure at the top of the bottle p_T is equal to the atmospheric pressure p_0. Upon sealing the bottle and forcing solution to flow out, the level of solution within the air tube lowers and air fills the tube little by little (Fig. 2.5B). In this process, as the bottle is airtight and solution is flowing out, pressure in the air at the top of the bottle decreases below the ambient pressure, so $p_T < p_0$. Once the air tube is entirely filled with air, $p_B = p_0$ and $p_T = p_0 - \rho g h$ (Fig. 2.5C). As the solution flows out of the bottle, h changes with time. However, the flow rate will not change, because as p_T goes down an air bubble will enter from the tube at the bottom of the bottle and travel upward (Fig. 2.5C) to maintain $p_B \simeq p_0$. At this point, the bottle has reached an equilibrium: pressure at the base of the bottle equals the ambient pressure at all times since air must be in equilibrium with the external atmosphere. Hence pressure at the bottom of the bottle does not depend on the level of the solution within the bottle [69].

In conclusion, the speed at the end of the millifluidic circuit will depend on the vertical distance H between the end of the millifluidic circuit (level W in 2.4) and the bottom of the bottle (level B in 2.4, see also fig. 2.5), or more precisely the height of the lower end of the tube flowing air into the bottle.

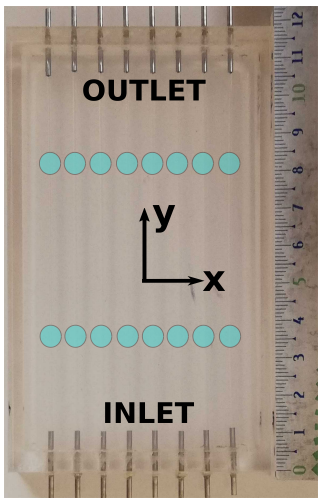

FIGURE 2.6: Image of the setup with the used x-y convention and positions of where osmotic pressure was measured.

2.3.4 Measure of polymer concentration in agar

I measured osmolality on the surface of the growth media with a Wescor 5500 Vapor pressure osmometer. I frequently recalibrated the osmometer using standard solutions.

The osmometer is not designed for gels, but rather for solutions. In the standard protocol, 10 μL of solution are aspirated with a micro-pipette tip and deposited onto a filter paper disk that is positioned in the sample holder. Once the sample holder is inserted in the sample chamber, the osmometer measures total solution concentration, or osmolality (in $mmol/kg$). The sensing element consists in a single wire thermocouple hygrometer suspended in a metallic frame that forms the sample chamber when joined with the sample holder. A second thermocouple senses the external temperature of the air and sets it as a reference while the vapor pressure in the sample chamber reaches equilibrium (see Fig. 2.7). The thermocouple in the sample chamber then looks for the dew point temperature in the chamber and gives an output proportional to the differential temperature between the dew point and the external temperature. This temperature depression is a function of the vapor pressure of the analyzed solution (which in turn is a linear function of the osmolality) and is given by the relation $\Delta T = \Delta e/S$. ΔT is the dew point temperature depression in degree Celsius, measured as a voltage signal by the thermocouple and then multiplied by the thermocouple responsivity. Δe is the difference between saturation and chamber vapor pressure. S is the slope of the vapor pressure temperature function at ambient temperature, given by the relation $S = e_0\lambda/RT^2$,

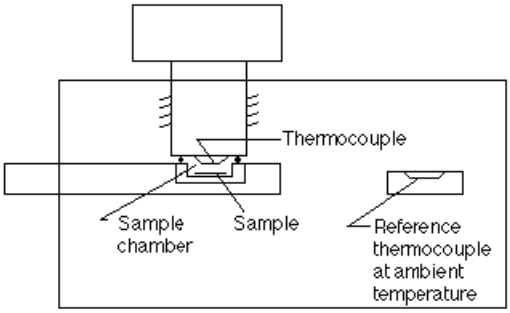

FIGURE 2.7: Sketch of the major components of a vapor pressure osmometer. [157].

where e_0 is the saturation vapor pressure, λ is the latent heat of vaporization, R is the universal gas constant and T is temperature.

In the dilute regime, the molal concentration is referable to osmotic pressure by van't Hoff law, $\pi = CRT$, where C is the osmolality in mol/kg and $RT = 2.446\ kg \cdot MPa/mol$ at 21 °C and π is measured in MPa, as in reference [100]. I verified that for the concentration of PEG I used, the polymers are in the dilute regime and van't Hoff relation is applicable. The maximum concentration of PEG I used for my experiments is 5.62% w/v of PEG 200 Da, corresponding to 0.028 mol/L. One molecule of PEG 200 Da is composed of 4 monomers of size $a = 0.35\ nm$. PEG 200 Da is a short polymer, but as a reference, De Gennes [43] scaling for long polymers suggests that the switch from dilute to semidilute solutions occurs at concentration $c^* = 1/(N^{4/5}a^3) = 12.8 mol/L$ of PEG 200 Da, that is much larger than the highest concentration I used. These arguments are consistent with measures obtained in [124] with a freezing point osmometer and in [100].

2.4 Strains and media

Wild type *Bacillus subtilis* NICB3610 bacteria were used for all biological experiments. For each experiment I extracted a small sample of bacteria with a sterile pipette tip from stocks kept at −80°C, I streaked them on TYE agar medium and let them grow in a 30°C incubator overnight. Once single colonies appeared, bacteria were grown in shaking TYE medium at 37°C from 4 to 6 hours. OD_{600} was measured with Novaspec III Visible Spectophotometer and bacteria were diluted to an $OD_{600} \simeq 1$. MSgg medium [8] was prepared and poured into the setups or the Petri dishes, solidified through addition of 1.5 % agar. The plates were then dried at 20°C for 24h before bacteria deposition.

MSgg medium is a mixture of different salts, aminoacids and sugars (recipe in Appendix B). All solutions need to be sterilized (autoclaved or filtered) before use. I first autoclaved the needed quantity of water with 1.5% agar and then added all salts and other components when agar mixture temperature dropped to ~66°C. To avoid salts precipitation during the media preparation, I mixed Msgg manually before pouring it into each plate. For Petri dishes, (25 ± 0.5) *ml* of Msgg were used for every plate. For setups, (42.5 ± 0.5) *ml* of Msgg were poured in each setup. During the tests and experiments, all samples were stored for at least 36h at a controlled temperature of 30°C.

2.5 Experimental protocol

In order to run one experiment per week, my work required planning and a systematic checklist. Here I expose the single steps of the protocol, which will be described in more detail in annexe B.

Day 0:

- Clean bottles from residues of solutions with surfanios: leave bottles one hour with surfanios inside, then rinse with distilled water;
- clean tubes and connectors with EtOH 70% + distilled water;
- wrap bottles and other pieces of equipment in aluminum foil an take them to the autoclave service.

Day1:

- prepare missing solutions for MSgg preparation (if needed).

Day 2:

- take back bottles from autoclave service;
- sterilize set-up and metal sticks;
    1. clean it with surfanios and distilled water and leave it for one hour in this solution;
    2. rinse with EtOH;
    3. sterilize under hood with UV lights for 30 minutes.
- sterilize set-up plastic box (this is a box where I store the set-up when I take it from IBV to INPHYNI. I use it just to protect the setup):

1. rinse with EtOH and let it dry under the hood;
2. sterilize under hood with UV lights for 30 minutes.

- prepare Mssg + 1.5% agar or variants (i.e. with PEG):
  1. autoclave water + agar 1.5%;
  2. prepare solution with other components and leave it at room temperature;
  3. make autoclave water + agar 1.5% cool down in hot bath at 60 °C.
- prepare plates + set-up with its cover;
- leave under hood for 24h face up;
- after 18h00: take bacteria out of -80 °C freezer, streak them on Petri dishes with TYE medium and put them in incubator at 30 °C, then wait up to the moment where colonies start to be visible (or not more than 14 hours) before taking them out of the incubator.

Day 3:

- before 10h00: take bacteria out of incubator at 30 °C and put them in 5 ml TYE in shaking incubator at 37 °C, then wait for about 4h;
- prepare solutions for Mariotte's bottles:
  - use Msgg recipe without agar, removing required volume of water when solution needs to be mixed with PEG 200 Da;
  - add from 0 to 5% PEG 200 Da at max to solutions, depending on needs;
  - filter sterilize with Stericup filters;
  - put filtered solutions in autoclaved bottles using a flame next to you.
- after 4h measure TYE + cells solution OD and take it to 1;
- remove metal sticks from setup;
- plate bacteria solution into set-up and control Petri dishes, wait for it to dry;
- wrap setup and Petri dishes in parafilm and put them in the sterile plastic box prepared the day before;

- take everything to InPhyNi;
- set-up the experiment:
  - connect all components with each other, always next to a flame;
  - rinse every now and then gloves with EtOH;
  - make flow start.

day 4-5:

- check the experiment, remove bubbles.

day 6 = day 0

- take osmotic pressure measurements;
- start again protocol from day 0.

2.6 Imaging and image analysis

Samples were imaged with 8-bit greyscale photographs taken every hour by a multifocal objective Navitar TV Zoom 7000 equipped with a camera system (PixeLINK PL-B74 1280x1024 Resolution) assembled on a motorized stage mounted above the Plexiglas chamber and controlled through a custom-made LabView interface, developed by Gregory Sauder (InPhyNi, Nice).

I performed image analysis with ImageJ v1.50 and following versions. I developed this protocol to analyze them:

1. Original images were imported in ImageJ as a stack.
2. The length scale was set in the image stack using the image of a ruler taken during the experiment as reference. The ruler was originally positioned on the same plane as the biofilm-agar interface during the experiment.
3. Images in the stack were aligned using "Linear Stack Alignment with SIFT" plugin [88].
4. A rectangular selection of 800×500 pixel was selected and cropped, in order to have the biofilm in the center of the frame and selection was duplicated for the whole stack.

5. The first image of the duplicated stack was subtracted from the whole duplicated stack using "Difference" function from *Image Calculator* command, which gives as result of the operation $img3 = |img1 - img2|$ in pixel values, leaving visible only the difference in grey values between the background and the biofilm shape (see fig.2.8b).

6. The resulting image was adjusted manually in brightness and contrast in order to underline the edge of the biofilm.

7. The images were thresholded and converted to binary using the "Triangle" method [180] (see overlayed selected area in fig.2.8d). The threshold was selected manually in order to underline every biofilm feature, including the thin layer that appears in some of the experiments (see fig. 2.9 as example). When the threshold is applied, all grey scale values are binarized (grey scale values above and below threshold are converted respectively into 0 and 1 respectively.

8. The biofilm surface was measured using the *Analyze particles* command. Biofilm with a surface of 2 mm^2 or smaller where not taken into account to avoid artifacts. When necessary, biofilm surface was selected manually.

This analysis produces as output a stack of binary images representing the biofilm measured surface (see fig.2.8e) and a text file containing the area dimensions in mm^2, the coordinates in mm of the centroid positions, and the stack position of the measured area. I chose this method as it seemed the more effective and reproducible to obtain quantitative data from the images. I chose to perform point 3 for the following reasons: first to correct the shift of 2 or 3 pixels that the camera sometimes performs from its original position; second to correct displacements that I imposed involuntarily when monitoring the experiments. I chose to perform point 5 to correct non uniform background illumination and to enhance the actual difference between the background and the biofilm. Before using this protocol I was selecting manually the area of the biofilm for each picture, as it was impossible when binarizing the image to separate the biofilm from the background. This old method works pretty well, but it is hardly reproducible and relies mainly on the eyes of the observer, increasing the chance of error. Moreover the method I finally used is much faster than the manual one.

Binary images of the biofilm taken at intervals of 6h were then imported into Matlab v2017b and analyzed with custom made scripts. I used one script to locate the center of mass of the biofilm for each frame and visualize it, to

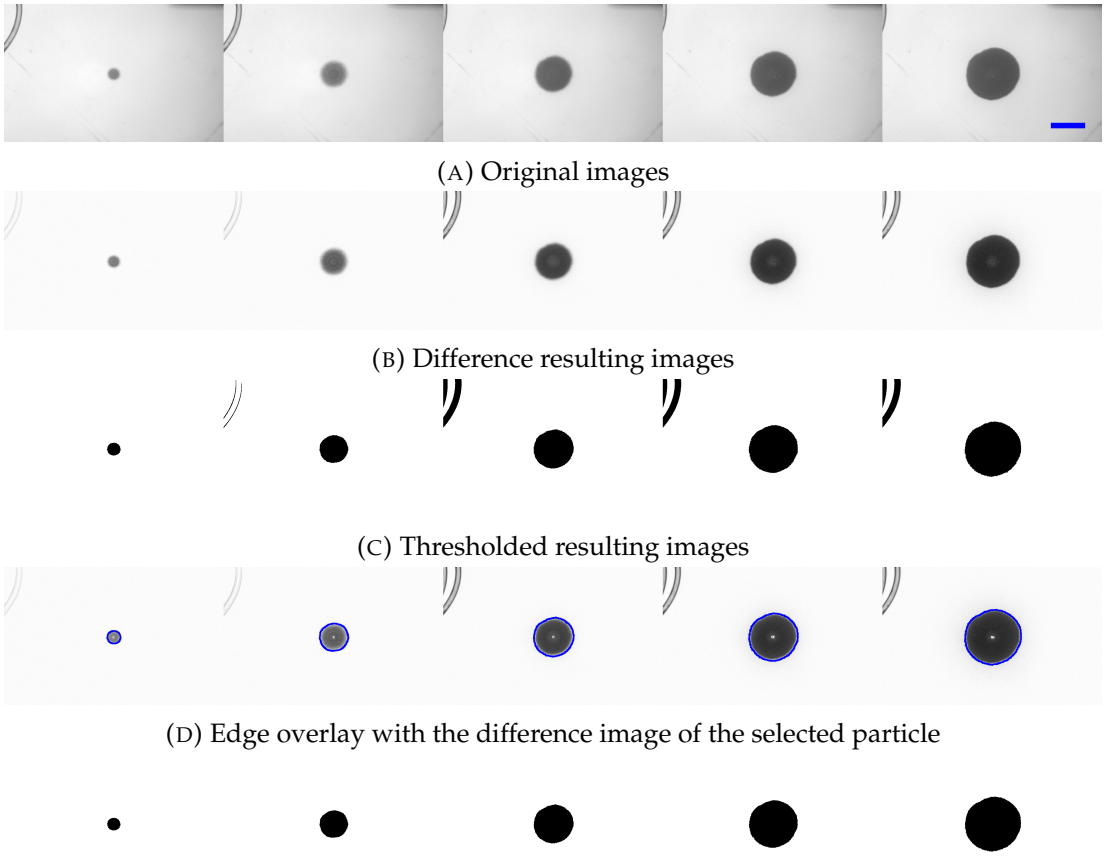

(A) Original images

(B) Difference resulting images

(C) Thresholded resulting images

(D) Edge overlay with the difference image of the selected particle

(E) Mask of the measured area

FIGURE 2.8: Example of image analysis sequence. Scale bar is 1 cm.

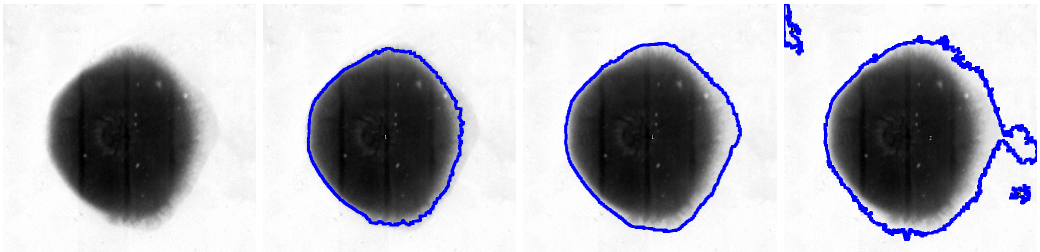

(A) Original image (B) Low threshold (C) Right threshold (D) High threshold

FIGURE 2.9: Example of biofilm edge and artifacts selection when different thresholds are applied.

verify that the displacement of the colony happens along the same direction of the gradient, and to quantify biofilm contour as it grows in time. For each selected frame, the script measures the distance ρ between the points on the biofilm leading edge, and the center of the biofilm at the time when the biofilm starts to be visible in the pictures. The calculated distance is plotted as $\rho = \rho(\theta)$ where ρ is the distance module and $-180^\circ < \theta < 180^\circ$ is the angle for which ρ is measured. I used then a second script to plot the average $\rho(\theta)$ for each type of experiment.

Chapter 3

Results

3.1 *Bacillus subtilis* biofilm morphology on gradients

When grown on homogeneous agar plates, biofilm develop a symmetric shape expanding radially on the surface. In *B. subtilis*, this behavior is driven at the biological level by expression of genes implicated in secretion of polymeric matrix combined with the physical transfer of water and nutrients suction from the substrate. In order to fit the experimental data of biofilm expansion on agar, a minimal model was proposed where production of biomass was the driving mechanism of expansion, and growth was described at small deviations from osmotic equilibrium. These deviations due to osmotic gradients are counterbalanced by intake of water, where water flow is ruled by conservation laws for mass and momentum. If a biofilm grows symmetrically when absorbing water and nutrients from an isotropic medium, and this growth is driven by local osmotic pressure gradients between the biofilm and the media, then what happens if the biofilm is in contact with a medium where there is a gradient of nutrient, or osmotic pressure? To our knowledge, this question has not been previously considered and biofilms have never been exposed to controlled osmotic gradients. Fig. 3.1 shows a sketch of the cross section of two biofilms:

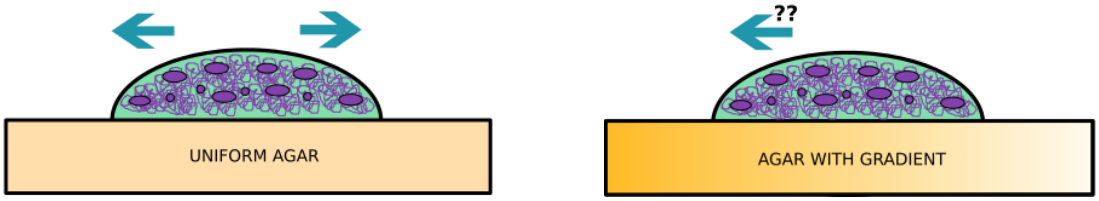

(A) Symmetric morphology on homogeneous agar plate.

(B) Unknown morphology on external chemical gradients.

FIGURE 3.1: Sketch of biofilm growing on agar in two different cases.

one growing in contact with an isotropic substrate and the other in contact with an anisotropic substrate. As I will show below, the expectation from the model in reference [129] would be that the biofilm may expand toward or against the external gradient of osmotic pressure, depending on whether physical or biological effects are more important. The first step to find out which is the case requires the development of an experimental setup, where the gradient in the agar medium can be reproducibly created and controlled in a sterile and temperature-controlled environment. In this chapter, I will present the results of my experiments for the development of the osmotic gradient and for bacteria growth in contact with a gradient of osmotic pressure. I will then conclude this part with final remarks and future perspectives.

3.2 Prediction from theory of osmotic spreading

I report here the main results for the theory of osmotic spreading put forward in [129], adapted to the case where an external osmotic gradient is applied. This theory captures correctly the initiation of biofilm spreading. After the initial vertical growth, the biofilm spreads horizontally. The late stages are likely affected by the dynamics at the contact line [129][153], that initially can be overlooked in the model as the biofilm is growing without changing its radius. If the external gradient perturbs growth without altering it dramatically, the thin film approximation of the equations of motion described in chapter 2 remains valid, with parameters that now depend on space as well as time:

$$\partial_t h - K(r,\theta)\frac{R}{r}\left[rh^3(gh)_r\right]_r = g(r,\theta)h \tag{3.1}$$

where $h(r,\theta,t)$ is the height of the biofilm at location defined in polar coordinates by the distance from the center r and azimuthal angle θ and time t; $g(r,\theta,t)$ is biomass production rate; R is biofilm radius and $K(r,\theta)$ is the sole non-dimensional parameter of the theory and depends on the equilibrium with the external environment:

$$K = \frac{1}{3(1-\phi_\infty)^2}\frac{\mu_w}{\mu_b}\frac{h_0^3}{\xi_\infty^2 R_0} \tag{3.2}$$

Here ϕ_∞ and ξ_∞ are the biomass volume fraction and mesh size in the biofilm when this is in equilibrium with the agar, hence these quantities depend on the environmental conditions; μ_b and μ_w are the dynamic viscosities of biomass and water respectively; h_0 and R_0 are the initial height and radius of the biofilm. Equation 3.1 is a non-linear diffusion equation with biomass

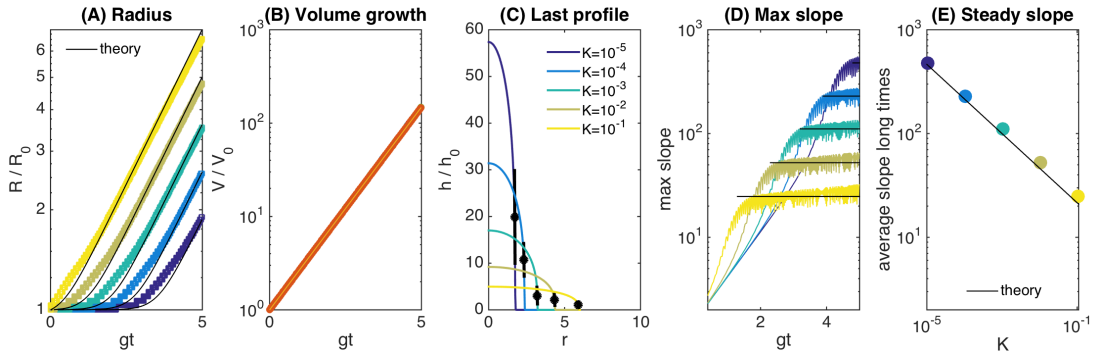

Colors indicate 5 different simulations obtained for different values of K from 10^{-5} to 10^{-1} color coded from dark blue to yellow. (A) evolution of biofilm radius in time compared with theoretical prediction from self similar solution; (B) exponential growth of volume normalized by its initial value; (C) Profile of the biofilm after 5 division times, with indication of the point of maximum slope, defining biofilm radius; (D) evolution of maximum slope in time, plateauing at a finite value, as expected; (E) plateau value for the slope as a function of the parameter K. The larger K, the smaller the slope and the faster the spreading.

FIGURE 3.2: Results of finite difference simulations of equation 1 with constant parameters g and K recovers the self similar solution obtained in[129].

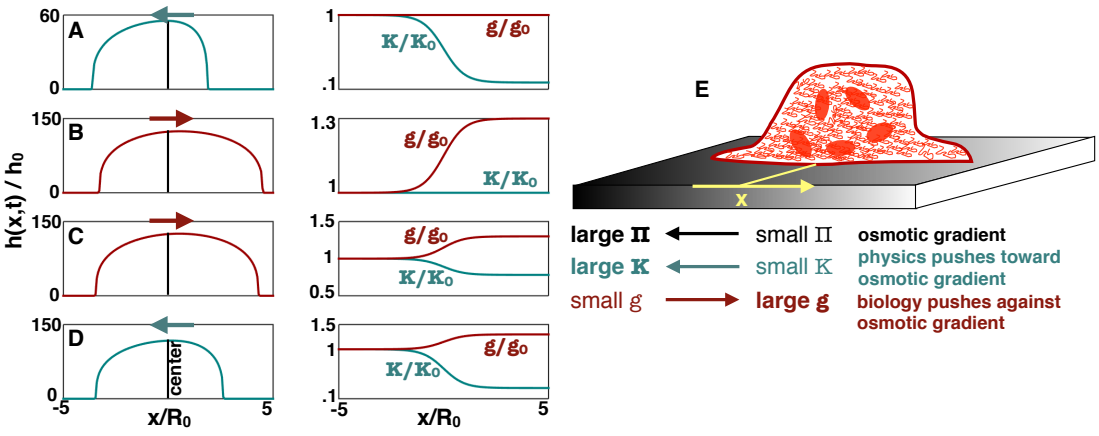

Left column: Biofilm profile after 5 division times, $t = 5/g_0$, normalized by bulk height at time 0 (h_0), obtained from numerical simulations of equation 3.3 with g and K varying in space. Right column: profile of g and K in space, normalized by their values g_0 and K_0 at the left edge. (A) At constant g and varying K the biofilm translocates toward the osmotic gradient; (B) at constant K and varying g the biofilm translocates against the osmotic gradient; (C)-(D) when both g and K vary, the direction of translocation depends on which of the two parameters dominates. (E) Sketch of gradients in the biofilm: at high osmotic pressure, K is expected to increase and g is expected to decrease.

FIGURE 3.3: Biofilm profile for different g and K.

growth and variable coefficients and cannot be solved analytically. We solve this equation with the built-in Matlab routine *pdepe* (which uses finite element methods to compute derivatives in space and an implicit scheme for time integration) [132]. We use a large domain, with no flux condition at $r = 0$ and $h = 0$ for $r \to \infty$. Note that this last boundary condition causes the maximum slope of the biofilm to saturate at a finite level, as predicted in [129]. The effects of varying environmental conditions can be understood by comparing simulations with different values of g and K, considered constant in space. In this case, we recover the results of [129] (see Fig. 3.2). Given g, larger K corresponds to faster expansion (compare purple and yellow in Fig. 3.2C). On the other hand, if K is kept constant, larger g corresponds to faster expansion, see e.g. green curve in Fig. 3.2A, where radial growth is shown as a function of gt, hence when g is large, expansion occurs at an earlier dimensional time t. To confirm this picture and illustrate the effects of an uneven osmotic environment on biofilm morphology, we simulate eq. 3.1 in one dimension, which reads:

$$\partial_t h - K(x)R[g(x)h^3 h_x]_x = g(x)h \tag{3.3}$$

where $h(x,t)$ is the height of the biofilm as a function of distance from the center, x, and time t. We solve this equation with Dirichlet boundary conditions at $x \to \pm\infty$, and using different forms of the coefficients K and g with x. Fig. 3.3 shows that when g is constant the biofilm expands toward large K (panel (A), left and right), whereas when K is constant the biofilm translocates toward large g (panel (B), left and right). But when a biofilm is exposed to gradients of osmotic pressure in the environment, both K and g vary in space with an opposite pattern (see sketch in Figure 3.2(E)). K varies because of the physics of osmotic equilibrium: regions of the biofilm in contact with a higher osmotic potential have large K because equilibrium with the environment occurs at a larger biomass volume fraction ϕ_∞ and smaller mesh size ξ_∞. From the relation 3.2 it is clear that K in these regions is large, as $(1-\phi_\infty)$ and ξ_∞ would be very small. Conversely, K at low osmotic pressure is small. On the other hand, biological response to osmotic pressure is expected to affect g in the opposite way: [124] demonstrated that *B. subtilis* pellicles downregulate matrix expression at large osmotic pressure, hence g is large when the osmotic pressure is small. Additionally, nutrient flows into the colony due to osmotically driven water flow, and this effect is larger at low environmental osmotic potential, which will further enhance growth in these regions (as shown in [178]). In summary, physics causes K to be disproportionately large at high

osmotic pressures, which works to push biofilms toward these regions. Biology works in the opposite direction, causing large g at low osmotic pressures and pushing the biofilm that way. Who wins? Whether the biofilm translocates toward or against external osmotic environments depends on the relative magnitude of variations in g and K; in Figure 3.3(C-D) I show two examples where either g or K wins. At later stages, the detailed dynamics of the contact line must be modeled in order to obtain predictions for the spreading rate. Osmotic spreading pushes the biofilm outward; but once spreading starts, the bulk soon reaches the contact line, and radial expansion slows down with respect to the exponential prediction put forward in [129]. In this regime, the contact line likely limits expansion and the details of the wetting properties of agar with and without added polymers should be considered [153]. In particular, the spreading velocity in this case is linear in the wettability parameter that measures the relative importance of wetting and entropy, and can be inferred from the contact angle, the height of the prewetting layer and the mesh size [153]. Experiments including the full profile of the biofilm are beyond the scope of my thesis and are left for future studies.

3.3 Heterogeneous agar plates

As the goal of my thesis is to investigate what happens to bacterial growth in contact with a gradient of osmotic pressure, it is important to ensure reproducibility of osmotic pressure gradients in a gel medium. In subsection 2.3.2 I presented the numerical simulations I developed to predict the concentration of a molecule, diffusing in agar, when a gradient is imposed at its bottom. Here I will list all the experimental results I obtained using the final prototype of my setup. Results of experiments using the old prototype are discussed in Appendix A.

3.3.1 Fluorescein gradient

Fluorescein is an organic dye usually available in the form of red powder, that once dissolved in water gives it a yellow to green color, depending on the quantity used. To test if the experimental setup was correctly generating chemical gradients, we decided to first use solutions of fluorescein and water, so that the eventual gradient could be quantified through image analysis. For the substrate, I used distilled water solidified with 1.5% agar. For the solutions

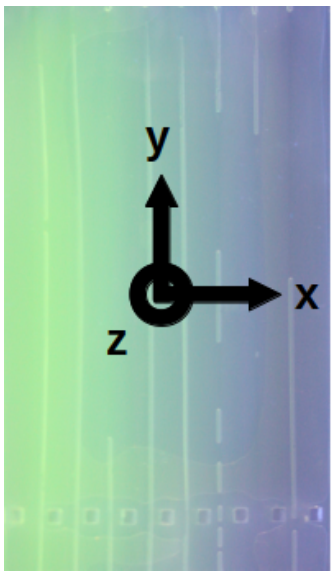

(A) Raw color picture of agar with gradient of fluorescein and *xyz* refence used.

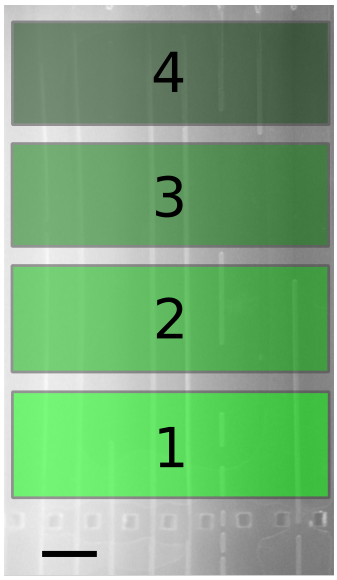

(B) Green color channel of image in (A). Areas 1 to 4 are selected to be analyzed.

FIGURE 3.4: Test of fluorescein gradient. Scale bar: 1 cm.

in the bottles, I used distilled water combined with linearly increasing concentrations of fluorescein and PEG. Fig. 3.4a is the picture of the agar surface at the end of the experiment, exposed to a UV light source. The experiment was conducted for 24h. I took the picture with a Canon EOS 450D using an exposure time of 1/4 s. As fluorescein emits in the green color wavelength (λ = 520-530 nm), I split the RGB color channels and I analyzed with ImageJ only the green channel. Fig. 3.4b shows the green channel extracted from the picture in Fig. 3.4a. In order to verify that the gradient does not depend on the position along the y-axis, I selected four areas (1 to 4 in Fig. 3.4b) and computed the light intensities averaged in the y-direction, across these four areas. The light intensity incident on the biofilm, I_0, is computed summing the average of the image intensity in the blue and the red channels of Fig. 3.4a. For a uniformly concentrated layer of fluorescein solution, the intensity of the signal I/I_0 depends on the concentration of fluorescein. In Fig. 3.5 I/I_0 is plotted as a function of x is shown for the four areas, demonstrating that the gradient depends on x only, as expected. The color code used in fig. 3.4b and 3.5 is similar: light colors correspond to areas next to the inlet (area 1) and progressively darken towards the outlet (area 4). The small spikes in the image correspond to artifacts for the presence of channels. Indeed, once disconnected from the fluid circuit, channels get filled with air and appear brighter than the agar gel,

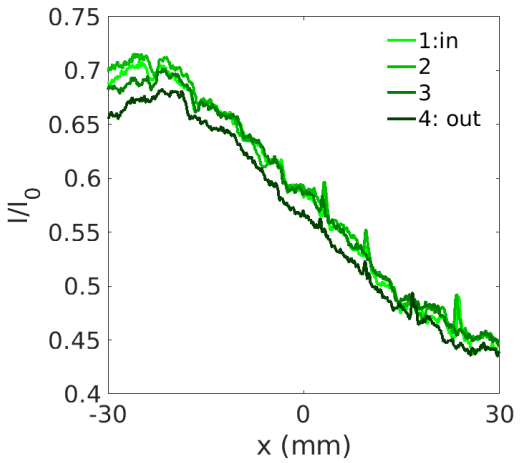

FIGURE 3.5: Light intensities of the green channel in the areas selected in 3.4b normalized with respect to the sum of the light intensities of the blue and red channels values in the same areas.

which corresponds to a larger value in the grey scale. These data show that the gradient is stable along the y direction of the setup and preserves the linear slope imposed across the channels.

3.3.2 Osmotic gradients: tests

To run tests on the gradient of osmotic pressure, I poured distilled water solidified with 1.5% agar in the setup and I prepared solutions with distilled water combined with concentrations of PEG 200 ranging from 0% to 5% v/v concentration. I chose to avoid using MSgg [8] for these test in the interest of time and also because the compounds required are much more expensive and longer to prepare than simple mixtures of water and PEG. Fig. 3.6 shows the average values of osmolarity in $mmol/kg$ on the top surface of the agar, measured with the vapor pressure osmometer as described in Chapter 2. Fig. 3.6 represents the average concentration of PEG molecules as a function of x, at different times from the beginning of the experiment (left column: 0h black, 24h magenta, 48h cyan) and at different distances from the inlet (right column: 2.5 cm from inlet red, 2.5 cm from outlet blue, note setup is 10 cm long. The xyz reference is the same as used in Fig. 2.6 and 3.4a. At two different distances from the inlet, concentration was measured in eight points, by placing eight filters at the x coordinates of the channels, as in Fig. 2.6. Fig. 3.6a shows the average and standard deviation in the case of a linear gradient obtained across three trials. Fig. 3.6b and fig. 3.6c show test performed imposing a step and a spiked gradient respectively.

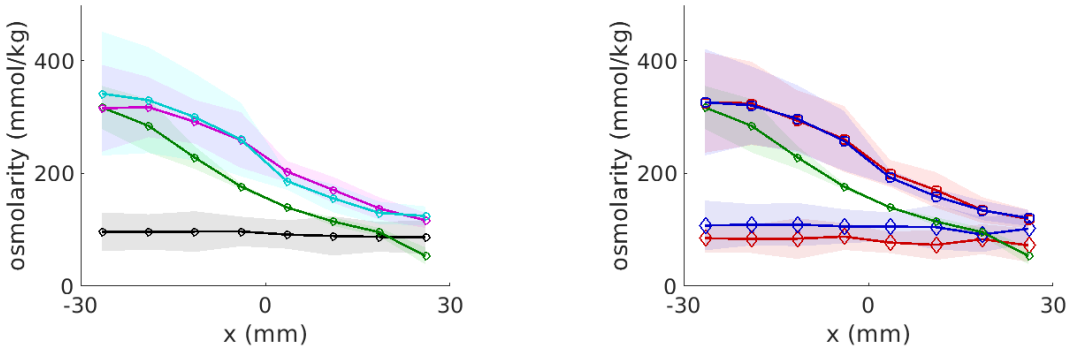

(A) Linear gradient in time and space

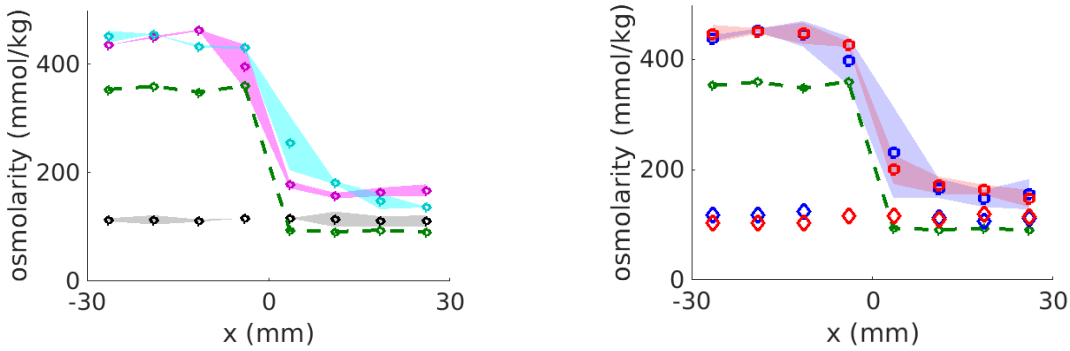

(B) Step gradient in time and space

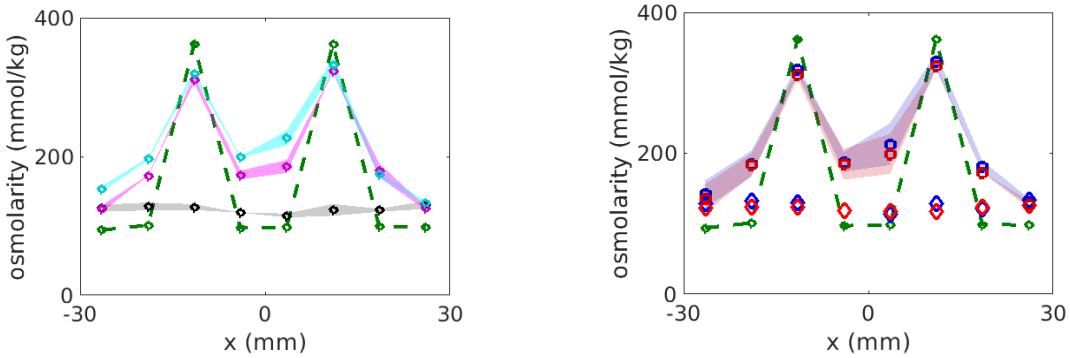

(C) Spiked gradient in time and space

Left: values of osmolarities obtained by averaging over the two lines, one closer to the inlet and one closer to the outlet (see sketch in Fig. 2.6). Dots: Black: agar 0h, magenta: agar 24h, cyan: agar 48h, green circles and dashed lines: solutions flowing through channels for 48h. Right: values of osmolarities obtained by averaging measures at 24h and at 48h. Red dots: agar close to inlet, blue dots: agar close to outlet, Red diamonds: agar close to inlet at 0h, blue diamonds: agar close to outlet agar close to inlet at 0h. Green circles and dashed lines: solutions flowing through setup.

FIGURE 3.6: Left: values of osmolarities measured at different times. Right: values of osmolarities measured at different locations on the setup. Shades represent standard deviation (A) and standard error ((B) and (C)).

These two tests were performed once, to verify that it is possible to impose

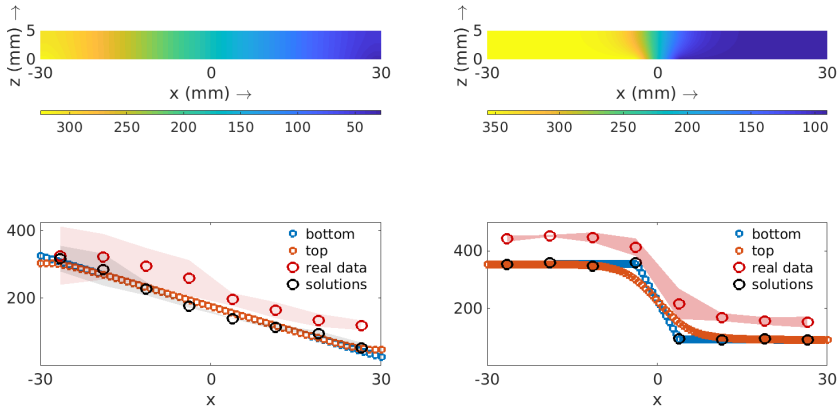

(A) Test linear gradient. (B) Test step gradient.

FIGURE 3.7: Data of osmolarities compared to result of numerical simulation.

gradients with different shapes. I have two measures for each experiment. In Fig. 3.6b and Fig. 3.6c, the dots represent the average between these two values and the shades represent the absolute difference between the two values measured for each point.

All the gradients represented in 3.6 show good agreement with the concentrations imposed in the different channels, stability over a long period of time (left column) and over a the setups length (y direction) (right column). In all panels in 3.6, the green dots represent the PEG concentration in the solutions flowed though the channels. Concentration in the solutions results slightly smaller than the concentration in the gel. Part of the reason is because the gel itself generates a non-zero value of osmolarity, probably because not all the agar polymers are entirely cross-linked, and some may dissolve thus contributing to the effective concentration. Part of this discrepancy can be attributed to instrument limitations when measuring effective concentration values between 0 and 200 $mmol/kg$. This effect is visible also from superposition of data with numerical simulations (Fig. 3.7a and 3.7b), but disappears when using MSgg instead of pure water, as osmolarity values are higher than 200 $mmol/kg$ (see Fig. 3.10). I simulated the gradient imposed at the bottom fitting the real data with straight lines. I cannot correct for osmolarity caused by the agar gel, because the osmometer is not reliable at small concentrations. Except for this shift, simulations agree well with real data in this case as well.

A big advantage of our millifluidic device, is that it is expected to be extremely robust with respect to changes in the flow rates across the different channels. The flow rate should simply be non-zero, but different flow rates will not impact the dynamics. Indeed, solutions need to flow in the channels

in order to preserve a fixed boundary condition for the concentration of polymers. As long as the flux is non-zero, and fast enough so that polymers in the channels are neither diluted nor concentrated, the system is expected to preserve the imposed gradients. In order to verify this expectation, I also measured the flow rates at the end of the millifluidic circuit. Fig. 3.8 shows the flow rate measured in $\mu L/min$ and the correspondent averaged osmolarity values. Both flow rate and osmolarity are shown as a function of channel position in order have the same horizontal axis in 3.8a and 3.8b. The osmotic gradient is stable despite large fluctuations in flow rate, hence there is no apparent correlation between flow rate and osmolarity on top of agar, as expected.

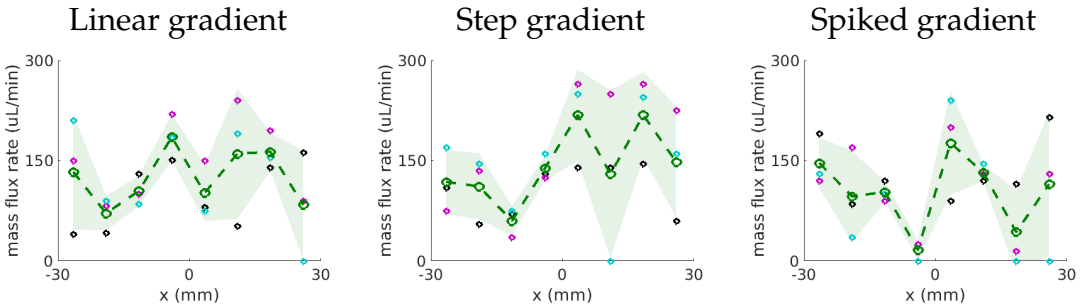

(A) Flux rates measured at different times during the experiments. Black: 1h, magenta: 24h, cyan: 48. Green dots and line: average, Green shade: standard deviation

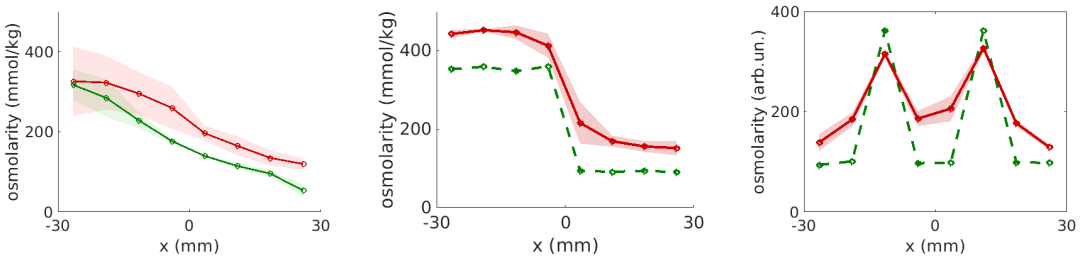

(B) Measures of osmolarity averaged across 48h. Red: average osmolarity in agar; green dots and lines: osmolarity in the solutions. Red shade: standard deviation.

FIGURE 3.8: Osmotic gradients are robust with respect to the solution flow rate in the channels. Left: linear gradient, average over 3 samples, center: step gradient; right: spiked gradient.

3.3.3 Osmotic gradients in experiments with biofilms

In experiments with bacteria, it is not possible to measure concentration of polymers on the surface of agar during the advancement of the experiment, because this would certainly perturb biofilm growth and cause contamination. Instead, I measured the effective concentration at the end of each experiment. Each experiment lasted from 30h to 48h. I prepared eight different solutions of

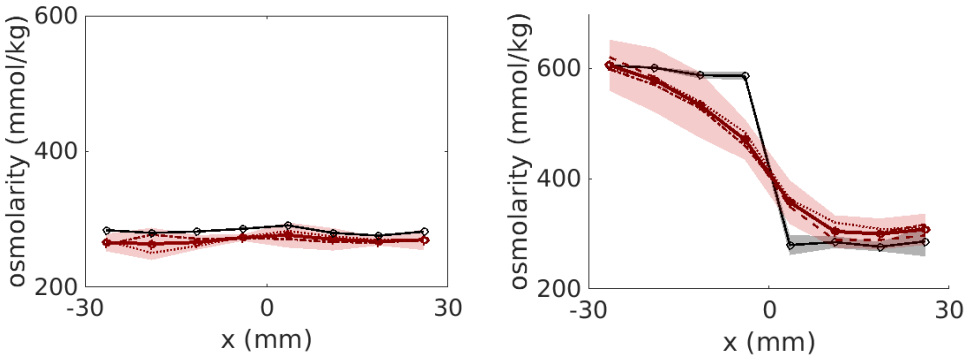

(A) Experiment with flux and no gradient (B) Experiment with flux and gradient

FIGURE 3.9: Values of osmolarities for injected solutions and agar in two different experiments. Black: flowed solutions; red: agar. Shades: standard deviation.

MSgg medium with a variable amount of PEG 200 Da, and I measured polymer concentration using the vapor pressure osmometer as described in section 2.3.3. In Fig. 3.9 the black circles and lines represents the osmolarity measured in the solutions flowed into the channels, whereas the red circles and lines represent the osmolarity measured on agar. For the control experiments in Fig. 3.9a, I used eight solutions of MSgg with no PEG and data are average values from in three different setups. For the experiments in Fig. 3.9b, I used four solutions of MSgg with 5% vol/vol concentration of PEG 200 flowed in four channels ($-30 < x < 0\ mm$) and four solutions of normal MSgg flowed in the other four ($0 > x > 30\ mm$). The data are collected from six setups. The values of concentration measured in the control experiment in the absence of gradient (Fig. 3.9a) are comparable to those in the $x > 0$ region of Fig. 3.9b, which further confirms reproducibility of the data. There is good agreement between the measured gradient and the one expected from numerical simulations of diffusion in agar, as shown in Fig. 3.10. Concentration of PEG at the bottom of agar undergoes an abrupt change at $x = 0$ as imposed by the concentrations in the channels; this abrupt change is smoothed out by diffusion, and results in a more gradual osmotic gradient at the top surface of agar. Data accord well with predictions with only slight deviations between $x = 15\ cm$ and $x = 0\ cm$.

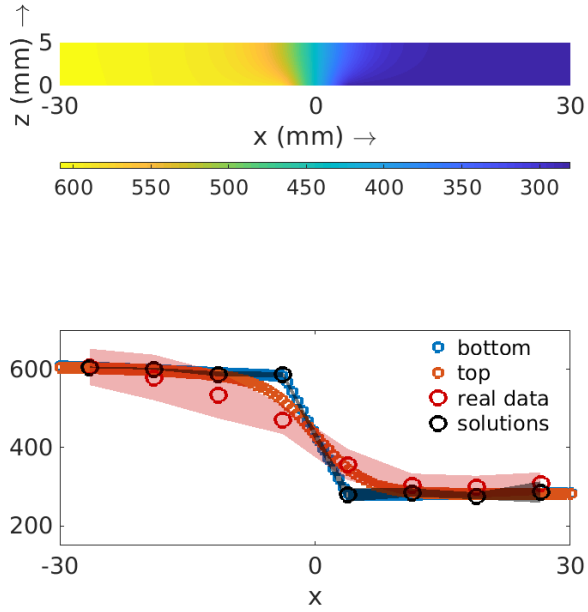

FIGURE 3.10: Superposition of real data over numerical simulation of diffusion in the xz plane. Blue dots: border condition imposed at $z = 0$; red small dots: numerical solution at $z = H$; red big dots: osmolarity measured on agar, black dots: osmolarity of liquid solutions injected; shades: errorbar.

3.4 Morphology of biofilms growing on osmotic gradients

The data produced during an experiment consist in a collection of 8-bit greyscale pictures of (1280 $\times$ 1024) pixel resolution, taken with a frequency of 1 picture/hour. An example of the resulting pictures is given in Fig. 3.11 for different experiment cases. Rows represent different conditions in the substrate. Columns represent time when the picture was taken. I analyzed the images using the methods described in section 2.6. Data analysis yielded (i) binary images of the colonies surfaces, (ii) the surface area, (iii) the coordinates of the centroid positions and (iv) the stack position (which corresponds to the time from the beginning of the experiment).

3.4.1 Temporal evolution of area

Fig. 3.12 represents the average surface area of a biofilm in time. Different colors correspond to different experiments, where biofilms were grown: in the presence of flux and osmotic pressure gradient (red), in the presence

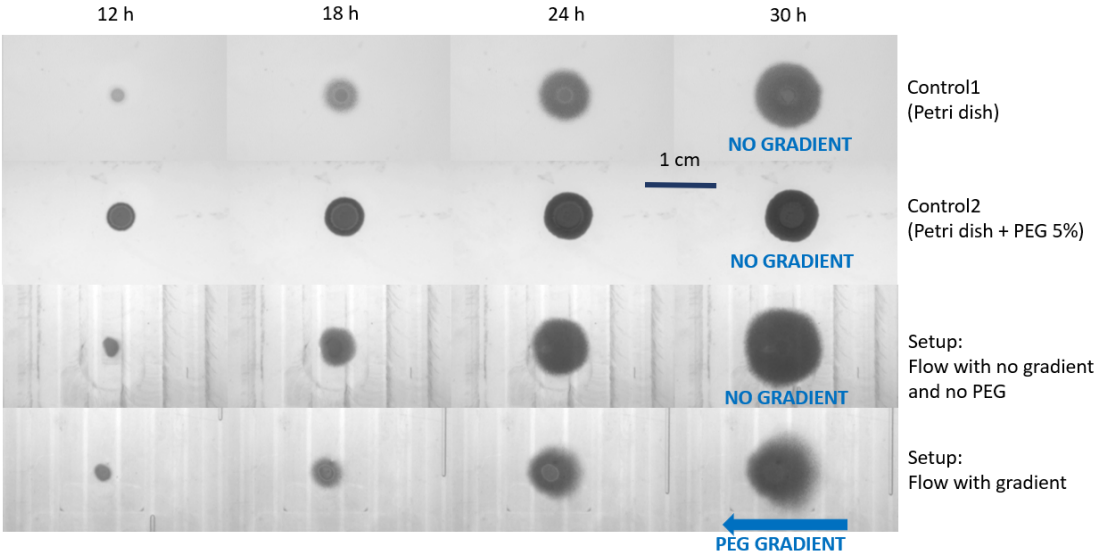

FIGURE 3.11: Examples of images collected during different experiment, at progressing hours, for different substrate conditions.

of flux and no osmotic pressure gradient (blue), in Petri dishes with normal MSgg-agar medium (yellow), in Petri dishes with MSgg-agar and a homogeneous concentration of 2.5% v/v PEG 200 Da (cyan) and in Petri dishes with MSgg-agar medium and a homogeneous concentration of 5% v/v PEG 200 Da (green). At initial times (6-12h), biofilms growing in setups with flux (red and blue) and controls growing in Petri dishes at different conditions (yellow, cyan and green) show a similar behavior. After 12h, the biofilms in the Petri dishes grow slower than biofilms in setups. This can be related to nutrient limitation in the Petri dish. The difference in rate of growth between biofilm in petri dishes on normal MSgg-agar medium and biofilm in petri dishes on MSgg-agar medium and PEG can be imputed to the higher osmotic pressure in mediums with PEG, that limits suction of water and nutrients by the biofilm, and that is in agreement with [7]. This last phenomenon happens also in pellicules grown on MSgg liquid medium [124].

The analysis of the average surface area of biofilm colonies contain no information about a potential translocation of the biofilm in the direction of the gradient, which is the essential feature I target with my experiments.

3.4.2 Biofilm translocation on osmotic gradients

To quantify the displacement, I used a custom-made Matlab script that reads the binary image of a single biofilm produced with ImageJ as input. It selects

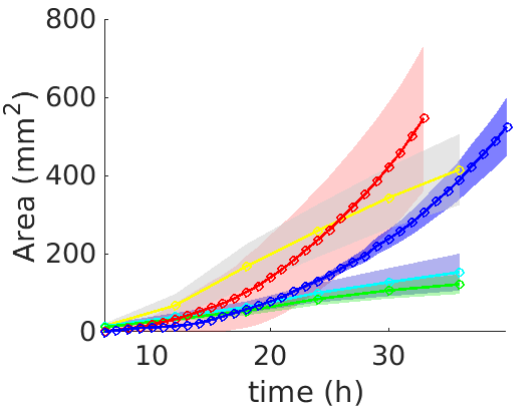

FIGURE 3.12: Evolution of area of the biofilms with time. Red: bacteria in setup with gradient; blue: bacteria in setup with flux without gradient and without PEG; yellow: bacteria in petri dish; cyan: bacteria in petri dish with 2.5% PEG 200 Da; green: bacteria in petri dish with 5% PEG 200 Da. Shades: standard deviation.

the mask of the biofilm for each snapshot and define its contour (with the instruction *contour()*). The script then calculates the center of mass as the average of the x and y coordinates of the pixels within each mask. Finally, the scrips plots the contours and centers of mass of the biofilm.

Fig. 3.13 (top) shows two examples of biofilm contours and centers of mass at different times, as well as the corresponding concentrations in the agar (bottom). Contour and center of mass are shown for t= 12h, 18h, 24h and 30h, color coded from yellow (12h) to blue (30h). Initially, a drop of bacteria suspension is deposited in at coordinate $x = 0$, which is where the biofilm eventually appears: hence the biofilm is centered initially at the center of the slope of the osmotic gradient in the agar. Fig. 3.13a shows no significant displacement of the center of mass of the biofilm, consistent with the fact that this colony is growing in an homogeneous osmotic environment in the absence of a gradient. On the contrary, Fig. 3.13b shows that the center of mass of the biofilm shifts toward the positive x values with time, hence moving against the osmotic gradient. Fig. 3.14 shows all the biofilms I grouped for experimental condition. Fig. 3.14A shows biofilm grown in contact with a step gradient (see Fig. 3.13b), 3.14B shows controls grown on Petri dish with MSgg-agar, 3.14C shows controls grown on Petri dishes with MSgg-agar with 2.5% v/v PEG 200 Da and 3.14D shows controls grown in the millifluidic setup with flow and no gradient (i.e. all bottles contain MSgg medium and no PEG). For visualization purposes, I show snapshots every 6h, color-coded from yellow (12h) to blue (30h). Nine out of eleven biofilms grown in contact with the step gradient

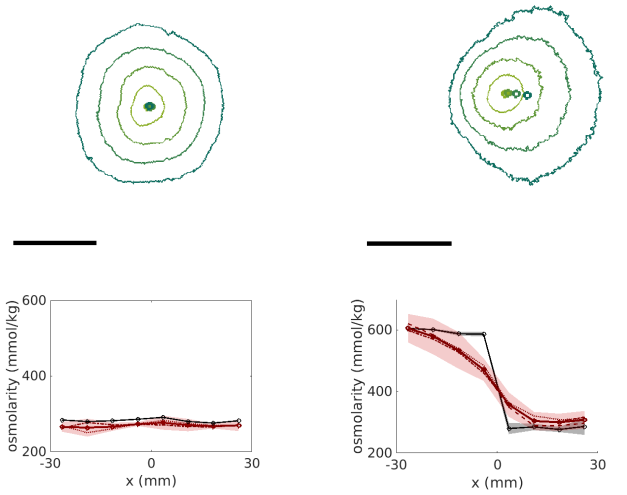

(A) Experiment with flux and no gradient

(B) Experiment with flux and gradient

FIGURE 3.13: Top row: corresponding example of biofilm contour and center of mass evolution over time. Contours are plotted at 12h (yellow), 18h, 24h and 30h (blue) in each column. Bottom row: average values of osmolarities for injected solutions and agar in two different experiments. Black: flowed solutions; red: agar. Shades: errorbar.

show a significant shift in the position of the center of mass, whereas controls grown in contact with a homogeneous environment show no displacement of the center of mass. To move beyond visualization, the next step consisted in quantifying the displacement of the center of mass.

As shown in 3.14A, the displacement of the center of mass occurs both in the x and y direction. I then compared biofilm translocation along the direction of the gradient (x) and orthogonal to the direction of the gradient (y) (see Fig. 3.15). I used the centroid positions obtained from the ImageJ analysis described in the previous chapter and calculated the average displacements in the horizontal and vertical directions for each biofilm. Fig. 3.15 represents the average displacements along x (red) and y (blue) with their respective standard deviations for all the different experiment conditions. Fig. 3.15a shows the experiment with the step gradient: in 8 out of 11 biofilms, the center of mass first translocates slightly towards higher osmotic pressure (0.05 to 0.76 mm), contributing to a slight negative translocation of the center of mass (which is not significant when averaged over all colonies, as this transient occurs at different times for each colony and not for all colonies). Eventually, all colonies tranlocate toward the positive x-axis (average displacement (1.9 ± 0.9) mm, whereas the average displacement of the center of mass along y remains close

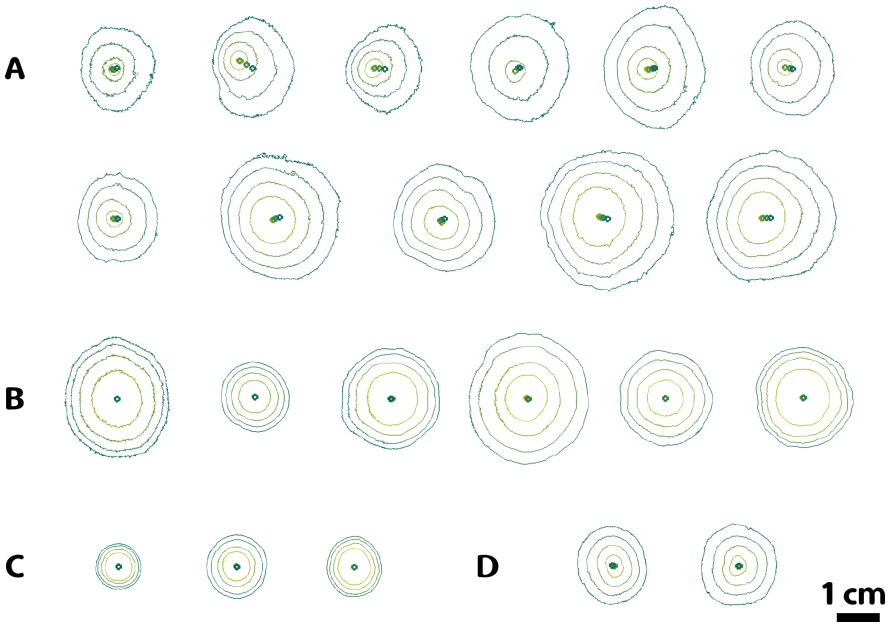

FIGURE 3.14: Biofilms analyzed (A) in presence of flux and osmotic pressure gradient , (B) in Petri dishes with normal MSgg-agar medium, (C) in Petri dishes with MSgg-agar medium with 2.5% v/v PEG 200 Da (D) in presence of flux and no osmotic pressure gradient

to zero. This analysis shows that while the biofilm translocates reproducibly along the x direction where the osmotic gradient is imposed in the agar, it may translocate sometimes toward the inlet and sometimes toward the outlet which results in no net y displacement on average. This comparison supports the hypothesis that the displacement of the center of mass is mainly driven by the external osmotic gradient and not by potential artifacts including e.g. a water flux on the agar surface caused by the underlying millifluidics. Controls grown in homogeneous osmotic environments show no displacement (see Fig. 3.15b). This result further corroborates the hypothesis that osmotic gradients drive the observed displacement.

3.4.3 Biofilm contour

In order to complement the information regarding displacement, I proceeded to compare the shape of the contour. I first defined the location of each point on the contour labeled by its angular position $\theta \in [-\pi, \pi]$ with respect to the horizontal line as sketched in Fig. 3.16. Consistent with the convention throughout the thesis, the positive x-axis corresponds to $\theta = 0$, and defines the direction where I impose the external osmotic gradient. For each snapshot, I computed

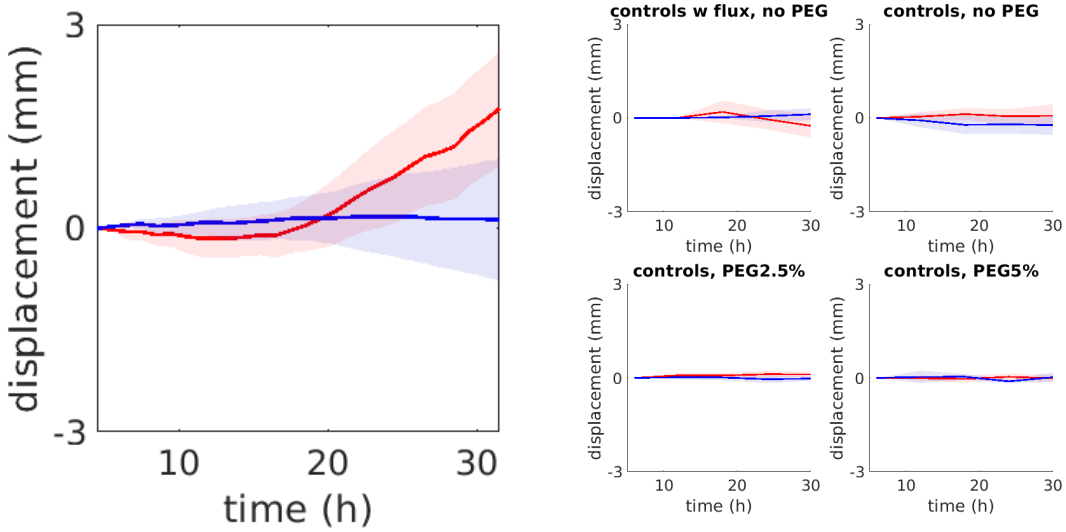

(A) Experiments with gradients.

(B) Controls with no gradient.

FIGURE 3.15: Displacement of the center of mass. Red: displacement along the x direction; blue: displacement along the y direction.

the distance $\rho(\theta)$ of each point on the contour from the center of the biofilm defined at t=0 (shown in Fig. 3.17 center). To compare different biofilms, I normalized surface area to unity, and defined the normalized biofilm contour by calculating the normalized distance $\rho^*(\theta)$ (shown in Fig. 3.17 right). For a perfectly circular biofilm, $\rho^*(\theta) = 1/\sqrt{\pi}$ for all values of θ and all times, whereas deviations from a circular biofilm correspond to deviations from this flat line.

Fig. 3.17 shows the results of this analysis. Rows represent different conditions; columns represent from left to right: an example of biofilm contours and centers of mass for each condition, $\rho(\theta)$ and $\rho(\theta)^*$. As for the previous

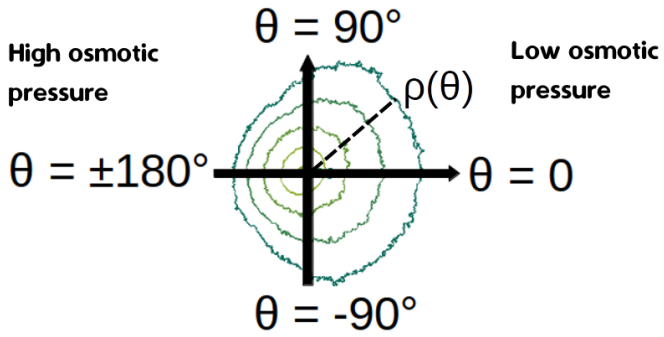

FIGURE 3.16: Scheme of the convention for the angle $\theta \in [-\pi, \pi]$ that defines points along biofilm's contour.

results, time is color-coded from light green (12h) to dark green (30h). Dashed lines and shades correspond to average and standard deviation of biofilm contour computed on all biofilms grown under the same conditions. In the third column the scale is the same for all figures. These results show that when a gradient of osmotic pressure is applied (Fig. 3.17a), ρ increases faster in the region near $\theta \approx 0$ corresponding to low osmotic pressure, and more slowly in the regions near $\theta \approx \pi$ corresponding to high osmotic pressure. Consistently, $\rho^* > 1/\sqrt{\pi}$ near $\theta \approx 0$, whereas $\rho^* < 1/\sqrt{\pi}$ near $\theta \approx \pi$. Note that the very first curve in Fig. 3.17a (light green) shows a weaker pattern in the opposite direction that is $\rho^* \lesssim 1/\sqrt{\pi}$ near $\theta = 0$ and $\rho^* \gtrsim 1/\sqrt{\pi}$ near $\theta = \pi$ that is consistent with the initial translocation toward higher osmotic pressure show in Fig. 3.15a.

None of the controls produced a significant deviation from the circular shape. Biofilms grown in the millifluidic device with no imposed gradient (Fig. 3.17b) appear more noisy than controls in Petri dishes (Fig. 3.17c,3.17d,3.17e). This is likely a genuine effect, although I did not pursue quantification of border instabilities, which would require much more statistics (in Fig. 3.17b, I am including data for two colonies). Deviations of the normalized distance ρ^* from $1/\sqrt{\pi}$ are present at early times, likely due to the initial condition, and vanish at later times when both colonies become circular. In all the other cases, when a gradient is not applied and biofilm are growing in Petri dishes (Fig. 3.17c,3.17d,3.17e), the value of ρ^* is stable around $1/\sqrt{\pi}$ for the entire length of the experiment and the errorbar is very small. These results confirm that biofilms may translocate first, transiently, toward osmotic gradients, but they eventually move against osmotic gradients imposed in their environment.

3.5 An interesting observation to be analyzed further

In the analysis I presented above, I focused on the first 30 hours of the experiment. In fact, at later times, I reproducibly observed an interesting phenomenon that deserves further inspection. Fig. 3.18 shows a typical old biofilm growing on my millifluidic device with the step gradient osmotic pressure as described above. Contamination appears reproducibly in all of my experiments under these conditions and I observe new colonies of what clearly appears as *B. subtilis* biofilm across the entire surface. I hypothesize that this phenomenon is driven by one biological and one physical factor. On the one

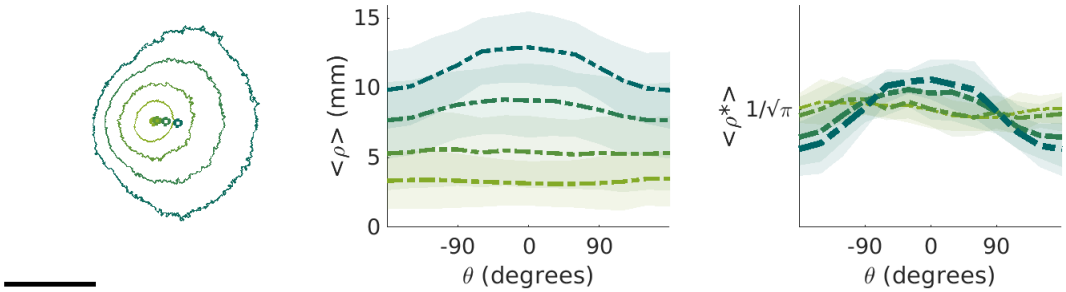

(A) Experiments on millifluidic setup with flux and a step gradient of PEG 200 Da.

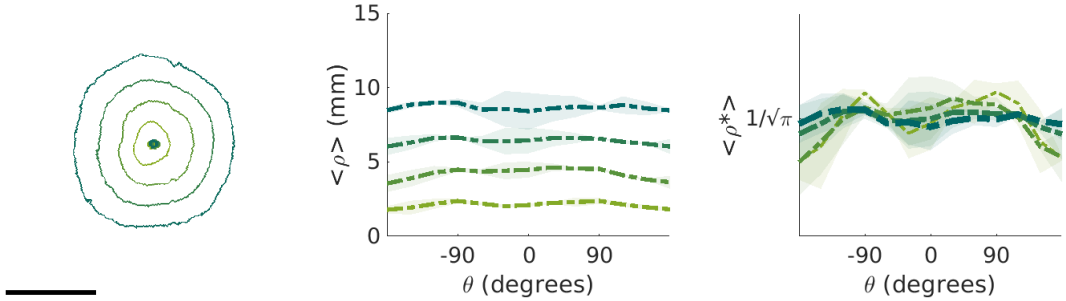

(B) Controls on millifluidic setup with flux and no osmotic gradients.

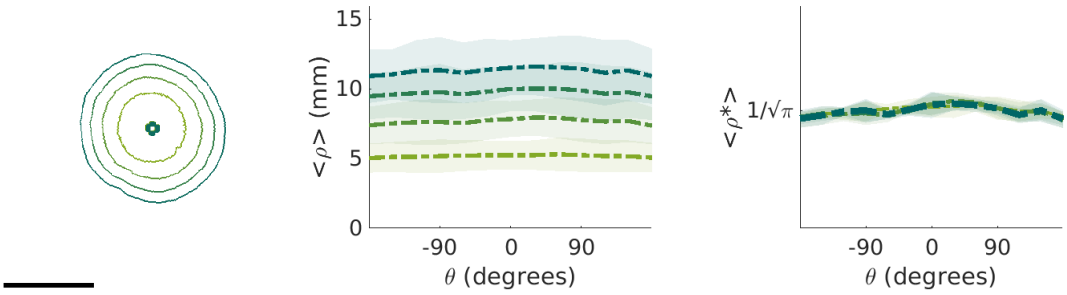

(C) Controls in Petri dishes with MSgg-agar.

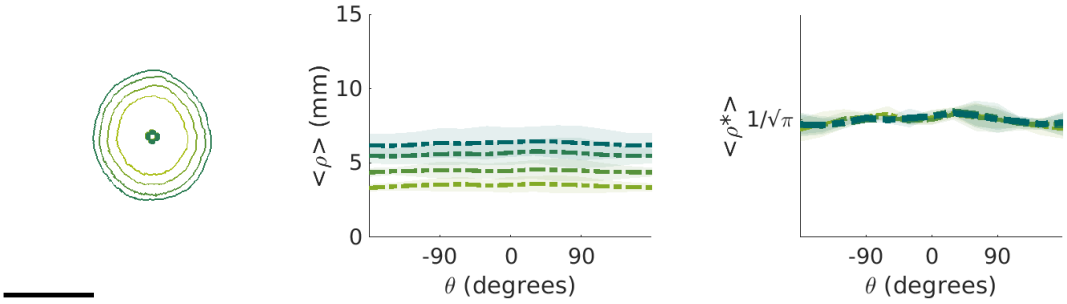

(D) Controls in Petri dishes with MSgg-agar and PEG 2.5%.

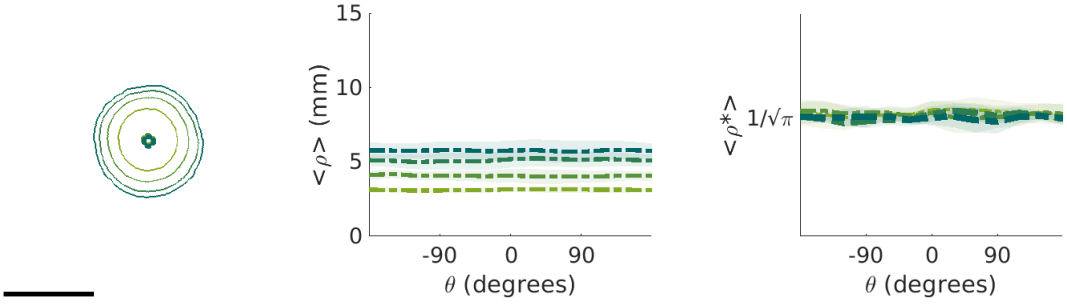

(E) Controls in Petri dishes with MSgg agar and PEG 5%.

Figure 3.17: Left: An example of biofilm contour and relative center of mass. Center: $< \rho(\theta) >$ at 12h,18h,24h,30h. Right: $< \rho(\theta)^* >$ obtained by normalizing the surface area of the biofilm to 1 at 12h,18h,24h,30h. Horizontal axis corvers the range $\theta \in [-\pi, \pi]$.

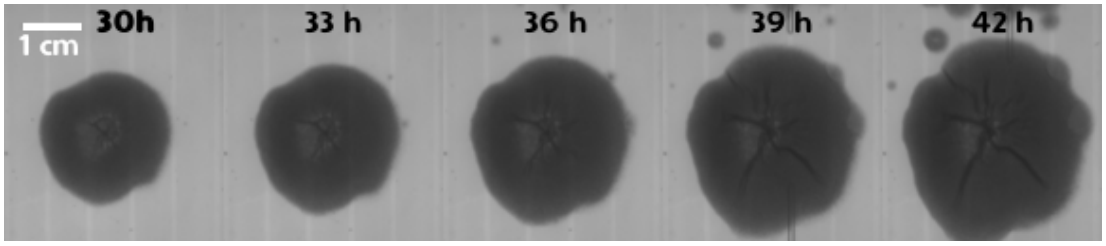

FIGURE 3.18: Example of contamination appearing at late times in one of the experiments with gradients.

hand, large osmotic pressures have been shown to inhibit matrix production in a KinD dependent way. Correspondingly, *B. subtilis* cells at high osmotic pressure transition quickly into sporulation, earlier than on low osmotic pressure [124]. However, a quick and potentially more effective sporulation is not sufficient to explain the contamination shown in Fig. 3.18. Indeed, I only observe this effect on my millifluidic setups, and not in control experiments on Petri dishes with any percentage of PEG. I hypothesize that enhanced sporulation is coupled to additional physical effects that allow spores to spread on the millifluidic device. Although in the interest of time I did not pursue further experiments, I believe this will be an interesting direction to understand biofilm disassembly and spore dissemination.

3.6 Conclusions

All the results are in good agreement with the hypothesis that biofilm spreading depends on gradients of osmotic pressure. The prediction from previous results [129] [153] is that biofilms translocate toward or against external osmotic gradients depending on the relative importance of three effects. *(i)* Equilibrium with the environment depends on the osmotic pressure in the substrate; at larger osmotic pressure, the biofilm is in equilibrium with the substrate at large biomass concentration and small mesh size. This effect causes the bulk of the biofilm to initiate expansion more quickly at large osmotic pressure, hence pushing the biofilm *toward* the external osmotic gradient. *(ii)* On the other hand, osmotic spreading pushes the biofilm towards the regions where the biomass growth rate is larger. And because biofilms overexpress matrix at low osmotic pressure, this effect pushes the biofilm *against* osmotic gradients. This effect is at play both at osmotic spreading initiation [129] and at later stages dominated by the dynamics of the contact line [153]. *(iii)* At

these late stages, gradients in the wetting properties of the substrate may also be relevant [153].

My results suggest the following hypothesis: *(i)* may often cause a small translocation toward large osmotic pressure at early stages, although the effect is small, but then *(ii)* and potentially *(iii)* take over, and eventually the biofilm translocates reliably toward small osmotic pressure.

These results suggest further experiments to corroborate this picture: it would be interesting to monitor matrix gene expression on these heterogeneous environments, as well as measuring the height of the biofilm close to the contact line to measure contact angles and monitor potential gradients in wetting induced by either the external environment or the biological response. With the protocol I developed, it is now possible to first tune the conditions (temperature, agar medium, polymer concentration) to maximize this effect, ad then observe the effect of other shapes of osmotic gradients. Potentially, this could lead to principles to develop controlled patterning of biofilm growth on surfaces, which could be used in the long term to direct biofilm growth toward or away from regions of interest.

Osmotic spreading is a fundamental physical mechanism and applies to other species of bacteria and fungi [28] [154][178]. Hence the methodology and ideas developed here could be applied to other species to ultimately test whether biofilms take advantage of osmotic spreading to direct growth toward the best conditions for their growth.

Part II

Fungal Spore dispersal

Chapter 4

Introduction

So far, I have focused my research on understanding how bacteria translocate when they are in contact with a gradient of osmotic pressure. In this second part, I will introduce another research topic that I decided to address, the spore dispersal in a particular phylum of the fungal kingdom, called Basiodiomycota. This part of my research took about ten months of my PhD, and it was conducted in strict collaboration with Prof. Anne Pringle and her group at University of Wisconsin-Madison, where I spent eight months between 2016 and 2017.

Fungi, together with Animals and Plants belong to the Eukaryota domain. These organisms usually grow in soil and dead matter and include among them molds, yeasts and mushrooms. They have an important role in ecology, as they can be saprotrophs (i.e. they break down decomposing matter in simpler compounds), mutualistic symbionts of animal and plants or parasites. As symbionts, they have an important role in exchanging nutrients with plants, in a symbiotic association where the fungus provides phosphorus and other compounds from the soil and the tree provides carbohydrates from photosynthesis (mycorrhizal association). They are widely employed in food industry: yeasts are used for bread, wine and beer fermentation. Finally, they are also a source of food in the form of edible mushrooms and truffles [169].

Interestingly, Fungi were classified as part of the Plants kingdom from the beginning of taxonomy classification by Linnaeus in 1735 [84] until exactly 50 years ago [172]. The mistake seems understandable when we think about fungi, especially mushrooms: they are motionless, rooted into earth and they disperse spores like plants disperse seeds. But despite looking more similar to plants at first sight, they are genetically closer to animals [161] and may have separated from them about 900 million years ago [5]. Unlike plants, they do not photosynthesize and they are heterotrophs, i.e. they require to absorb nutrients from the external environment. The main component of the fungal cell wall is chitin, rather than cellulose found in plants. But, similar to plants,

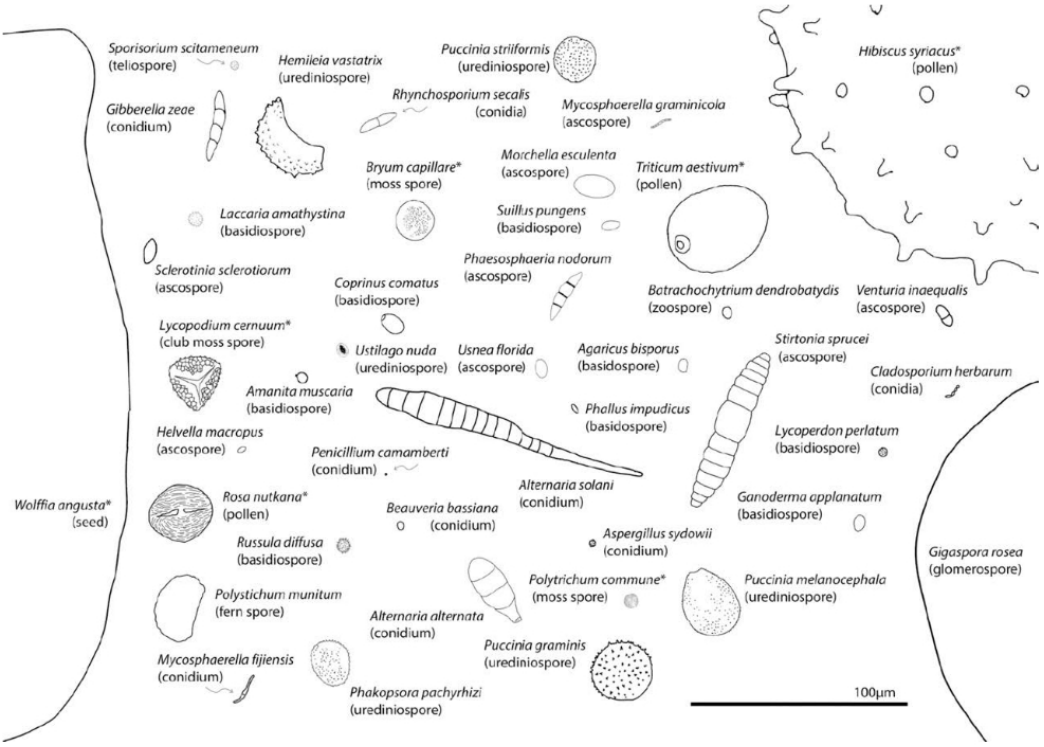

FIGURE 4.1: Sizes of fungal spores and other airborne particles. Some species are wind dispersed (e.g., *Puccinia graminis*), while others have other means of dispersal (e.g., *Gigaspora rosea*). The smallest plant seed, *Wolffia angusta*, the pollen grains of *Hibiscus syriacus* and *T. aestivum*, and a glomerospore of the arbuscular mycorrhizal *Gigaspora rosea* are provided for comparison. Species labeled with an asterisk are not fungi [44].

fungi also have a cell wall, although their composition is different. As fungal cells are more closely related to animal cells than bacteria are, it is difficult to develop antifungal drugs effective against fungal cells without the side effect of impacting also human cells.

This kingdom expresses a huge biodiversity, however, little is known about its true extension. The real number of existing species is estimated to be between 500,000 and 10 million [58]. Different species are able to survive in very different environments. This resistance and distribution ensures the presence of fungi all over planet Earth and affects most ecosystems [30], as fungi are major decomposers, but can be also pathogenic. In recent years, new fungal diseases affecting crops and animals have started to attract the interest of researchers more and more, as they cause losses of million of dollars of food waste and affect animal survival and ecosystem equilibra [109] [75] [39]. Fungi are mainly immobile and hidden within a substrate. In the case of mushrooms, the fruiting body is only a small part of the whole fungus, compared to the

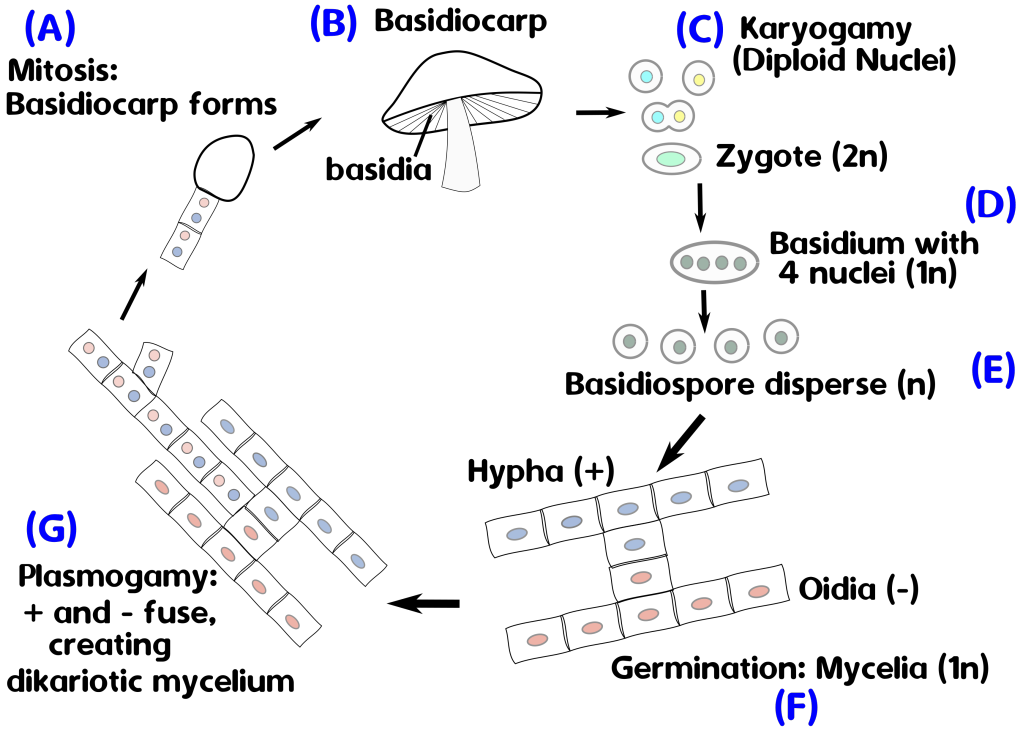

(A) The basidiocarp develops from a secondary mycelium and produces an high number of basidia on the surface of its gills beneath the cap of the basidiocarp (B). (C) Badidia maturate and combine their nuclei (karyogamy), producing a zygote with a diploid cell. (D) Through meiosis, each basidium produces four basidiospores, each containing a single haploid nucleus. (E) Basidiospores are discharged by the surface-tension catapult mechanism. (F) Discharged basidiospores germinate to form haploid (monokaryotic) mycelia with simple transverse septa. (G) Plasmogamy (i.e. the fusion) between the hypha and the oidium forms a dikaryotic mycelium. If environmental conditions allow it, the dikaryotic mycelium eventually produces a basidiocarp (A).

FIGURE 4.2: Semplified diagram of the life cycle of a basidiomycete, inpired by [169].

mycelium that grows as a net within the soil and whose extension can be of several square meters. Because of their immobility, their only way to reproduce and travel far from a particular location is to release numerous spores in the air [44]. Spores can be dispersed in such high concentrations that they can cause allergies and respiratory diseases [76]. Once released, spores are then carried more or less far away from the sourcing sporocarp by wind. When a spore lands on a favorable host, it is important for it to be still alive in order to germinate and extend its life cycle. The colonization of the host happens then through development of a system of tubes called hyphae, that from branches to build up the mycelium. However, fungi can grow less frequently also as discrete yeast cells, thallus or plasmodium [169]. To get an idea of the multiple shapes spores can have, see Fig. 4.1.

Among fungi, one of the biggest phyla is the one of Basidiomycetes. They are among the most common fungi and fill very different ecological roles. Most

of them grow in land soil and have spores dispersed by wind, but some of them grow in water or marine habitats. They include among them pathogens as *Puccinia graminis* (wheat stem rust) and *Phakospora pachyrhizi* (Asian soybean rust), as well as hallucinogens such as *Amanita muscaria* and *Psilocybe* spp. They can be mycorrhizal associates or saprothophs. The phylum is defined by basidiospores. The basidiospores are sexual spores (i.e. the result of nuclear fusion and meiosis, see Fig.4.2) whose size range is between 3 and 20 μm. They are packed on the gills of mushroom fruit bodies caps, usually attached in groups of four (but the number goes from one to nine) to a basidium by subtle excrescences called sterigma, connected to a single spore via a hilum. Spore shape and color can vary from one species to an other, going from almost spherical and transparent to an almond-like shape with dark pigmentation. The spore walls can be smooth or jagged [169]. In my work, I focused only on woodland mushrooms with a gilled cap. This part of my thesis focuses on how the spores of Basidiomycetes may be related with the mushroom gills morphology. In the next section I will explain more in detail how these spores are released by the fruit body for most of the Basidiomycetes species.

4.1 Basidiospore discharge

Most of the Basidiomycetes use as dispersal mechanism for their spores a system know as ballistospore discharge, or surface tension catapult, where the spores are actively ejected away from basidia. This mechanism was originally proposed by Buller [14] and Ingold [59]. Typically, the ejection happens once a drop of liquid, known as Buller's drop and formed extracellularly at the base of a spore, reaches a critical size and collapses onto another drop, called adaxial drop and formed above Buller's drop, along the longitudinal axis of the same spore [99] [116]. This coalescence produces a larger liquid drop that effectively reduces the total surface of the two drops. The released energy is thus converted to kinetic energy transmitted to the spore, which is ejected horizontally away from the basidium and the gill (or pore) that held it within the mushroom. The spore is rapidly decelerated by air resistance. After traveling horizontally for a short range (typically less than 2 mm), the spore then falls vertically and ends up underneath the mushroom cap where it can reach dispersive airflows to be carried away [99]. This trajectory has been named sporabola, and the horizontal range of the spore right after discharge must be small enough that spores do not hit the opposite gill surface once ejected. The discharge of basidiospores has been an interesting phenomenon for scientists

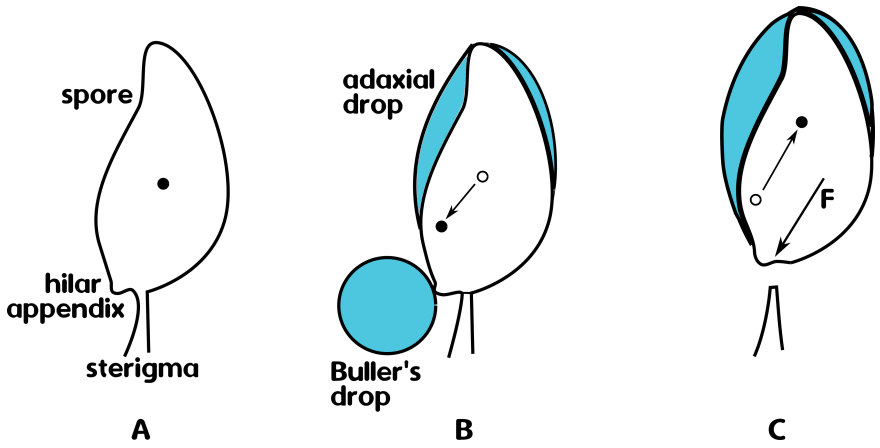

(A) the spore is attached to the sterigma before the Buller's drop formation. The black circle represents the center of mass. (B) The Buller's drop appears at the hilar appendix and the adaxial drop forms on the spore wall, both increasing in size. The center of mass of the spore-drop complex moves towards the hilar appendix. (C) The two drop coalesce, the center of mass of the spore-drop complex moves rapidly away from the hilar appendix and the spore-drop complex acquires kinetic energy and momentum thanks to the reduction of surface energy, exerting a force on the sterigma (F). The spore-drop complex is thus ejected away from the hilar appendix.

FIGURE 4.3: Sketch of the events associated with ballistospore discharge. Image readapted from [169].

since over a century by now. It was first observed by Schmitz in 1843 [127]. The first one to observe this mechanism in more detail was Buller at the beginning of the 20th century. He described the development and the discharge of a spore, observing the secretion of a drop at the hilum (the junction between the spore and its sterigma) preceding the discharge of the spore together with the drop [14]. Further statements need to wait up to the arrival of camera recording. Webster et al. presented photographic evidence of a drop of liquid forming at the hilar appendix right before discharge, proposing a two-phase mechanism for spore ejection: the first phase involves the liquid drop wetting the spore surface, acquiring momentum; the second involves the sharing of momentum and movement of the center of mass of the spore-drop complex due to the rapid wetting. This redistribution of mass and consequent resulting momentum is what ejects the spore-drop complex away from the sterigma [167]. Pringle et al. discuss a similar mechanism where the energy and directional momentum of the drop-spore complex are given by the release of surface tension at the moment of coalescence between Buller's drop and a second drop present on the side of a spore (adaxial drop) [116]. The two merging drops coalesce and move to the distal end of the spore, exerting a force on the sterigma, generating a rotation of the spore towards the drop and the following ejection [116]. Noblin et al. proposed a four-stage ballistospore ejection

mechanism. This starts with the growth of the Buller's drop and the motion of the center of mass of the spore-drop complex towards the end of the sterigma. It is then followed by the early coalescence of the adaxial drop and the Buller's drop, which generates two forces of equal magnitude but opposite direction exerted by the spore and the drop. The momentum of the resulting merged drop is transferred to the spore during the late stage of coalescence, putting the hilum under tension and eventually breaking it [103]. The common characteristics of the above-described models is that they are purely based on an energetic balance and give no information about the launching direction of the spore. Recent publication integrating the model with simulations and experiments states that the Buller's drop surface reduction releases surface energy and gives momentum to the spore-drop complex, while the launching direction is dictated by the spore adaxial plane orientation [85].

4.2 The reasons behind the work

It has long been hypothesized that mushrooms form gills in order to increase the surface area for spore production, to pack the maximum number of spores with minimum biomass investment [14] [97] [36]. [97] and [36] modeled the effects of different gill arrangements on the total surface area for spore production. From both models [97] and [36], it appears that the cap radius, the distance between gills and the gills width affect the most the maximum gill area. The resulting configurations with the greatest possible packing efficiency would be that of a single spiral or a Venetian blind gill, that does not appear in nature, probably because these arrangements are incompatible with the radial symmetry of the mushroom caps. These works analyze only the fruit-body cap morphologies of gilled mushrooms, without developing the association with the size of the spore, although they propose it as a further development.

Some mushroom species form a single array of gills, like *Russula cremicolor*, but most of the gilled mushrooms appear to develop secondary gills when enough space between two primary gills is formed far from the stipe [36]. The spacing between the gills has an important role in the basidiospores ejection mechanism. If the distance between two gills is too narrow, once ejected a spore can impact the opposite gill. Ejection velocity is another key parameter: if the velocity is too low, the horizontal range that the ejected spore travels will be too short, and the spore will remain trapped within the gill. To achieve the optimal morphology (i.e a morphology where the maximum number of spore

is packed and ejected out of the mushroom cap) the size of Buller's drop, the size of the spore and the distance between gills should be finely coordinated.

The study of optimality in mushroom morphology is not new to biophysics. Previous work on the phylum of Ascomycetes, where ascospores are ejected out of an ascus (i.e. a fluid-filled sac) through an apical ring, shows that the dimension of the spores and the apical ring are tightly coupled to minimize energy losses during ejection [42]. In Basidiomycetes, while spore size and gill distance may be under genetic control [74], Buller's drop appears to be formed extracellularly by water vapor condensation around a hygroscopic substance execreted from the hilar appendix [170][168]. Whether or how fungi control its size remains unknown, although data reporting characteristic sizes of Buller's drop for different species suggest that individual species control size [37] [116] [140].

The goal of my work is to obtain new insights in the understanding of ballistospore discharge, aiming to better understand the role of the different morphological features involved in this physical process. In particular, I explored whether the morphologies of gilled mushroom enable maximum packing of spores within the gills. I collected mushroom of different species and measured the statistics of spore size and intergills distance to analyze if they correlate with each other i.e. if farther gills correspond to bigger spores sizes. The data were then fitted with theory that relates ejection velocity and flight time to the horizontal distance traveled by a spore from the moment of launch to the moment it begins sedimenting out from underneath the gills, as in [14] [116] [103] [37] [140] [85]. The ejection velocity is obtained through an energy balance between the surface energy released during coalescence and the kinetic energy of the spore-drop complex. As result of this balance, velocity depends on size and densities of the spore and the Buller's drop. The ballistic distance traveled by the spore is predicted by combining ejection speed and flight time of the spore-drop complex before sedimentation begins. Assuming that the criterion for maximum packing is that the spores travel exactly midway between two gills, from two of three variables among (i) Buller's drop radius, (ii) spore radius and (iii) intergill distance, the third one can be predicted. The theory generates a phase space made up of the three variables that gives the condition for maximum gill packing. The results of the real data superimposed onto the phase space will be discussed in the following chapter.

Chapter 5

Data and theory of maximum packing for mushroom caps

5.1 Data collection

To compare the theory with real data, I collected mushroom of several species directly in the field to quantify the distribution of the spore size along the cap radius and the intergills distance. I collected mushroom from several locations around University of Wisconsin-Madison Lakeshore Natural Preserve, Madison, WI, and in the Huron Mountain Club, in the Upper Peninsula of Michigan, MI with the help of the members of Pringle lab. Unfortunately, 2017 was a particularly dry year, which made the collection of the specimens difficult: most of the mushrooms I found were too old or too dry to get reliable data out of them.

To get a spore print from the mushrooms, I separated the cap from the stems and placed the caps with gills facing down onto a aluminum foil and paper and left them overnight. I then isolated samples of the spores from different regions of the spore print: close to the stipe, close to the edge of the cap and halfway between the stipe edge and the cap edge. I took images of the spores using confocal microscopy (Zeiss Elyra SLM 780 and Zeiss LSM 710) and analyzed the images with the *Analyze particles* command implemented in ImageJ to trace and measure the area of the spores. I then calculated the average spore radius as $R_s = \sqrt{S/\pi}$. To measure the distance between the gills, I took pictures of the fresh caps before taking the spore prints and then analyzed the pictures with ImageJ. To analyze the picture, I identify the center of the caps by eye and then traced manually concentric circles around it. I then used a plugin command available with ImageJ v1.51 and following called *Oval profile*. The command gives as an output the plot of the gills profile along each circle measured as grey values. I then used a custom made Matlab script to quantify the intergills distances d as the peak to peak distance minus the half width of the

peaks. The data show that the spore size changes from species to species, but does not change along the single mushroom cap. Hence, mushrooms produce spores of about the same size within the sporocarp. Also the intergills distance remains constant within the sporocarp, thanks to the appearance of secondary or tertiary gills towards the edge of the mushroom cap. The only species not showing this behavior is the *Russula spp.*, that has no secondary gills and shows an intergill distance that grows linearly with the distance from the stem edge. Among the species I measured, the intergills distance ranges from 0.25 mm to 1.5 mm, but there is no obvious correlation between the intergill distance and the size of the mushroom cap. In fact, this work started with the idea of monitoring the variation of spore size in a single individual mushroom fruit body, and comparing spores of mushrooms with and and without secondary gills. In species with no secondary gills like in *Russula spp.* sample, the distance between the gills increases proceeding from close to the stipe to the edge of the cap. Hence the dimension of either the Buller's drop or the spore should vary across a single individual in order to maintain maximum packing. Unfortunately, I managed to collect only the *Russula spp.* sample with no secondary gills, but further work could investigate this point.

5.2 Mathematical model

Ejection velocity. The ejection velocity is calculated from the balance between the surface energy released during coalescence, that is $\sim \pi\gamma R_B^2$ (γ is the surface tension and R_B is the Buller's drop radius), and the kinetic energy of the spore-drop complex, obtaining:

$$v_0 = U\sqrt{\frac{y^2}{y^3+\beta}} \tag{5.1}$$

where v_0 is the ejection velocity. $y = R_B/R_s$ is the normalized Buller's drop radius. $\beta = \rho_s/\rho_B$ is the ratio between the spore density and the Buller's drop density. $U = \sqrt{3\alpha\gamma/(2\rho_B R_s)}$ is a velocity scale, where R_s is the radius of the sphere with the same volume as the spore and α takes into account the energy dissipated to break the spore apart from the hilum. The size of Buller's drop that maximizes ejection speed is derived by imposing the derivative of 5.1 equal to zero and gives $y_{max} = (2\beta)^{1/3}$. If $1 < \beta < 2$, the equation implies that at y_{max}, $1.26R_s < R_B < 1.59R_s$. Using values of Buller's drop of 13 species of basidiomycetes taken from literature, it appears that in nature

$y_{data} = R_B/R_s \simeq 0.35 \pm 0.11$, suggesting that this fungi do not eject at the maximum speed possible predicted from theory, although other species may.

The ballistic range. Once the spore is ejected away from the gill together with Buller's drop, air drag causes rapid deceleration of the spore-drop complex and the relaxation time can be approximated by the Stokes time:

$$\tau = T(y^3 + 1)^{2/3} \tag{5.2}$$

where $T = 2R_s^2/(9\nu\overline{\beta})$. ν is the air kinematic viscosity. $\overline{\beta}$ is the ratio between the density of air and the density of the spore-drop complex. The complex is considered to be a sphere with volume equal to the sum of the spore and drop volumes. After discharge, the spore-drop complex travels an horizontal distance equal to $x = v_0\tau$, after which it stops abruptly and starts to sediment vertically out from two facing gills, following a "sporabola" trajectory.

Maximum spore packing. To successfully escape the mushroom cap, the spore must travel far enough to avoid entrapment within basidia and spores underneath it, but less far than the distance between two gills to avoid entrapment in the opposing gill. Assuming that all gills are reproductive, then the safety criterion for the intergill distance should be $d > 2x$. To pack as many spores as possible and avoid inefficient empty spaces between one gill and the other, the distance between two gills should be close to the minimum value $d \sim 2x$ where d is the intergill distance and $x = v_0\tau$. Combining the values of v_0 and τ given in 5.1 and 5.2, we obtain:

$$\left(\frac{y_{pack}^2}{y_{pack}^3 + \beta}\right)^{1/2} (y_{pack}^3 + 1)^{2/3} = \frac{\overline{\beta}}{\overline{\alpha}} \frac{d}{R_s} Re_B^{-1/2} \tag{5.3}$$

where y_{pack} is the normalized Buller's drop radius and the pedix $pack$ is to stress that this prediction is valid at maximum packing. $1/\overline{\alpha} = \sqrt{27/(8\alpha)}$ and $Re_B = \nu^2\rho_B/(R_s\gamma)$ is the Reynolds number based on the spore equivalent radius and the capillary velocity. Eq. 5.3 predicts the relation between intergill distance d, nondimensional Buller's drop radius y_{pack} and spore radius R_s when the maximum packing condition is satisfied. Given the values of two of the three parameters among d, y_{pack} and R_s (in our case, d and R_s) eq. 5.3 predicts the third (y_{pack}) under the assumption of maximum packing. Fig.5.1 shows the numerical solution of 5.3 for y_{pack} color-coded from 0 to 5 for

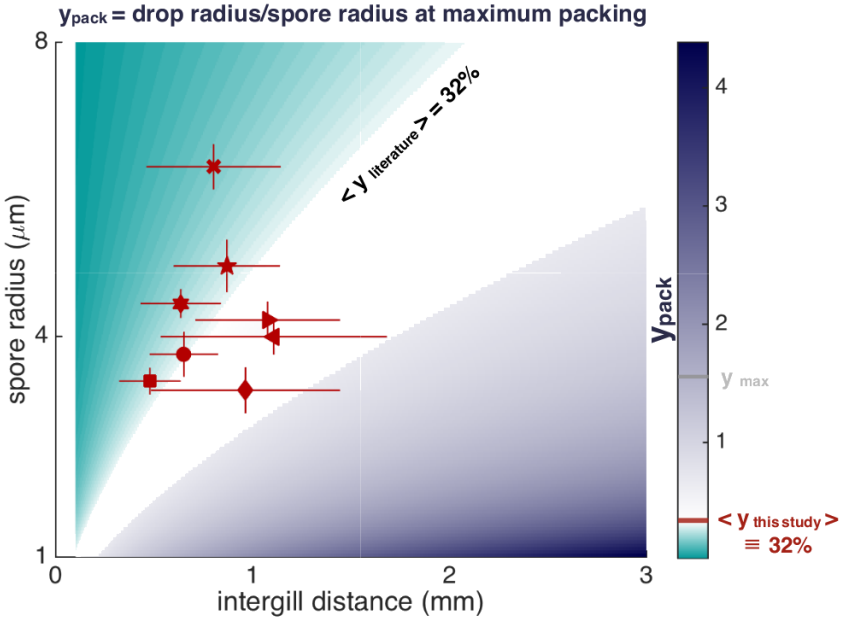

FIGURE 5.1: Prediction for normalized Buller's drop radius at maximum packing, y_{pack} , obtained by numerically solving Equation 5.3. y_{pack} is color coded from 0 (cyan) to 4.4 (black). Symbols correspond to data of intergill distances and spore radii measured from 8 species collected in Michigan and Wisconsin.

different combinations of intergill distances and spore radii. The color represents the value of normalized Buller's drop radius that allows for maximum packing. The experimental data represent the average and standard deviation of spore radius and intergill distances across single individuals. The comparison of the experimental data that I collected in this study with the theoretical prediction of maximum packing shows that real species lie in a region of the phase space where the Buller's drop radius that maximizes spore packing ranges from $R_s = 23$ to $50\%R_s$. Previous data in the literature suggest that Buller's drop radius scales as $R_B \sim 32\%R_s$. An approximate solution of 5.3 valid at small y is outlined in the paper attached at the end of this chapter and demonstrate that this linear scaling of Buller's drop and spore radius implies intergill distance must scale as $R_s^{3/2}$ for an optimally packed mushroom. All data up to date are consistent with the hypothesis of maximum spore packing, suggesting that Buller's drop radius is finely tuned to control range and speed. How this fine tuning works in a process that appears to be extracellular and depending on environmental conditions remains a fascinating question for future research. The results I obtained in this chapter are being submitted for publication to Mycologia.

Chapter 6

Paper: *A precise relationship among Buller's drop, ballistospore and gill morphologies enables maximum packing of spores within gilled mushrooms.*

A precise relationship among Buller's drop, ballistospore and gill morphologies enables maximum packing of spores within gilled mushrooms.

Martina Iapichino[1], Yen Wen Wang[2], Savannah Gentry[2], Anne Pringle[2], Agnese Seminara[1]

June 19, 2019

Keywords: Surface tension catapult | Fungi | Morphometrics | Maximum speed | Biomechanics

Abstract. Basidiomycete fungi eject spores using a surface tension catapult; a fluid drop forms at the base of each spore and after reaching a critical size, coalesces with the spore and launches it from the gill surface. Although basidiomycetes function within ecosystems as both devastating pathogens and mutualists critical to plant growth, an incomplete understanding of ballistospory hinders predictions of spore dispersal and impedes disease forecasting and conservation strategies. Building on a nascent understanding of the physics underpinning the surface tension catapult, we first use the principle of energy conservation to identify ejection velocities resulting from a range of Buller's drop and spore sizes. We next model a spore's trajectory away from a basidium and identify a specific relationship among Buller's drop and spore radii, and intergill distances, enabling maximum packing of spores within a minimal amount of gill tissue. We collected data of spore and gill morphologies from wild mushrooms and compared data to the model. The data of real species suggest that in order to pack the maximum number of spores into the least amount of biomass, Buller's drop should be smaller but comparable to the spore. Previously published data of Buller's drop and spore sizes support our hypothesis pointing and also suggest a linear scaling between spore's and Buller's drop radii. Morphological features of the surface tension catapult appear tightly regulated to enable maximum packing of spores. Moreover, if mushrooms are maximally packed and Buller's drop radii scale linearly with spore radii, we predict that intergill distance should scale as spore radius to the power 3/2.

[1]CNRS and Université Côte d'Azur, Institut de Physique de Nice, UMR7010, Parc Valrose 06108, Nice, France

[2]Departments of Botany and Bacteriology, University of Wisconsin-Madison, Madison, WI, USA

M.I., A.P and A.S. designed research; M.I., Y.W.W., S.G. and A.P. performed experiments; M.I. and A.S. performed theoretical analysis and data analysis; M.I., A.P. and A.S. wrote manuscript.

The authors declare no conflict of interest.

To whom correspondence should be addressed. E-mail: agnese.seminara@unice.fr

Introduction. Molds, yeasts and mushrooms are ubiquitous across Earth. Estimates of the number of fungal species range from 1 to more than 5 million [1] and fungi in ecosystems function as decomposers, mutualists and pathogens. Emerging fungal diseases endanger crops as well as wild plants and animals, threatening food security, but also altering forest dynamics and contributing to the extinction of animals. Losses cost millions of dollars of damage [2, 3, 4].

Fungal bodies are immobile, typically hidden within substrates. Fungi use spores to reproduce and travel away from a natal habitat. Spores are carried in currents more or less far away from a source and when a spore lands in a favorable environment, it germinates and begins or extends the life cycle. Basidiomycetes are among the most common fungi, encompassing pathogens like *Puccinia graminis* (wheat stem rust) and *Phakopsora pachyrhizi* (Asian soybean rust), as well as charismatic mushrooms like *Tricholoma matsutake* (matsutake) and *Amanita muscaria* (the fly agaric). The phylum is defined by the basidiospore. Typically, basidiospores are launched via a surface tension catapult. In species with mushrooms, spores grow in groups of four from basidia arranged along the gills or pores of a mushroom, each spore attached to a sterigma. A drop of liquid, known as Buller's drop, forms extracellularly at the base of each spore when water condenses on the spore's hilar appendix. Buller's drop then collapses onto another adaxial drop formed along the longitudinal axis of the spore itself (see sketch in Figure 1). Upon coalescence, surface energy is converted into kinetic energy and transmitted to the spore which is ejected horizontally away from the basidium and sterigma. The spore decelerates to rest after a few milliseconds and then falls vertically between

two gills or within the pore.

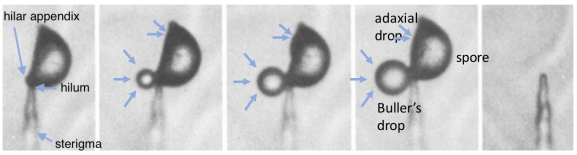

Figure 1: Diagram illustrating our current understanding of the surface tension catapult. First, Buller's drop forms and grows by condensation at the base of the spore. At the same time, the adaxial drop grows in contact with the spore also by condensation. At a critical size, Buller's drop collapses onto the adaxial drop and reduces the total liquid surface, thus releasing energy. The released energy is converted into kinetic energy, catapulting the spore away from its parent. The size of Buller's drop, together with material parameters, determines the speed of spore discharge. Image adapted from [5]. Condensation onto Buller's drop and the adaxial drop is visualized through blue arrows.

Ballistospore discharge is a phenomenon that has fascinated scientists for over a century. It was first observed by Schmitz [6]. In the 20th century, Buller described the phenomenon in more detail, observing the development and discharge of the spore, describing the formation of the drop at the hilar appendix and the subsequent discharge of the spore together with the drop [7]. The drop is now referred to as Buller's drop and the discharge understood as a "surface tension catapult". Progress in understanding of the anatomy and the physics of the surface tension catapult was enabled by the development of cameras. Webster et al. provided photographic evidence of Buller's drop forming at the hilar appendix just before discharge and proposed a two-phase mechanism for spore ejection: the first phase involving Buller's drop enveloping the spore surface, acquiring momentum; the second involving the sharing of momentum and movement of the center of mass of the spore-drop complex, a result of the rapid wetting [5]. Subsequent works modeled the conversion of surface energy into kinetic energy with different degrees of complexity and imaged ballistospore launch with progressively faster cameras [8, 9, 10, 11, 12]. Pringle et al. [8] observed coalescence while Noblin et al. [9] describe the process as encompassing four stages and estimate approximately half of the total surface energy is dissipated during launch. Recently, Liu et al. moved beyond considerations of energy balance to generate simulations of the fluid dynamics within the Buller's drop and the adaxial drop during coalescence, as well as describe experiments with biomimetic drops [12]. Liu et al [12] find that coalescence occurs in a regime where viscous dissipation in the Buller's drop is negligible. Hence energy is not dissipated to set Buller's drop in motion, but presumably to break the spore from the sterigma. In addition, Liu et al. find that pinning of the contact line provides directionality for the spore/drop complex as it ejects away from the originating gill.

It has long been hypothesized that mushrooms form gills to increase the surface area for spore production and pack the maximum number of spores into a minimal investment of biomass [7, 13, 14]. To achieve an optimal morphology, the size of Buller's drop, the size of the spore, and the distance between gills must be finely coordinated. While spore size and intergill distance may be under genetic control [15], Buller's drop forms extracellularly [16]. Whether and how fungi control the size of Buller's drop remains unknown, although data reporting characteristic sizes of Buller's drop for different species suggest individual species do control size [10, 17, 8, 11].

To explore whether the morphologies of gilled mushrooms enable the maximum packing of spores within tissues, we first revisit the theory relating ejection velocity and flight time to the horizontal distance traveled by a spore from the moment of launch to the moment it begins sedimenting out from underneath the gills [7, 8, 9, 10, 11, 12]. Using energy balance we obtain the ejection speed and highlight its dependence on the sizes and densities of the spore and Buller's drop. By combining expressions for ejection speed and flight time we predict the distance travelled ballistically by the spore-drop complex before sedimentation starts. We then use our theory to elucidate the criteria enabling maximum packing of spores. In the phase space made up of the three variables *(i)* drop radius, *(ii)* spore radius and *(iii)* intergill distance, the criterion for maximum packing is that spores must travel ballistically exactly midway between two facing gills. Given two of the three variables *(i)-(iii)*, our theory predicts the third, assuming maximum packing. To compare models to data, we collected mushrooms of eight different species and measured the statistics of spore size and intergill distance. By placing these morphological data on the phase space generated from our theory, we discover that for collected species, the radius of Bullers drop must range between 23% and 50% of the radius of the spore (depending on the precise value of spore density and efficiency of energy conversion). To elucidate the exact relationship between Bullers drop and spore radii, we revisit previously published data for an additional 13 species [10, 17, 8, 11] and find Bullers drop scales as 32% of spore size, consistent with our prediction. In fact these data [10, 17, 8, 11] suggest Bullers drop radius scales linearly with spore radius, and combined with our theory, generate a second prediction: to enable maximum packing, intergill distance should scale as spore radius to the power 3/2. In the aggregate our work synthesizes thinking about the

morphologies of Bullers drop, spores and gills, while providing insights into the principles shaping ballistospory.

Results

Ejection speed. The surface tension catapult reaches a maximum ejection speed when the spore and Buller's drop have nearly the same volume. The two drops that coalesce to power the surface tension catapult are made from condensed water vapor and appear following the secretion of hygroscopic substances by the fungus. When Buller's drop coalesces with the adaxial drop, the resulting reduction of surface area provides the surface energy to accelerate the spore. Because the adaxial drop is pinned to the surface of the spore, Buller's drop accelerates along it towards the distal tip of the spore. But once the moving drop reaches the tip of the spore, capillarity and contact line pinning decelerate water and its momentum is transferred to the spore. Momentum transfer causes the force that breaks the contact between spore and sterigma, resulting in spore ejection away from the basidium. The release of surface energy by coalescence is $\sim \pi\gamma R_B^2$, where γ is surface tension and R_B is Buller's drop radius. By balancing surface energy to kinetic energy of the spore-drop complex, we obtain:

$$v_0 = U\sqrt{\frac{y^2}{y^3+\beta}} \tag{1}$$

where v_0 is the ejection velocity; $U = \sqrt{3\alpha\gamma/(2\rho_B R_s)}$ is a velocity scale independent of Buller's drop radius; R_s is the radius of a sphere with the same volume as the spore, this is the "equivalent radius" of the spore and we will call it "spore radius" for short; $y = R_B/R_s$ is the normalized Buller's drop radius i.e. the ratio of Buller's drop to spore radii; ρ_B and ρ_s are densities of Buller's drop and spore respectively and $\beta = \rho_s/\rho_B$ is the ratio of Buller's drop to spore densities.

We use the parameter α to account for the fraction of available energy dissipated when the spore breaks apart from the hilum, the point of attachment between the spore and the sterigma (see Figure 1). Viscous dissipation during the dynamics of coalescence can be neglected because ballistospory operates in a regime of low Onhesorge number [12]. After exploring the dynamics of ejection velocity, we realized that the simple energy balance discussed at length in the literature and recapitulated in equation (1) predicts there will be a radius of Buller's drop that maximizes v_0 (see Figure 2). By zeroing the derivative in (1) we obtain the size of Buller's drop that maximizes ejection speed: $y_{\max} = (2\beta)^{1/3}$ and when considering spores with densities once to twice the

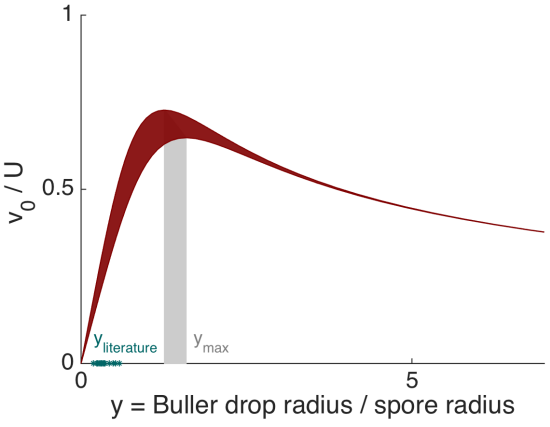

Figure 2: Energy balance from eq (1) predicts discharge speed. We represent the normalized speed v_0/U as a function of y defined as the ratio of Buller's drop radius R_B divided by spore radius R_s (red line). The thickness of the red line represents predicted speed for β ranging from 1 to 2, where β is the ratio of spore to drop density. Velocity peaks at $y_{\max} = (2\beta)^{1/3} = 1.26$ to 1.59 (grey shades) for β ranging from 1 to 2.

density of water[18], $\beta = 1$ to 2, this equation implies that at $y_{\max}$ Buller's drop radius will be comparable to the equivalent radius of the spore $R_B \sim 1.26R_s$ to $1.59R_s$ (the grey shade in Figure 2 marks all values of $y_{\max}$, for β ranging from 1 to 2). Note that at $y_{\max}$ control of the ejection speed is robust, i.e. ejection speed becomes insensitive to small deviations from the exact value of Buller's drop size. Buller's drop is generally assumed to scale with spore length [10] and this scaling appears to hold for at least 13 species of basidiomycetes, as shown in [10, 17, 8, 11]. Supplementary Figure 1 uses these published data to calculate spore radius R_s, pointing to $y_{\text{literature}} = R_B/R_s \sim 0.35 \pm 0.11$ where we report average $\pm$ standard deviation. $y_{\text{literature}}$ are represented in cyan on the horizontal axis in Figure 2, suggesting these fungi do not operate at maximum ejection speed, but rather remain on the rising slope well away from the maximum. Note that only three out of their 13 species are gilled mushrooms (the rest are either pored), but these three species line up with the rest of the data and show no clear departure from the rest of the collected data (Supplementary Figure 1).

Ballistic range. Once the spore-drop complex is ejected, air drag causes rapid deceleration and the complex's relaxation time is well approximated by the Stokes time [19, 20]:

$$\tau = T(y^3+1)^{2/3} \tag{2}$$

where we have considered the complex as a sphere with volume equal to the sum of the spore and drop volumes. In equation (2), $T = 2R_s^2/(9\nu\bar{\beta})$, ν is the air kinematic viscosity and $\bar{\beta}$ is the density of air divided by the density of the spore-drop complex.

After discharge, spores travel horizontally a distance

$$x = v_0\tau$$

with v_0 and τ from equations (1) and (2). Next a spore stops abruptly and starts to sediment vertically, out from beneath a pair of facing gills, following a trajectory commonly known as a "sporabola" (represented in Figure 3A).

Maximum spore packing. In order to successfully escape the mushroom, a spore must travel away from its basidium a distance x into the clear space between gills, before sedimentating; it must travel far enough to avoid entrapment within the basidia and spores underneath it. If x is in fact dictated by this safety criterion, and assuming all gills are reproductive, then the distance between two facing gills, d, should be at least twice x, hence $d > 2x$. To pack as many spores as possible within a mushroom and avoid inefficient empty spaces, the distance between gills must be close to this minimum value:

$$d \sim 2x$$

where $x = v_0\tau$. Plugging in the values of v_0 and τ given by equations (1) and (2) we obtain:

$$\left(\frac{y_{\text{pack}}^2}{y_{\text{pack}}^3+\beta}\right)^{1/2}(y_{\text{pack}}^3+1)^{2/3} = \frac{\bar{\beta}}{\bar{\alpha}}\frac{d}{R_s}Re_B^{-1/2} \qquad (3)$$

where y_{pack} is the normalized Buller's drop radius and we add the suffix $_{\text{pack}}$ to stress that this prediction is valid at maximum packing. Here $1/\bar{\alpha} = \sqrt{27/(8\alpha)}$, and $Re_B = \nu^2\rho_B/(R_s\gamma)$ is a Reynolds number based on spore radius and capillary velocity $\gamma/(\nu\rho_B)$. Equation (3) predicts the relationship between three variables: nondimensional Buller's drop radius y_{pack}, spore radius R_s and intergill distance d - at maximum packing. Hence given two of these three variables, equation (3) predicts the third, assuming maximum packing and given the values of the parameters (spore density, energy conversion efficiency). For example, for any combination of spore radius and intergill distance, equation (3) predicts the optimal radius of Buller's drop that achieves maximum packing. We solve Equation (3) numerically and show the result for y_{pack} in Figure 3 color-coded from 0 (cyan) to 5 (black) for different combinations of intergill distances and spore radii using parameters listed in table 1. At each point in the phase space defined by spore radius and intergill distance, the color represents the value of normalized Buller's drop radius that achieves maximum packing. Symbols and errorbars represent our own data, described, analyzed and discussed below.

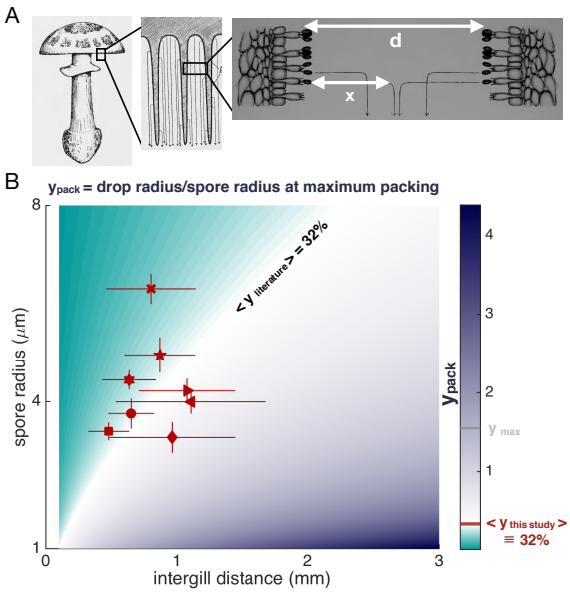

Figure 3: Mushroom cap morphology and the maximum packing of spores. (A) From left to right: Drawing of a mushroom; close-up of gills; magnified view of adjacent gills with basidia and basidiospores. Several trajectories of individual spores (sporabolas) are represented in faint gray in the center panel and black arrows in the right panel; adapted from Buller's drawing [7]. Maximum packing implies that spores initially travel a distance $x = v_0\tau$ to reach the midpoint between two facing gills separated by $d = 2v_0\tau$ with v_0 and τ given by equations (1) and (2). (B) Prediction for normalized Buller's drop radius at maximum packing, y_{pack}, obtained by numerically solving Equation (3) with the parameters listed in Table 1. y_{pack} is color coded from 0 (cyan) to 4.4 (black); white corresponds to the value $\langle y_{\text{literature}}\rangle = 32\%$. Symbols correspond to data of intergill distances and spore radii measured from 8 species collected by us in Michigan and Wisconsin (see Figure 4). The optimal Buller's drop radius for the 8 collected species is $y_{\text{pack}} \sim 0.32 \pm 0.12$, where we report average $\pm$ standard deviation. The free parameters α and ρ_s are chosen within their range of natural variation, to fit the average optimal Buller's drop to data published in the literature. However, the prediction varies little across the range of variation of α and ρ_s.

Data collection. To place real species on the phase space generated by our theory, we collected data of spore and gill morphologies for eight wild mushroom species (see Table 2). We cut mushroom caps free from stipes (stems) (Figure 4A) and placed caps with gills facing

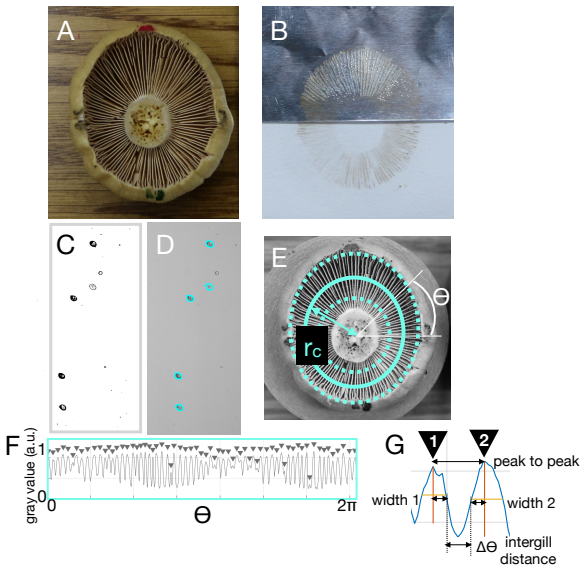

Figure 4: Data collection. (A) An image of the underside of a mushroom cap collected in Fall 2017 from the Huron Mountain Club. (B) Spore print obtained by placing the spore cap on half aluminum foil/ half paper overnight. (C) Confocal microscope image of a sample of spores from the spore print. (D) Segmentation of image, used to recover spore contours. (E) Concentric circles around the center of the cap mark where intergill distances were measured and define the azimuthal angle θ, used to compute intergill distance. (F) Grey scale values from image in E, as a function of azimuthal angle θ. Peaks correspond to gills (white in the image of E), while troughs correspond to the spaces between gills (dark or black in the image of E). To obtain intergill distance, we marked all peaks (note arrows) and kept track of their azimuthal angles. (G) Close-up image showing locations of two peaks, marked by arrows 1 and 2. Intergill distance $\nabla\theta$ is defined in radiants, as the peak to peak distance (difference in azimuthal angle of two adjacent peaks) minus the width of the gills themselves (width 1 and width 2 - see Materials and Methods). We calculated intergill distances in mm by multiplying $\nabla\theta$ for the radius of the circle (r_c in panel E).

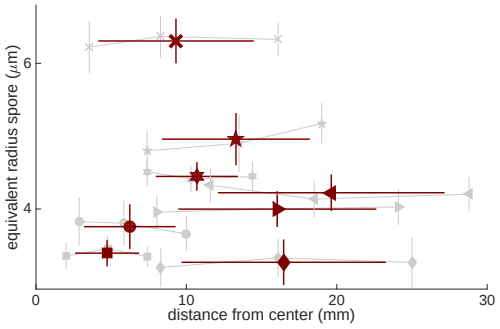

Figure 5: Spore size does not vary across a single mushroom cap. Gray thin lines mark measurements of spore radius taken at three different distances from cap stipes with errorbar representing standard deviation; means and standard deviations for spore radius at all distances are shown in dark red vertical lines. Horizontal red line guides the eye.

down onto aluminum foil and paper overnight, resulting in what is called a spore print (Figure 4B). We then isolated samples of spores from different regions of the spore print: close to the stipe, close to the edge of the cap, and exactly in between the stipe edge and cap edge. Spores were imaged using confocal microscopy (Figure 4C) and images analyzed with standard imaging protocols to trace and measure the contours of spores (Figure 4D). Spore areas S were computed from images of between 155-1180 spores and radii calculated from measures of area $R_s = \sqrt{S/\pi}$. To measure distances between gills, we first identified the center of each cap by eye. We then drew between 6 and 10 circles (depending on the size of each specimen's cap) concentrically around the center of the cap (Figure 4E). Values of grey were measured along each circle (one example in Figure 4F) and the profile of the grey values used to define intergill distances d as the peak to peak distance minus the width of the peaks (see close up of two peaks in Figure 4G, and Materials and Methods).

While spore size varies from species to species, it does not vary across a single mushroom cap (spores are not larger nearer the center or edge of a cap); mushrooms produce spores of a single size within a sporocarp (Figure 5). Moreover, the average intergill distance also remains constant with distance from the center of the cap. The phenomenon is driven by the appearance of secondary gills towards the edge of a mushroom cap; as two gills with origins at the stipe diverge, often a secondary gill will appear. The appearance of secondary and tertiary gills keeps intergill distances constant. The only species in our dataset with variable intergill distances was an as yet unidentified species of *Russula sp.*, which does not grow secondary gills [21, 14]. Among measured species, intergill distances vary from about 0.25 mm to 1.5 mm (Figure 6) but there is no obvious correlation between intergill distances and the size of the mushroom cap.

To ensure maximum packing in real species,

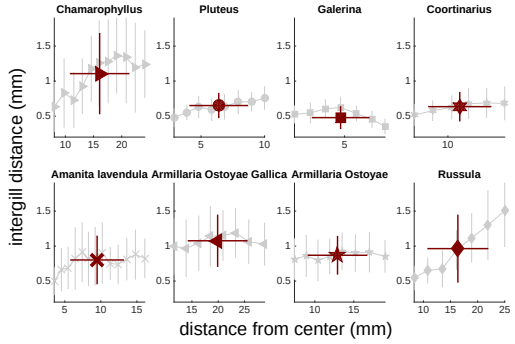

Figure 6: Average gill spacing varies little with distance from cap stipes, a result driven by the appearance of secondary gills at greater distances from the cap stipe. Gray lines show all measures at various distances from the center, vertical red lines show the average and standard deviation. Horizontal red line guides the eye. The only exception is *Russula sp.* which has no secondary gills.

Buller's drop radius should be 23% to 50% of spore radius. Next, we compared experimental data collected in this study with the theory for maximum packing of spores. We computed averaged and standard deviationd of spore radius and intergill distance across single individuals and we placed these data on the phase space generated by our theory for maximum spore packing (symbols and errorbars in Figure 3B).

While most parameters of our theory are known (Table 1), α and ρ_s are not. In order to understand how the model depends on parameters, we derived an approximate formula from our theory (3), showing that in fact the optimal radius of Bullers drop depends only weakly on these free parameters. Indeed, when $y_{\text{pack}} < 1$, one can expand equation (3) to leading order to obtain:

$$R_B \sim d\sqrt{\frac{27\rho_a}{8\alpha\rho_s}\frac{\nu^2\rho_a}{R_s\gamma}} \tag{4}$$

This compact formula shows that Buller's drop radius at maximum packing depends on $(\alpha\rho_s)^{-1/2}$. For the range of variation reported in the literature (see Table 1), $\alpha\rho_s = 0.4\,g/cm^3$ to $1.9\,g/cm^3$, and we predict $\langle y_{\text{this study}}\rangle = 50\%$ to 23%. In Figure 3, we use $\alpha\rho_s = 0.9\,g/cm^3$ resulting from the following fitting procedure: we choose this parameter so that the predicted Buller's drop radius for maximum packing averaged over our collected data $\langle y_{\text{this study}}\rangle$ coincides with the observed value $\langle y_{\text{literature}}\rangle \sim 32\%$ (Figure 3B Supplementary Figure 1) from the cited literature. Importantly, the value of this parameter (obtained e.g. for $\alpha = 0.5$ and $\rho_s = 1.8g/cm^3$) is consistent with the range of variation reported in the literature (see Table 1). With this choice of parameters, the predicted Buller's drop radius at maximum packing for the 8 species analyzed in this study is $y_{\text{this study}} = (32 \pm 12)\%$, where we report average $\pm$ standard deviation.

Buller's drop is often assumed to scale *proportionally* with spore size[10], and published data showed in Supplementary Figure 1 corroborate this assumption, pointing to $R_B \sim 32\% R_s$ (although note that only 3 out of 13 species in these published data correspond to gilled mushrooms). However, the assumption appears at odds with the prediction for maximum packing, since equation (4) implies that Buller's drop radius scales linearly with intergill distance d and with the *inverse* square root of spore radius R_s. To resolve the paradox, intergill distance must increase with increasing spore radius in the following way:

$$d \sim 0.32\sqrt{\frac{8\gamma\alpha\rho_s}{27\rho_a^2\nu^2}R_s^3}$$

where we have simply plugged $R_B \sim 0.32\,R_s$ into equation (4). In order to convincingly prove or disprove this relationship, further data monitoring spore, drop and gill morphologies as well as spore density and ejection velocity are needed.

Conclusions. The intricate morphologies of gilled mushrooms are hypothesized to maximize surface to volume ratios, an adaptation enabling the maximum packing of spores within a minimum investment of biomass. The hypothesis requires intergill distances to be exactly twice the horizontal range of an ejected spore: an ejecting spore must both clear its natal gill and avoid lodging into the gill across from it, and assuming gills are crowded together as closely as possible (to efficiently use the space within a mushroom cap), the spore will be finely tuned to reach midway between facing gills. Intergill distances may be shaped by the reach of a spore, but because spore range is dictated by the dimension of Bullers drop and its density relative to the dimension and density of the spore, the three parameters: intergill distance, spore size, and Bullers drop size - emerge as highly interdependent in the context of maximum packing. We find that intergill distances and spore sizes of real species populate a region of phase space where the radius of Bullers drop enabling maximum spore packing ranges from 23% to 50% of spore radius. Our conclusion is supported by previously published data [10, 17, 8, 11]

suggesting Bullers drop radius scales with spore dimensions as $R_B \approx 32\% R_s$. Moreover, the linear scaling of Bullers drop and spore radii implies intergill distance must scale as $R_s^{3/2}$ within an optimally packed mushroom. More data are needed: our conclusions are based on a total of 21 species. But the data collected to date are consistent with the hypothesis of maximum packing, confirming Bullers drop radius will be finely tuned to control range and speed. How tuning evolves and the biomechanics underpinning ballistospory, in a purely extracellular process operating in the context of fluctuating environments, remains a fascinating question for future research.
[1]

Materials and methods.

Data collection and published data Between the 15th and 17th of September, 2017 we collected mushrooms from lands owned by the Huron Mountain Club, in the Upper Peninsula of Michigan. On the 15th of October, 2017 we collected mushrooms from the University of Wisconsin-Madison Lakeshore Natural Preserve. We collected opportunistically, taking any mushroom that appeared in good shape, but focusing on gilled (not pored) fungi. Unfortunately we were collecting during a particularly dry period, nonetheless, we collected specimens of eight morphologically distinct species, listed in Table 2.
We also identified published data in literature; these data are generated from a different group of species (Supplementary Table 1) and provide measurements of Buller's drops and spores, but do not provide information about intergill distances [10, 17, 8, 11]. In this series of papers, the authors capture ballistospory from high speed video microscopy and obtain Buller's drop and spore size from image analysis.

Preparing specimens for morphometrics On the same day mushrooms were collected, caps were separated from stipes using a scalpel and left face down from 8 to 12 hours on a piece of paper covered with aluminum foil in order to create spore prints. Spore prints are generated when spores fall from gills and settle directly underneath the cap. Spore prints reflect the morphology of each collected specimen and the location of stipes and patterns of gill spacing are easily seen. Spore prints were carefully wrapped in wax paper and taken back to the Pringle laboratory at the University of Wisconsin-Madison. To image spores, three small pieces of aluminum foil, each measuring approximately 1mm x 1mm, were cut (i) from close to each stem,(ii) equidistant between the stem and the cap edge and (iii) from near the edge of each cap. Spores were washed off each foil piece and suspended in a Tween 80 0.01% vol solution. 15 μl of each spore suspension were immediately spread onto a glass slide and spores imaged. Microscope slides were sealed with nail polish in order to avoid evaporation of Tween and prevent the movement of spores during imaging. To measure distances between gills, a photograph of each cap's underside, with a ruler included in the photograph, was taken immediately after spore printing using a Canon EOS400D. After spore printing and photography, collected mushrooms were dried in a mushroom dryer and stored in the Pringle laboratory.

Identification of species using DNA barcoding To generate DNA barcodes for each collected sporocarp, we extract DNA with an NaOH extraction method modified from [24] to amplify the internal transcribed spacer locus [25]. First, the tissues of each sporocarp were ground finely with a pestle in 40μl of 0.5 M NaOH and the solution centrifuged at 13,000 rpm for 10 min. Five microliters of supernatant were transferred to 495μl of 100 mM Tris-HCl (pH 8) and centrifuged at 13,000 rpm for another min. The resulting supernatant was used as template for PCR reactions. To amplify the internal transcribed spacer, 1 μl of extracted DNA was mixed with 1μl of a 10μM solution of the primer ITS1F (5'-CTT GGT CAT TTA GAG GAA GTA A-3'), 1 μl of a 10 μM solution of the primer ITS4 (5'TCC GCT TAT TGA TAT GC-3'), 12.5μl of Lucigen's EconoTaq Plus Green 2x Master Mix, and 9.5μl of nuclease-free water. The reaction mixtures were incubated using a Bio-Rad C1000 Thermal Cycler at 95$^\circ C$ for 5 min, followed by 30 rounds of amplification, including (1) denaturation at 95$^\circ C$ for 30 s, (2) primer annealing at 50$^\circ C$ for 30 s and (3)elongation at 72$^\circ C$ for 60 s. The PCR protocol concluded with 7 min of additional elongation at 72$^\circ C$ and pauses at 4$^\circ C$. Amplified products were cleaned and then Sanger sequenced by Functional Biosciences (Madison, Wisconsin). Sequences are deposited in Genbank (https://www.ncbi.nlm.nih.gov/) with accession numbers MK829236-MK829244.

Microscopy and image analysis to measure spore geometry. Images of spores were taken using microscopes housed at the Newcomb Image Center at the University of Wisconsin-Madison. Spores were imaged either individually or in groups, depending on whether a particular microscope's field of view housed one or more than one spore, using Zeiss Elyra LSM 780 and Zeiss LSM 710 confocal microscopes. Spores were not stained as all collected species proved to be autofluorescent. The laser wavelength used to excite autofluorescence was 405 nm. The average area and average radius of spores of each species were then calculated using an image analysis tool implemented in ImageJ v. 1.51. A single pixel's dimension in μm was calculated from the microscope and the images converted to greyscale (8-bit or 16-bit). ImageJ was then used to threshold each image and convert the greyscale to a binary image, highlighting all the spores to be counted and using the measurement of a single pixel to calculate the area of each spore as shown in Figure 4C-D. Spores touching other spores were not measured, nor were

[1] Webster and coauthors estimated that Buller's drop contain about 1% in mass of mannitol and sucrose [22], hence γ and ρ_B are well approximated by the surface tension[23] and density of water.

Table 1: List of parameters and their estimated or measured values from the literature.

Parameter	**symbol**	**value**	**Reference**	used in Fig 3
air density	ρ_a	$1\,kg/m^3$		$1\,kg/m^3$
spore density	ρ_s	0.8 to $3.8\,g/cm^3$	[18]	$1.8\,g/cm^3$
Buller's drop density	ρ_B	$1\,g/cm^3$	same as water[1]	$1\,g/cm^3$
Buller's drop surface tension	γ	$0.07\,N/m$	same as water[1]	$0.07\,N/m$
efficiency of energy conversion	α	$(50 \pm 5)\%$	[9]	0.5
density ratio	$\beta = \rho_s/\rho_B$			
density ratio	$\bar{\beta} = \rho_a/\rho_B$			
Reynolds number	$Re_B = R_s\gamma/(\nu^2\rho_B)$			
Reynolds number	$Re_s = R_s\gamma/(\nu^2\rho_s)$			
intergill distance	d			
spore radius	R_s			
Buller's drop radius	R_D			
normalized Buller's drop radius	$y = R_B/R_s$			
y at maximum packing	y_{pack}			

Table 2: List of collected species, collection location, number of spores imaged and analyzed, corresponding symbol used in Figures.

Collected species	**Location**	**# spores**	**symbol**
Camarophyllus borealis	Huron Mountain Club	231	▶
Cortinarius caperatus	Huron Mountain Club	1180	✱
Amanita lavendula	Huron Mountain Club	155	×
Armillaria mellea spp. complex (A)	Huron Mountain Club	301	★
Armillaria mellea spp. complex (B)	Huron Mountain Club	257	◀
Mycena sp.	UW-Madison Lakeshore Natural Preserve	530	●
Russula sp.	UW-Madison Lakeshore Natural Preserve	1053	◆
Galerina marginata	UW-Madison Lakeshore Natural Preserve	1159	■

particles smaller than $2\mu m^2$. Particles bigger than $2\mu m^2$ were identified either as spores or not-spores by eye.

Image analysis to measure intergill distances. The distances between gills were measured along cap undersides using concentric circles drawn at various distances from the stipe, or center of the cap. Image analysis used ImageJ v1.51 as well as a custom Matlab R2017b script. We first used ImageJ v1.51 to open each picture, set pixel length in *mm* using the image of the ruler included in each photograph, and convert images to greyscale (8-bit or 16-bit). The Oval Profile plugin was used to obtain greyscale profiles traced along each of the concentric circles drawn onto an image; these circles were drawn manually around the stipe. Profiles were sampled at 3600 equally spaced points along each circle. Next, the area of each circle was measured to calculate its average distance from the cap center, and these measurements were later used to convert the distance between gills from radiants to mm. The greyscale profile obtained from ImageJ was imported into Matlab and analyzed with the function Findpeaks. Peaks in the greyscale image identify the centers of gills, which appear white in greyscale images. Peaks that were closer than 0.3° were discarded as noise. We visually inspected data to confirm that minor peaks did correspond to gills. Finally, we quantified gill thickness as the width of the peak, defined as the distance where grey value drops half way below peak prominence, which is a measure of peak height. The distance between two gills was defined as the distance between their centers minus the half-width of each of the two gills.

Aknowledgements

This work was supported by the Agence Nationale de la Recherche Investissements d'Avenir UCA^{JEDI} #ANR-15-IDEX-01, by the Centre National de la Recherche Scientifique Project international de cooperation scientifique (PICS) "2FORECAST", by the Thomas Jefferson Fund a program of FACE and by the Global Health Institute at the University of Wisconsin-Madison. We would like also to thank Huron Mountain Club for its kind hospitality and Sarah Swanson for all her help and discussions about confocal microscopy.

References

[1] M Blackwell. The fungi: 1,2,3, ... 5.1 million species? *Am Journ Bot*, 98:426–438, 2011.

[2] E Pennisi. 1000 genomes project gives new map of genetic diversity. *SCIENCE*, 29:574–575, 2010.

[3] K. Kupferschmidt. Attack of the clones. *Science*, 337:638, 2012.

[4] M.C. Fisher, D.A. Henk, C.J. Briggs, J.S. Brownstein, L.C. Madoff, S.L. McCraw, and S.J. Gurr. Emerging fungal threats to animal, plant and ecosystem health. *Nature*, 484:186, 2012.

[5] J Webster, RA Davey, and CT. Ingold. Origin of the liquid in Buller drop. *Trans. Br. Mycol. Soc.*, 83:524–527, 1984.

[6] J Schmitz. Beitrage zur anatomie und physiologie des schw amme. *Linnaea*, 17:437, 1843.

[7] A. H. R. Buller. *Researches on Fungi, Vol. II.* Longmans, Green and Co., London, U.K., 1909.

[8] Pringle A, Patek S, Fischer M, Stolze J, and Money N. The captured launch of a ballistospore. *Mycologia*, 97:866–871, 2005.

[9] X Noblin, S Yang, and J Dumais. Surface tension propulsion of fungal spores. *The Journal of Experimental Biology*, 212:2835–2843, 2009.

[10] Mark W. F. FISCHER, Jessica L. STOLZE-RYBCZYNSKI, Yunluan CUI, and Nicholas P. MONEY. How far and how fast can mushroom spores fly? physical limits on ballistospore size and discharge distance in the basidiomycota. *Fungal Biol*, 114:669–675, 2010.

[11] J L Stolze-Rybczynski, Y Cui, M Henry, H Stevens, DJ Davis, MWF Fischer, and NP Money. Adaptation of the Spore Discharge Mechanism in the Basidiomycota. *Plos One*, 4:e4163, 2009.

[12] Fangjie Liu, Roger L. Chavez, S. N. Patek, Anne Pringle, James J. Feng, and Chuan-Hua Chen. Asymmetric drop coalescence launches fungal ballistospores with directionality. *J. R. Soc. Interface*, 14:20170083, 2017.

[13] Karl BMcKnight and Robin O. Roundy. Optimal gill packing in agaric sporocarps. *J Theoret Biol*, 150:497–528, 1991.

[14] Mark W. F. FISCHER and Nicholas P. MONEY. Why mushrooms form gills: efficiency of the lamellate morphology. *Fungal Biol*, 114:57–63, 2010.

[15] U. K ues and Y. Liu. Fruiting body production in basidiomycetes. *Appl Microb Biotech*, 54:141–152, 2000.

[16] J.Webster, R.A.Davey, and J.C.R.Turner. Vapour as the source of water in buller's drop. *Mycolog Res*, 93:297–302, 1989.

[17] Jessica L. Stolze-Rybczynski. *Biomechanics of spore discharge in the basidiomycota*. PhD Thesis, Miami University, Oxford, OH, 2009.

[18] Tareq Hussein, Veera Norros, Jani Hakala, Tuukka Pet aj a, Pasi P. Aalto, Ullar Rannik, Timo Vesala, and Otso Ovaskainen. Species traits and inertial deposition of fungal spores. *J Aeros Sci*, 61:81–98, 2013.

[19] G. G. Stokes. On the effect of internal friction of fluids on the motion of pendulums. *Transactions of the Cambridge Philosophical Society*, 9:8–106, 1851.

[20] Mark W. F. FISCHER, Jessica L. STOLZE-RYBCZYNSKI, Diana J. DAVIS, Yunluan CUI, and Nicholas P. MONEY. Solving the aerodynamics of fungal flight: how air viscosity slows spore motion. *Fungal Biol*, 114:943–948, 2010.

[21] R Phillips. *Mushrooms of North America*. Little, Brown & Company, Boston., 1991.

[22] J Webster, RA Davey, N Smirnoff, W Fricke, P Hinde, D Tomos, and Turner JCR. Mannitol and hexoses are components of Buller's drop. *Mycol. Res.*, 99:833–838, 1995.

[23] M Hoorfar, M.A. Kurz, Z Policova, M.L. Hair, and A.W. Neumann. Do Polysaccharides Such as Dextran and Their Monomers Really Increase the Surface Tension of Water? *Langmuir*, 22:52–56, 2006.

[24] H. Wang, M. Qi, and A. J. Cutler. A simple method of preparing plant samples for PCR.. *Nucleic acids research*, 21:4153, 1993.

[25] C. L. Schoch, K. A. Seifert, S. Huhndorf, V. Robert, and C. A. ...Fungal Barcoding Consortium Spouge, J. L.and Levesque. Nuclear ribosomal internal transcribed spacer (ITS) region as a universal DNA barcode marker for Fungi. *Proceedings of the National Academy of Sciences*, 109:6241–6246, 2012.

Supplementary information for: A precise relationship among Buller's drop, ballistospore and gill morphology enables maximal packing of spores within gilled mushrooms.

Martina Iapichino[1], Yen Wen Wang[2], Savannah Gentry[2], Anne Pringle[2], Agnese Seminara[1]

June 16, 2019

1 Data from literature

In Table 1 we list published data for 14 species obtained from high speed video microscopy, as well as the reference. We discarded from the selected literature the species for which measures of Buller's drop size was inferred indirectly. When spore volume V_s is available, the equivalent radius of the spore (called "spore radius" in the main text for short), i.e. the radius of a sphere with the same volume as the spore is calculated as $R_s = (3V_s/4\pi)^{1/3}$. When spore volume is not available directly, we calculate it from spore length and width, assuming it is a prolate spheroid, $V_s = \frac{4}{3}\pi L_s W_s^2$. In Figure 1 we show the linear scaling between spore radius and Buller's drop radius from data published in the literature.

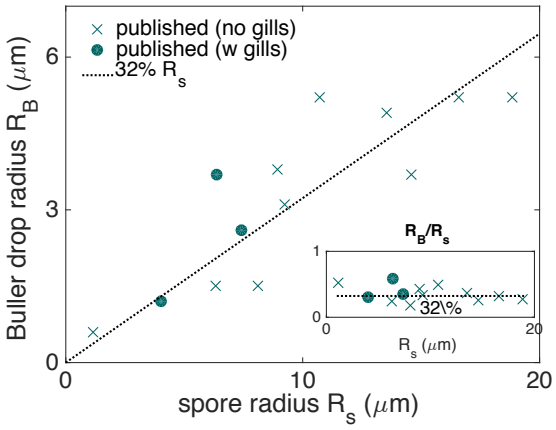

Figure 1: Linear scaling between spore radius and Buller's drop radius from data published in the literature, and recapitulated in table 1. Spore radius is calculated as described in the main text.

2 Spore density

In Figure 2 we show the histogram of spore densities from several different species from ref [1]; spore densities range from 0.8 to 3.8 g/cm^3.

3 Efficiency of energy conversion

To set the range of variation of the efficiency parameter α, we use measures of ejection velocity for two species of basidyomycetes (*Auricolaria* and *Sporobolomyces*), for

[1]CNRS and Université Côte d'Azur, Institut de Physique de Nice, UMR7010, Parc Valrose 06108, Nice, France
[2]Departments of Botany and Bacteriology, University of Wisconsin-Madison, Madison, WI, USA
The authors declare no conflict of interest.
To whom correspondence should be addressed. E-mail: agnese.seminara@unice.fr

Table 1: Name of species and type, Buller's drop radius R_B, spore length L_s, spore width W_s, spore volume V_s, spore equivalent radius R_s, reference. Species with gilled mushrooms are marked in boldface.

Name of species	**Structure bearing spores**	R_B (μm)	L_s (μm)	W_s (μm)	V_s (μm)	R_s (μm)	**ref**
Trametes versicolor (Poriales)	Pores	0.6	-	-	6.4	1.15	[4]
Aleurodiscus oakesii (Agaricomycetes, Russulales)	Spines	5.2	23.2	17.0	-	18.86	[5]
Itersonilia perplexans (Temellomycetes, Tremellales)	Yeast	4.9	15.1	12.8	-	13.52	[5]
Tilletiopsis albescens (Exobasidiomycetes, incertae sedis)	Yeast	3.7	13.4	4.4	-	6.38	[5]
Laccaria amethystina (Agaricomycetes, Russulales)	**Gills**	**1.5**	**8.1**	**8.1**	**-**	**8.1**	**chap 4 [3]**
Stereum hirsutum (Agaricomycetes, Russulales)	Pores	1.2	7.2	3.0	-	4.02	chap 4 [3]
Xerula radicata (Agaricomycetes, Russulales)	**Gills**	**3.7**	**16.8**	**13.6**	**-**	**14.59**	**chap 4 [3]**
Gymnosporangium juniperi- virginianae (Pucciniomycetes,Pucciniales)	Gelatinous telial horns	5.2	20.0	15.1	-	16.58	[6]
Tilletia caries (Exobasidiomycetes, Tilletiales)	Host tissue	5.2	21.4	7.6	-	10.73	[6]
Sporobolomyces salmonicolor (Pucciniomycetes, Sporidiobolales)	Yeast	3.8	11.5	7.9	-	8.95	[6]
Auricularia auricula (Agaricomycetes, Auriculariales)	Jelly-like basidiome	3.1	12.9	7.8	-	9.22	[6]
Polyporus squamosus (Agaricomycetes, Polyporales)	Pores	2.6	14.0	5.4	-	7.41	[6]
Armillaria tabescens (Agaricomycetes, Agaricales)	**Gills**	**1.5**	**6.8**	**6.1**	**-**	**6.32**	**[6]**
Clavicorona pyxidata (Agaricomycetes, Russulales)	Yeast	1.2	4.7	3.5	-	3.86	[6]

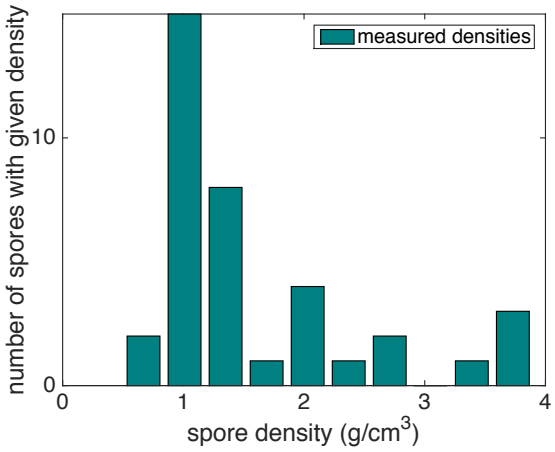

Figure 2: Histogram of spore densities from ref [1].

which geometry of the spore and drop was observed directly. For these two species, the observed velocity is 0.73% and 0.68% of the theoretical maximum respectively (see Table 2, ref [2]), yielding a fraction of usable energy $0.73^2 = 0.53$ and $0.68^2 = 0.46$, which we summarize as $(50 \pm 5)\%$. These measures are consistent with estimates presented in ref [3], based on different hypothesis about the geometry of the adaxial drop.

References

[1] Tareq Hussein, Veera Norros, Jani Hakala, Tuukka Pet aj a, Pasi P. Aalto, Ullar Rannik, Timo Vesala, and Otso Ovaskainen. Species traits and inertial deposition of fungal spores. *J Aeros Sci*, 61:81–98, 2013.

[2] X Noblin, S Yang, and J Dumais. Surface tension propulsion of fungal spores. *The Journal of Experimental Biology*, 212:2835–2843, 2009.

[3] Jessica L. Stolze-Rybczynski. *Biomechanics of spore discharge in the basidiomycota*. PhD Thesis, Miami University, Oxford, OH, 2009.

[4] Mark W. F. FISCHER, Jessica L. STOLZE-RYBCZYNSKI, Yunluan CUI, and Nicholas P. MONEY. How far and how fast can mushroom

spores fly? physical limits on ballistospore size and discharge distance in the basidiomycota. *Fungal Biol*, 114:669–675, 2010.

[5] Pringle A, Patek S, Fischer M, Stolze J, and Money N. The captured launch of a ballistospore. *Mycologia*, 97:866–871, 2005.

[6] J L Stolze-Rybczynski, Y Cui, M Henry, H Stevens, DJ Davis, MWF Fischer, and NP Money. Adaptation of the Spore Discharge Mechanism in the Basidiomycota. *Plos One*, 4:e4163, 2009.

Part III

Annexes to part I

Appendix A

Set-up development

In this chapter I will talk about the procedures we use and the trials we made to build the final setup I used for my results.

A.1 Microfluidic system to generate a surface gradient

When I started my PhD, the first prototype we used was a microfluidic mixer with two inlets and eight outlets connected to eight different channels drilled at the base of a chamber of internal dimensions ($4cm \times 4cm$). The channels where separated from the agar by a membrane. The two inlets had two solutions, one with no PEG, one with 30% vol/vol concentration of PEG. With the microfluidic mixer it was possible to get at the outlets eight different PEG concentrations going linearly from 0% to 30% vol/vol. sketch

When I started my PhD, the idea was to use soft lithography to fabricate a microfluidic gradient generator made in poly(dimethylsiloxane) (PDMS) similar to the one described in [63] and showed in 2.3.1. In our case we used a modified design with respect to the one proposed: the system is always symmetric, but our network of microchannels has two inlets and eight outlets. The working principle is straight forward. At the beginning there are N vertical and parallel inlets. At each step, each channel follows a vertical serpentine path and then divides in two, horizontally. The new horizontal internal channels connect between them in a node and a new vertical channel branches out from the node (see Fig. A.1). Then a new step repeats. If N is the number of inlets, i is the index of the branching step, at each step $N + i$ channels will be formed. Horizontal channels are short compared to the vertical ones. In each vertical serpentine channel, two fluids flowing laminarly get mixed by diffusion. To guarantee mixing only by diffusion, the time the two fluid spend flowing laminarly side by side needs to be long enough to reach equilibrium, which is the

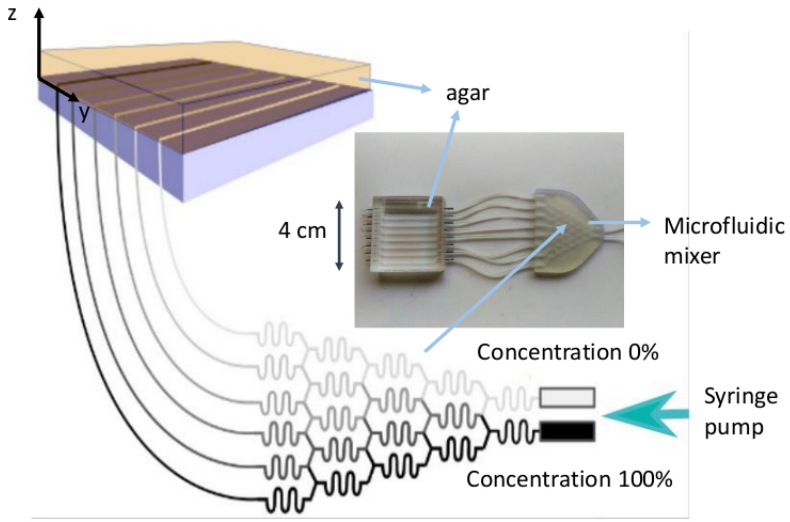

FIGURE A.1: Sketch of the microfluic mixer connected to a setup. Solutions go from 0% concentration (light grey) to 100% concentration (black)

reason why vertical channels have a serpentine shape. As a general rule then, flow speed shouldn't exeed the lenght of the serpentine portion per second. For more accurate calculations, time to reach equilibrium can be calculated solving diffusion equation in one dimension in a finite media. The initial set-up configuration for the experiment contemplated the use of a syringe pump to infuse two solutions with 0% and 5% concentration of Polyethylene glycol (PEG) into the two inlets of the microfluidic mixer. The microfluidic mixer had eight outlets connected to eight channels carved in the base of a squared chamber of 4 cm$\times$4cm. The agar and the channels were separated by a membrane that was glued at the base of the chamber, above the channels.

This configuration was abandoned for several reasons, that I will list in the following subsection.

A.1.1 Difficulties

Syringe pump. The main issues with the syringe pump are that (i) it is not possible to use bigger volumes than 50 ml, (ii) it is possible to control the flow rate at which the syringe pump is operating, but it is not possible to control the pressure exerted by the flow during infusion. Our experiments need ~500 ml of solutions to be infused continuously during 2 or 3 days. Changing the syringe during the experiment exposes to the risk of external contamination and to the entrapment of air bubbles inside the syringe. These air bubbles are

then infused in the microfluidic mixer and get stuck inside it, stopping the experiment and making it unusable. About pressure, it can happen that pieces of agar or other clusters of salts get stuck in a channel, increasing resistance in the channel itself. In such a case, the syringe pump continues infusing at a constant rate and pressure in the channel will raise. The fluid then tries to flow through the path where it meets less resistance and, in the worst case, detaches the membrane between the channel and the agar, crashing the whole experiment. I tried to substitute the two syringes with two bottles and to infuse the solutions with the help of a pressure pump that infuses at very low pressures (100-500 mbar), but the detachment of the membrane was still a problem. The other issue was that with this configuration the flow rate changed with time, as the pressure pump pushes over the surface of the solutions inside the bottles, and consequently the pressure exerted by the liquid column changes with time. We solved the issues due to pressure control using Mariotte's bottles.

Flux imbalance due to different viscosities. I tried to use the pressure pump to inject solutions of 20% PEG 10kDa in water or 20% PEG 20KDa in water in the microfluidic setup. The different viscosities created an imbalance in the microfluidic setup. In Fig. A.2 you can see the time required to infuse 500 μl of solution and the corresponding flow rates at different inlet pressures as a function of the different channels. Using this configuration I realized there was another problem: the big molecules of PEG 10 kDa and PEG 20 kDa tend to sediment in the bottom part of the bottles, hence not only the flow rate changes with time due to the change of the liquid column inside the bottles, but also thanks to a density gradient that develops inside the solutions. It is not possible to constantly mix the solution in the bottles due to the development of air bubbles. We solved the issue using PEG with a much lower molecular weight and removing the microfluidic mixer.

Concentration of PEG used during experiments			
PEG 10 kDa		**PEG 20 kDa**	
# Bottle	**% w/w**	**# Bottle**	**% w/w**
1	0	**1**	0
2	20	**2**	20

Bubbles. For everyone working with microfluidics, one of the main problems is the presence of bubbles in the microfluidic circuit, as they adhere to

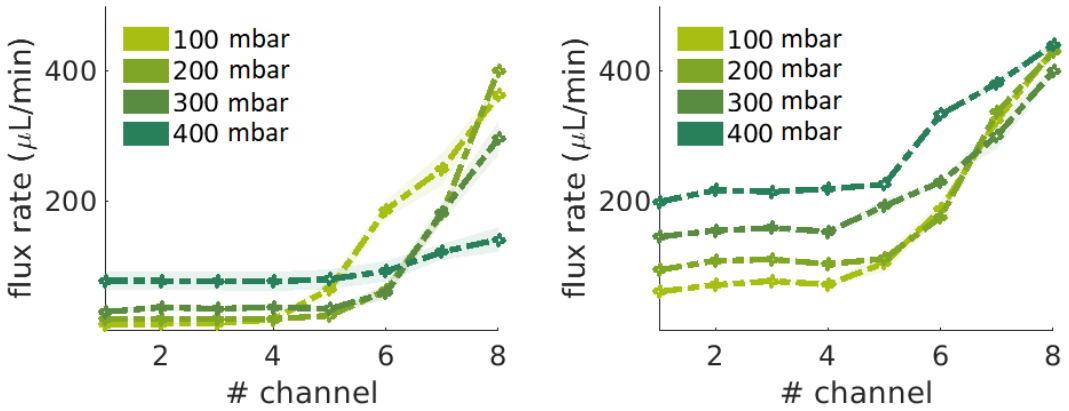

(A) Flux rate measured for PEG 20 kDa 20 % w/w.

(B) Flux rate measured for PEG 10 kDa 20 % w/w.

FIGURE A.2: Flux rates for different inlet pressures.

the channels surface and clog them. To avoid the presence of bubbles we tried to degas the solutions with the help of a sonicator, but this system does not eliminate 100 % of the bubbles. Moreover, gas trapped inside the solutions can expand its volume with time, creating new bubbles. The hardest point was when bubbles got stuck inside the microfluidic mixer, as this completely crashed the experiment. I tried to avoid the bubbles using bubble traps as well, but bubble traps needed to be changed after one day due to accumulation of salts in the filter. Disconnecting the bubble traps lets air inside the microfluidic mixer, thus not helping the success of the experiment. We solved the issues of bubbles removing the microfluidic mixer and scaling the agar chamber to bigger dimensions.

Small setup. At first, to collect images, I was using the $4cm \times 4cm$ with the surface of the agar facing up. The volume of agar used was very small and it dried very fast in the Plexiglas chamber at 30 °C, crashing the experiment. I solved this problem with the fabrication of a cover. The membrane separating the channels from the agar needed to be glued and changed at each new experiment. Gluing the membrane was very complicated and required to remove the glue manually at each new experiment, with the help of an optical microscope to observe the surface while scraping away the glue. Moreover glue could spread by capillarity inside the channels at the moment of gluing, making the membrane useless and clogging the channel. We solved the issues changing completely the design of the setup, making it bigger and carving the channels directly into the agar, thus removing the necessity of the membrane.

A.2 Deposition of bacteria on a stripe

During my PhD I tried to develop a protocol to deposit bacteria solution as a stripe instead of a single drop. The goal was to deposit bacteria on a stripe to then reduce the complexity of the equations to solve from 3D to 2D. I used microscope slides of 76 mm $\times$ 26 mm dimensions, where I wrapped the 26 mm in sterile tape and autoclaved everything (see Fig. A.3. Once the microscope slides were sterile, I immerged the side wrapped with tape in 10 μl of bacteria solution and waited for it to absorb the solution, then I was gently leaning the taped side on the surface of the MSgg agar in the Petri dish. Fig. A.4 shows one example of biofilm growing after using this deposition technique. The growing biofilm expands symmetrically maintains proportions, expanding only in one direction, meaning that only the distance of the lateral edges from the center matters. The main problem with this technique is the difficulty to control the exact volume that is deposited on the agar surface. It probably can be perfectioned, but I could not work further on this for absence of time.

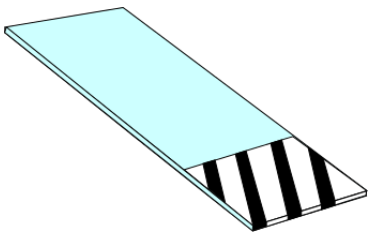

FIGURE A.3: Sketch of a microscope slide with a piece of sterile tape attached at one of the extremities.

A.3 Measure of osmotic pressure with dialysis membranes

At first, we did not have an available osmometer in the laboratory, so we tried to develop a DIY laboratory technique to quantify the variation of osmotic pressure inside the agar. The idea was to use the chamber of a syringe with a dialysis membrane glued ad the base and the top hole closed with parafilm, containing a solution with a certain osmotic pressure. The volume of the solution was then supposed to vary depending on the osmotic pressure of the agar the syringe was in contact with. Dialysis membranes are generally sold in a tubular form. To check if this idea could work I tested the dialysis membrane

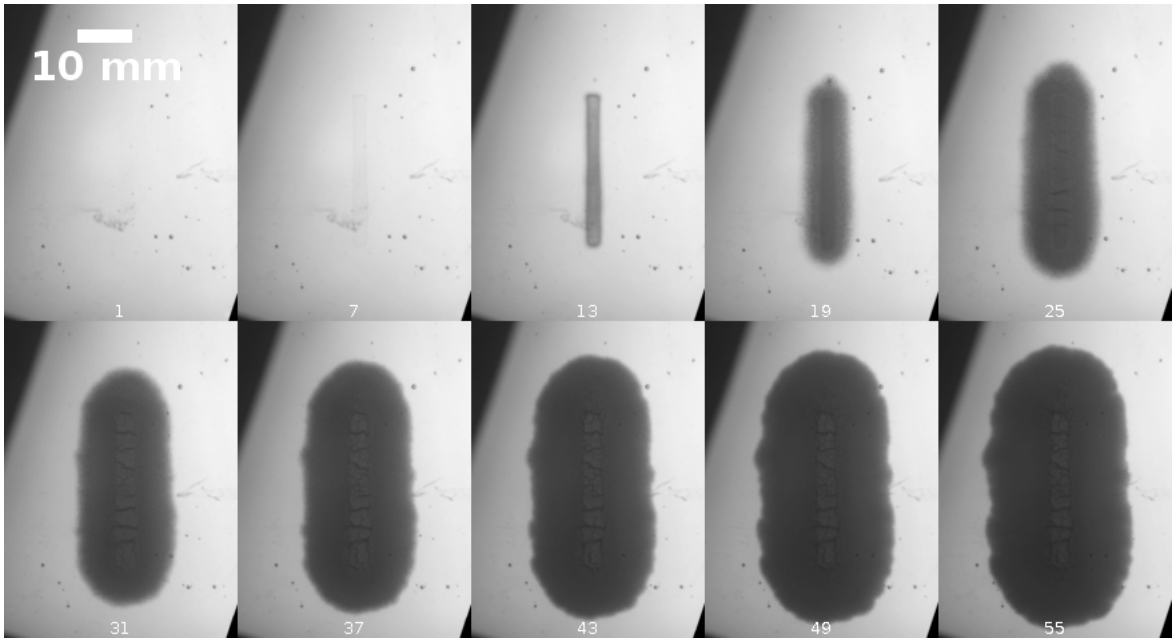

FIGURE A.4: Example of biofilm growing using the stripe deposition technique.

filling them with 20 % w/w PEG 20 kDa and 5 % w/w PEG 20 kDa and submerging them in a solution of 10 % w/w PEG 20 kDa, following [35]. Fig. A.5 shows how the relative weight of the membranes I used changed with time. Purple represents 5 % w/w PEG 20 kDa and green represents 20 % w/w PEG 20 kDa, shades represent standard deviation. This result shows that dialysis membranes work for our purpose. I tried later to implement the system with the syringes, but almost none of them worked (data not shown) and the preparation was really time consuming. In the end we acquired an osmometer and the development of this system became unnecessary.

A.4 Osmotic gradients in Petri dishes

I got inspired by [126] and [57] to try to create a linear osmolarity gradient directly in a Petri dish. They use what they call a "gradient-plate technique" which consists in pouring two layers of agar, one with the desired compound whose gradient is to be developed, and the other without. The first layer is poured maintaining the petri dish tilted and left to dry. Once dried, the dishes is put in a flat position and the same amount of the second component is poured, to get a total of 25 ml of medium. From my observation, this technique is very useful to get preliminary results, as it is very easy to realize, but

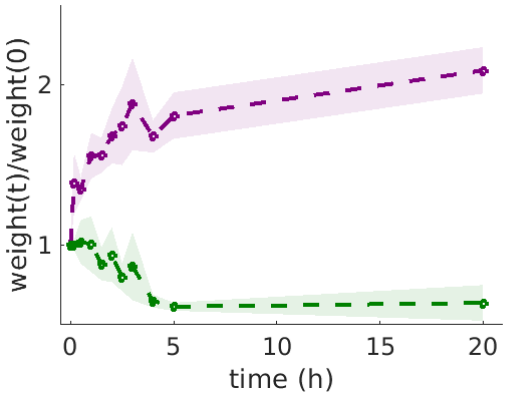

FIGURE A.5: Change of relative weight of the two solutions contained inside dyalisis membranes

the surface of the Petri dishes gets often irregular during the preparation and it does not offer much choice over the desired shape of the gradient. The slope of the gradient in the Petri dishes is less steep than the one developed with the linear gradient in the final set-up and most of the biofilms show an irregular shape without an appreciable displacement of the center of mass. That is why in the end we decided to do my experiments with a more developed setup that offers a better control over the shape of the gradient and the surface of agar. Fig. A.6 shows the contours of a biofilm grown in a Petri dish (left), the development of the radius of the contours ρ as a function of the angle θ and the development of the radius normalized with respect to the area ρ^* as a function of the angle θ. The methods used to analyze these data are the same described in chapter 2.

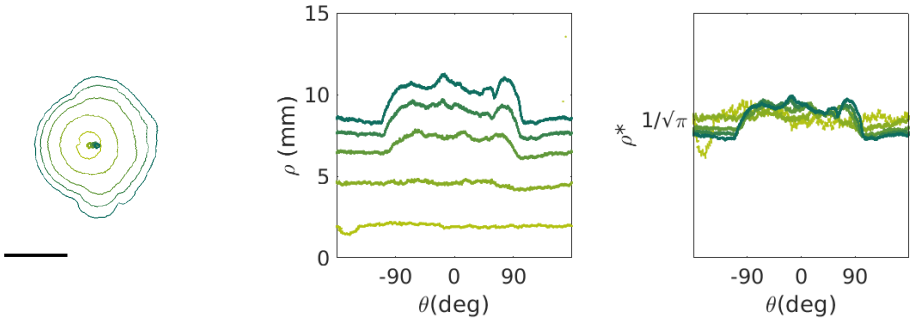

FIGURE A.6: Experiment in Petri dishes with linear gradient going from 0% to 5% PEG 200 Da.

A.5 List of experiments

List of experiments		
Date	**Type of experiment**	**Comments**
10/12/2015	round colonies in Petri dishes	first experiment, training, trial
10/02/2016	round colonies in Petri dishes	training, trial
17/02/2016	round colonies in Petri dishes	training, trial
24/02/2016	stripe colonies in Petri dishes	
11/03/2016	small setups in Petri dishes	no flux
16/02/2017	round colonies in Petri dishes	strange biofilms
23/02/2017	round colonies in Petri dishes	strange biofilms
02/03/2017	round colonies in Petri dishes	round biofilms
10/03/2017	round colonies in Petri dishes	strange biofilm
17/03/2017	round colonies in Petri dishes	round biofilm again
23/03/2017	stripe colonies in Petri dishes	
12/04/2017	fluorescein gradient test	irregular gradient
28/04/2017	fluorescein gradient test	
16/05/2017	stripe colonies in Petri dishes	no parafilm
20/05/2017	fluorescein gradient test	nothing shown. New big squared setup or small?
23/05/2017	stripe colonies in Petri dishes	2 msgg, 2 filtered msgg
08/06/2017	round colonies in Petri dishes	2 msgg, 2 filtered msgg
16/06/2017	round colonies in Petri dishes	no parafilm
23/06/2017	round colonies in Petri dishes	
29/06/2017	round colonies in Petri dishes	
06/07/2017	small setup	failed: all flooded
10/07/2017	fluorescein gradient test	big squared setup, nothing shown
12/07/2017	small setup	failed: membrane, bubbles
13/07/2017	round colonies in Petri dishes	
21/07/2017	round colonies in Petri dishes	
24/07/2017	viscometer tests, diffractometer tests	
26/07/2017	experiment with 2 small setups face up	failed: agar dried
28/07/2017	round colonies in Petri dishes	

04/08/2017	round colonies in Petri dishes	no parafilm, face up, anticondense
09/08/2017	flux time measurement with fluigent	
10/08/2017	flux time measurement with fluigent	
31/08/2017	flux time measurement with fluigent	
04/12/2017	6 normal Msgg w parafilm 6 normal Msgg wo parafilm, 2 filtered Msgg w parafilm, 2 filtered wo parafilm	
06/12/2017	6 normal Msgg w parafilm, 6 normal Msgg wo parafilm, 2 filtered Msgg w parafilm, 2 filtered wo parafilm	
02/02/2018	prepared experiment	bottles crashed in autoclave
15/02/2018	experiment with old setups + stoppers + bacteria	failed: flooded, only 2/4 setups working
23/02/2018	experiment with new setups	linear gradient, failed: flooded
11/04/2018	experiment with new setups	linear gradient failed: bubbles, problems with water-tightness
17/04/2018	experiment with new setups	linear gradient, bacteria. failed: contamination
27/04/2018	experiment with new setups	test with fluoresceine: linear gradient
03/05/2018	experiment with new setups	test with fluoresceine: linear gradient; failed: it shows nothing
08/05/2018	experiment with new setups	test with fluoresceine: linear gradient; no fluoresceine gradient, but osmolarity gradient
17/05/2018	experiment with new setups	linear gradient, bacteria. failed: contamination
03/06/2018	experiment with new setups	test linear gradient, no bacteria
07/06/2018	2 Msgg w PEG 5%, 2 Msgg w PEG 2.5%, 1 normal Msgg	

13/06/2018	experiment with new setups	NO gradient, Failed: contaminations, BUT we have osmolarity values
22/06/2018	experiment with new setups	NO gradient, no flux. Failed: contaminations
05/07/2018	experiment with new setups	autoclaved setup, NO gradient, no flux. No contamination
10/07/2018	experiment with new setups	test EtOH + UV lights on setup, NO gradient, no flux. No contamination. + trial small box
26/07/2018	experiment with new setups	only one setup, linear gradient with bacteria. Failed: you see nothing, biofilms are irregular
02/08/2018	experiment with new setups	linear gradient with bacteria. Failed: contaminations
08/08/2018	experiment with new setups	test linear gradient, no bacteria
08/08/2018	round colonies in Petri dishes	tried new technique for gradient in agar plates. only one worked very well
10/08/2018	experiment with new setups	test linear gradient, no bacteria
31/08/2018	experiment with new setups	test step gradient, no bacteria
04/09/2018	experiment with new setups	test spiked gradient, no bacteria
21/09/2018	experiment with final setups	no gradient, no PEG
02/10/2018	experiment with final setups	no gradient, no PEG. Failed: Biofilms are oval!
09/10/2018	experiment with final setups	no gradient, no PEG
17/10/2018	experiment with final setups	no gradient, PEG 5%. Failed channels detached, setup1 has oval biofilms
26/10/2018	experiment with final setups	step gradient. Failed: contaminations
23/11/2018	experiment with final setups	Failed: impossible to launch experiment
07/12/2018	round colonies in Petri dishes	stock check
11/12/2018	experiment with final setups	step gradient, with bacteria

18/12/2018	experiment with final setups	step gradient, with bacteria. Failed: setup 1 gone, osmometer broken
22/01/2019	experiment with final setups	step gradient, with bacteria
30/01/2019	experiment with final setups	step gradient, with bacteria

Appendix B

Detailed protocol

Day 0:

- Clean bottles from residues of solutions with surfanios; leave bottles one hour with surfanios inside, then rinse with distilled water;
  - I add surfanion to the MSgg solution and leave the mixture in the bottles for at least 1 hour. Then I rinse and rub the bottle with a with a bottle cleaning brush, if necessary.
- clean tubes and connectors with EtOH 70% + distilled water;
  - first I put the dirty tubes and connectors in water and surfanios and leave them for one hour. Then I rinse them. I use a 25 mL syringe to inject all the tubes and connectors with EtOH, then inject all the tubes and connectors with distilled water to rinse away the EtOh.
- wrap bottles and other pieces of equipment in aluminum foil an take them to the autoclave service.
  - I wrap only the top part of the bottles and put a piece of autoclavable tape to fix the aluminum. I put the tubes and the connectors in a beaker that and I cover the top of the beaker with aluminum foil. The autoclave service is at 3rd floor of Institut Biologie Valrose.

Day1:

- prepare missing solutions for MSgg preparation (if needed).

Day 2:

- take back bottles from autoclave service;
- sterilize set-up and metal sticks:

1. clean it with surfanios and distilled water and leave it for one hour in this solution;
   - if necessary, I use also a cleaning brush. I put a special care in cleaning the dispensing needles to remove eventual pieces of gel stuck in it.
2. rinse with EtOH and let it dry under the hood;
   - I usually collect the EtOh in a shallow plastic container while I rinse the setup and its stopper, then I pour the set-up with its stopper in the same EtOH (in the same container I also put the metal sticks to carve the channels in the agar) and let them rest inside the EtOH for some minutes. I insert the metal sticks in the dispensing needles and I rinse again everything in the EtOH. Finally I take the setup with the metal sticks still inserted in the dispensing needles and the cover out of the EtOh and let the EtOH dry.
3. sterilize under hood with UV lights for 30 minutes.
   - I let the EtOH drip and dry from the set-up and its cover before leaving them in the hood

- sterilize set-up plastic box (this is a box where I store the set-up when I take it from IBV to INPHYNI. I use it just to protect the setup):
  1. rinse with EtOH and let the EtOH drip and dry;
  2. sterilize under hood with UV lights for 30 minutes.
- prepare MSsg + 1.5% agar or variants (i.e. with PEG):
  1. autoclave water + agar 1.5%.;
  2. prepare solutions with other components of MSgg, MSgg + PEG 2.5% and MSgg + PEG 5% and leave it at room temperature;
  3. make autoclaved water + agar 1.5% cool down in hot bath @ 60 °C.
- prepare Petri dishes and set-up with its cover;
  - I mix the autoclaved mixture of water and agar 1.5% with the other components of the MSgg. Then I pour the MSgg with agar in the setups and in the Petri dishes. I then preparethe Petri dishes with Msgg + agar + PEG 2.5% and MSgg + agar + PEG 5%.
- leave setups and Petri dishes under hood for 24h face up;

- after 18h00: take bacteria out of -80 °C freezer, streak them on Petri dishes with TYE medium and put them in incubator @ 30 °C, then wait up to the moment where colonies start to be visible (or not more than 14 hours) before taking them out of the incubator.
  - -80 °C freezer of the Arkowitz team is at -2nd floor of IBV. Bacteria are usually stocked in a box labeled "Agnese Seminara". Petri dishes with TYE are prepared by technicians at IBV and they are usually available in the cold room at third floor of IBV. Incubator @ 30 °C is in the P2 room of Arkowitz team.

Day 3:

- before 10h00: take bacteria out of incubator @ 30 °C and put them in a test tube with 5 mL of liquid TYE in shaking incubator @37 °C, then wait from 4 to 6 hours at maximum before measuring OD_{600};
  - Liquid TYE is available in Arkowitz team lab and is prepared by technicians at IBV. Shaking incubator @ 37 °C is in the P2 room of Arkowitz team.
- prepare solutions for Mariotte's bottles:
  - use Msgg recipe without agar, removing the required volume of water when solution needs to be mixed with PEG 200 Da;
  - add from 0 to 5% PEG 200 Da to solutions, depending on needs;
  - filter sterilize with Stericup filters;
  - pour filtered solutions in autoclaved bottles using a flame next to you.
- after 4h measure TYE + cells solution OD_{600} and take it to 1;
  - the spectrophotometer to measure OD_{600} is available in in the P2 room of Arkowitz team. I use 1000 μL of TYE solution as reference, then I measure OD_{600} using 900 μL of bacteria solution mixed with 100 μL TYE solution. Then I prepare 500 μL of bacteria solution with $OD_{600} \sim 1$.
- remove metal sticks from setup;
- plate bacteria solution into set-up and control Petri dishes, wait for it to dry;

- wrap setup and Petri dishes in parafilm and put them in the sterile plastic box prepared the day before;
- take everything to InPhyNi;
  - the bottles and the plastic boxes are heavy and impractical to take around all together. I usually store them in a big container to carry them around.
- set-up the experiment:
  - connect all components with each other;
    1. I connect tube 1 (the one that goes from the Mariotte's bottles to the first setup) to the outlet of the Mariotte's bottles, standing next to the flame;
    2. I put Mariotte's bottle on the standing base next to the plexiglass chamber, I put setup 1 inside the plexiglass chamber;
    3. using a sterile syringe, I aspire the liquid from the Mariotte's bottle in the tube 1 in order to let the air fill the inlet tube of the Mariotte's bottle and the liquid fill the tube 1;
    4. once liquid is dripping spontaneously from tube 1, I connect the tube 1 to the inlet of setup 1, then I wait for the liquid to fill the channel of setup 1
    5. once liquid has filled the channel of the setup 1, I connect tube 2 (the one going from setup 1 to setup 2) to the outlet of setup 1 and wait for the liquid to fill tube 2
    6. once liquid has filled tube 2, I connect tube 2 to the inlet of setup 2, then I wait for the liquid to fill the channel of setup 2
    7. once liquid has filled channel of setup 2, I connect tube 3 (the one going from setup 2 to waste) to the outlet of setup 2, then I wait for the liquid to fill the tube 3
  - rinse every now and then gloves with EtOH;
  - make flow start.

day 4-5:

- check the experiment, remove bubbles.
  - If there are bubbles stuck somewhere, I usually use a 1 mL sterile syringe to gently aspire liquid from the tube 3 of the channel where

the bubble is stuck. This is usually enough to make the flow start again

day 6 = day 0

- take osmotic preassure measurements;
- start again protocol of day 0.

B.1 Msgg broth recipe (1 liter) [8]

Amount/L	**Stock**	Sterilization
50 ml	0.1M Pot. phosphate buffer	filter sterilize or autoclave
100 ml	1M MOPS, pH 7	filter sterilize
10 ml	5 mM $FeCl_3$	autoclave
10 ml	200 mM $MgCl_2$	filter sterilize or autoclave
5 ml	10 mM $MnCl_2$	filter sterilize or autoclave
100 μl	10 mM $ZnCl_2$	autoclave
1 ml	2 mM thiamine	filter sterilize or autoclave
5 ml	Tryptophan (10 mg/ml)	filter sterilize
5 ml	Phenylalanine (10 mg/ml)	filter sterilize
5 ml	Threonine (10 mg/ml)	filter sterilize
25 ml	20% glycerol	filter sterilize
25 ml	20% glutamate	filter sterilize
700 μl	1 M $CaCl_2$	autoclave
758.2 ml	dH_2O (sterile)	

For solid plates, autoclave water with 1.5% agar and let cool to $\sim$ 55 °C. Mix the remaining ingredients, already sterile and add to the autoclaved agar before pouring plates.

Bibliography

[1] Angelini et al. "Bacillus subtilis spreads by surfing on waves of surfactant." In: *Proceedings of the National Academy of Sciences of the United States of America* 106.43 (2009), pp. 18109–13.

[2] Asally et al. "Localized cell death focuses mechanical forces during 3D patterning in a biofilm". In: *Proceedings of the National Academy of Sciences* 109.46 (2012), pp. 18891–18896.

[3] Barnhart and Chapman. "Curli biogenesis and function". In: *Annual Review Microbiology* 60 (2006), pp. 131–147.

[4] Be'er et al. "Paenibacillus dendritiformis Bacterial Colony Growth Depends on Surfactant but Not on Bacterial Motion". In: *Journal of Bacteriology* 191.18 (2009), pp. 5758–5764.

[5] Berbee and Taylor. *Systematics and Evolution. The Mycota (A Comprehensive Treatise on Fungi as Experimental Systems for Basic and Applied Research), vol 7B.* Ed. by McLaughlin, McLaughlin, and Lemke. Springer, Berlin, Heidelberg, 2001.

[6] Branda et al. "A major protein component of the Bacillus subtilis biofilm matrix". In: *Molecular Microbiology* 59.4 (2006), pp. 1229–1238.

[7] Branda et al. "Biofilms: The matrix revisited". In: *Trends in Microbiology* 13.1 (2005), pp. 20–26.

[8] Branda et al. "Fruiting body formation by Bacillus subtilis". In: *Proceeding of the National Academy of Science* 98.20 (Sept. 2001), pp. 11621–11626.

[9] Branda et al. "Genes involved in formation of structured multicellular communities by Bacillus subtilis". In: *Journal of Bacteriology* 186.12 (2004), pp. 3970–3979.

[10] Braudo. "Mechanism of galactan gelation". In: *Food Hydrocolloids* 6.1 (1992), pp. 25–43.

[11] Brenner, You, and Arnold. "Engineering microbial consortia: A new frontier in synthetic biology". In: *Trends in Biotechnology* 26.9 (2008), pp. 483–489.

[12] Brigham et al. "Microscopic imaging of network strands in agar, carrageenan, locust bean gum and kappa carrageenan/locust bean gum gels". In: *Food Hydrocolloids* 8.3 (1994), pp. 331–344.

[13] Bryers. "Medical Biofilms". In: *Biotechnology and Bioengineering* 100.1 (May 2008), pp. 1–18.

[14] Buller. *Researches on Fungi, vol. 2*. London: Longmans Green & Co., 1922.

[15] Carpentier and Cerf. "Biofilms and their consequences , with particular reference to hygiene in food industry". In: *Journal of Applied Bacteriology* 75.1971 (1993), pp. 499–511.

[16] Chapman et al. "Role of Escherichia coli curli operons in directing amyloid fiber formation". In: *Science* 295.5556 (Feb. 2002), pp. 851–855.

[17] Christensen et al. "[2] Molecular tools for study of biofilm physiology". In: *Biofilms*. Vol. 310. Methods in Enzymology. Academic Press, 1999, pp. 20–42.

[18] Chui, Phillips, and McCarthy. "Measurement of the Porous Microstructure of Hydrogels by Nuclear Magnetic Resonance". In: *Journal of Colloid and Interface Science* 174.2 (1995), pp. 336–344.

[19] Cogan and Keener. "The role of the biofilm matrix in structural development". In: *Mathematical Medicine and Biology* 21.2 (2004), pp. 147–166.

[20] Cooper, Dean, and Hinshelwood. "Factors affecting the growth of bacterial colonies on agar plates." In: *Proceedings - Royal Society. Biological sciences* 171.23 (1968), pp. 175–199.

[21] Costerton, Geesey, and Cheng. "How Bacteria Stick". In: *Scientific American* 238(1) (Jan. 1978), pp. 86–95.

[22] D'Argenio et al. "Autolysis and autoaggregation in Pseudomonas aeruginosa colony morphology mutants." In: *Journal of Bacteriology* 184.23 (Dec. 2002), pp. 6481–6489.

[23] Davison and Goldspink. "The effect of training on the swimming muscles of the goldfish (Carassius auratus)". In: *Journal of Experimental Biology* 74.1 (1978), pp. 115–122.

[24] Defez et al. "Additional direct medical costs of nosocomial infections: an estimation from a cohort of patients in a French university hospital". In: *Journal of Hospital Infection* 68.2 (Feb. 2008), pp. 130–136.

[25] Derda et al. "Paper-supported 3D cell culture for tissue-based bioassays." In: *Proceeding of the National Academy of Science USA* 106.44 (Nov. 2009), pp. 18457–18462.

[26] Dertinger et al. "Generation of gradients having complex shapes using microfluidic networks". In: *Analytical Chemistry* 73.6 (2001), pp. 1240–1246.

[27] Diggle et al. "The galactophilic lectin, LecA, contributes to biofilm development in Pseudomonas aeruginosa." In: *Environmental Microbiology* 8.6 (June 2006), pp. 1095–1104.

[28] Dilanji, Teplitski, and Hagen. "Entropy-driven motility of *Sinorhizobium meliloti* on a semi-solid surface". In: *Proceedings of the Royal Society B: Biological Sciences* 281.1784 (2014), p. 20132575.

[29] Divoux, Mao, and Snabre. "Syneresis and delayed detachment in agar plates". In: *Soft Matter* 11 (18 2015), pp. 3677–3685.

[30] Dix and Webster. *Fungal ecology*. London: Chapman & Hall, 1995.

[31] Donlan and Costerton. "Biofilms: Survival Mechanisms of Clinically Relevant Microorganisms". In: *Clinical Microbiology Reviews* 15.2 (Apr. 2002), pp. 167–193.

[32] Enos-Berlage et al. "Genetic determinants of biofilm development of opaque and translucent Vibrio parahaemolyticus". In: *Molecular Microbiology* 55.4 (2005), pp. 1160–1182.

[33] Fauvart et al. "Surface tension gradient control of bacterial swarming in colonies of Pseudomonas aeruginosa". In: *Soft Matter* 8 (Jan. 2012).

[34] Fedtke, Gotz, and Peschel. "Bacterial evasion of innate host defenses - the *Staphylococcus aureus* lesson". In: *International Journal of Medical Microbiology* 294.2–3 (2004), pp. 189–194.

[35] Feher and Ford. "A simple student laboratory on osmotic flow, osmotic pressure, and the reflection coefficient." In: *Advances in Physiology Education* 13.1 (1995), S10–S20.

[36] Fischer and Money. "Why mushrooms form gills: efficiency of the lamellate morphology". In: *Fungal Biology* 114.1 (2010), pp. 57–63.

[37] Fischer et al. "How far and how fast can mushroom spores fly? Physical limits on ballistospore size and discharge distance in the Basidiomycota". In: *Fungal Biology* 114.8 (2010), pp. 669–675.

[38] Fischer et al. “Solving the aerodynamics of fungal flight: How air viscosity slows spore motion”. In: *Fungal Biology* 114 (Sept. 2010), pp. 943–948.

[39] Fisher et al. “Emerging fungal threats to animal, plant and ecosystem health.” In: *Nature* 484 (Apr. 2012), pp. 186–194.

[40] Friedman and Kolter. “Genes involved in matrix formation in Pseudomonas aeruginosa PA14 biofilms.” In: *Molecular Microbiology* 51.3 (Dec. 2004), pp. 675–690.

[41] Friedman and Kolter. “Two Genetic Loci Produce Distinct Carbohydrate-Rich Structural Components of the Pseudomonas aeruginosa Biofilm Matrix”. In: *Journal of Bacteriology* 186.14 (July 2004), pp. 4457–4465.

[42] Fritz et al. “A natural O-ring optimizes the dispersal of fungal spores”. In: *Journal of the Royal Society Interface* 10.85 (2013).

[43] de Gennes. *Scaling concepts in polymer physics*. Cornell Univerrsity Press, 1979.

[44] Golan and Pringle. “Long-Distance Dispersal of Fungi”. In: *Microbiology spectrum* 5 (4 2017).

[45] Gonzalez-Pastor, Hobbs, and Losick. “Cannibalism by sporulating bacteria”. In: *Science* 301 (2003), pp. 510–513.

[46] Götz. “*Staphylococcus* and biofilms”. In: *Molecular Microbiology* 43.6 (Apr. 2002), pp. 1367–1378.

[47] Grossman. “Genetic networks controlling the initiation of sporulation and the development of genetic competence in Bacillus subtilis.” In: *Annual Review of Genetics* 29 (1995), pp. 477–508.

[48] Guvener and McCarter. “Multiple regulators control capsular polysaccharide production in *Vibrio parahaemolyticus*.” In: *Jornal of Bacteriology* 185.18 (Sept. 2003), pp. 5431–5441.

[49] Hall-Stoodley, Costerton, and Stoodley. “Bacterial biofilms: From the natural environment to infectious diseases”. In: *Nature Reviews Microbiology* 2.2 (2004), pp. 95–108.

[50] Hall-Stoodley and Stoodley. “Developmental regulation of microbial biofilms”. In: *Current Opinion in Biotechnology* 13.3 (2002), pp. 228–233.

[51] Harshey. “Bacterial Motility on a Surface: Many Ways to a Common Goal”. In: *Annual Review of Microbiology* 57.1 (2003), pp. 249–273.

[52] Harshey. "Bees aren't the only ones: swarming in Gram-negative bacteria". In: *Molecular Microbiology* 13.3 (1994), pp. 389–394.

[53] J Henrichsen. "Bacterial surface translocation: a survey and a classification." In: *Bacteriological reviews* 36.4 (1972), pp. 478–503.

[54] Henriques et al. "Control of cell shape and elongation by the rodA gene in Bacillus subtilis". In: *Molecular Microbiology* 28.2 (1998), pp. 235–247.

[55] Hohne, Younger, and Solomon. "Flexible microfluidic device for mechanical property characterization of soft viscoelastic solids such as bacterial biofilms." In: *Langmuir* 25.13 (July 2009), pp. 7743–51.

[56] Houari et al. "Rheology of biofilms formed at the surface of NF membranes in a drinking water production unit". In: *Biofouling* 24.4 (2008), pp. 235–240.

[57] Hunt and Sandham. "Improved agar gradient-plate technique." In: *Applied microbiology* 17.2 (1969), pp. 329–30.

[58] Hyde et al. "The ranking of fungi: a tribute to David L. Hawksworth on his 70th birthday". In: *Fungal Diversity* 84 (1 2017), pp. 1–23.

[59] Ingold. *Fungal Spores. Their Liberation and Dispersal.* Oxford: Clarendon Press, 1971.

[60] Irimia, Geba, and Toner. "Universal microfluidic gradient generator". In: *Analytical Chemistry* 78.10 (2006), pp. 3472–3477.

[61] Jackson et al. "Identification of psl, a locus encoding a potential exopolysaccharide that is essential for Pseudomonas aeruginosa PAO1 biofilm formation." In: *Journal of Bacteriology* 186.14 (July 2004), pp. 4466–4475.

[62] Janmey, Winer, and Weisel. "Fibrin gels and their clinical and bioengineering applications". In: *Journal of Royal Society Interface* 6.30 (Jan. 2009), pp. 1–10.

[63] Jeon et al. "Generation of solution and surface gradients using microfluidic systems". In: *Langmuir* 16.22 (2000), pp. 8311–8316.

[64] Jones, Carballido-López, and Errington. "Control of Cell Shape in Bacteria: Helical, Actin-like Filaments in Bacillus subtilis". In: *Cell* 104.6 (2001), pp. 913–922.

[65] Kadouri, Venzon, and O'Toole. "Vulnerability of Pathogenic Biofilms to *Micavibrio aeruginosavorus*". In: *Applied and Environmental Microbiology* 73.2 (2007), pp. 605–614.

[66] Kavamura and de Melo. "Effects of different osmolarities on bacterial biofilm formation". In: *Brazilian Journal of Microbiology* 45.2 (2014), pp. 627–631.

[67] Kinsinger, Shirk, and Fall. "Rapid Surface Motility in Bacillus subtilis Is Dependent on Extracellular Surfactin and Potassium Ion". In: *Journal of Bacteriology* 185.18 (2003), pp. 5627–5631.

[68] Kinsinger et al. "Genetic Requirements for Potassium Ion-Dependent Colony Spreading in Bacillus subtilis". In: *Journal of Bacteriology* 187.24 (2005), pp. 8462–8469.

[69] Marián Kireš. "Mariotte Bottle with Side Openings". In: *The physics teacher* 44 (2006), pp. 388–389.

[70] Klapper et al. "A viscoelastic fluid description of bacterial biofilm material properties". In: *Biotechnology and Bioengineering* 80 (3 2002), pp. 289–296.

[71] Klausen et al. "Biofilm formation by Pseudomonas aeruginosa wild type, flagella and type IV pili mutants." In: *Molecular Microbiology* 48.6 (June 2003), pp. 1511–1524.

[72] Kolter and Greenberg. "The superficial life of microbes". In: *Nature* 441 (2006), pp. 300–302.

[73] Korstgens et al. "Uniaxial compression measurement device for investigation of the mechanical stability of biofilms." In: *Journal of Microbiological Methods* 46.1 (July 2001), pp. 9–17.

[74] Küe and Liu. "Fruiting body production in basidiomycetes". In: *Applied Microbiology and Biotechnology* 54.2 (Aug. 2000), pp. 141–152.

[75] Kupferschmidt. "Attack of the Clones". In: *Science* 337.6095 (2012), pp. 636–638.

[76] Lacey. "Spore dispersal — its role in ecology and disease: the British contribution to fungal aerobiology". In: *Mycological Research* 100.6 (1996), pp. 641–660.

[77] Lasa. "Towards the identification of the common features of bacterial biofilm development." In: *International Microbiology* 9.1 (2006), pp. 21–28.

[78] Latasa et al. "BapA, a large secreted protein required for biofilm formation and host colonization of Salmonella enterica serovar Enteritidis." In: *Molecular Microbiology* 58.5 (Dec. 2005), pp. 1322–1339.

[79] Lau et al. "Absolute Quantitation of Bacterial Biofilm Adhesion and Viscoelasticity by Microbead Force Spectroscopy". In: *Biophysical Journal* 96.7 (2009), pp. 2935–2948.

[80] Leid et al. "The exopolysaccharide alginate protects *Pseudomonas aeruginosa* biofilm bacteria from IFN-gamma-mediated macrophage killing". In: *Journal of Immunology* 175.11 (2005), pp. 7512–7518.

[81] Lemon, Higgins, and Kolter. "Flagella-mediated motility is critical for Listeria monocytogenes biofilm formation." In: *Journal of Bacteriology* 189.12 (June 2007), pp. 4418–4424.

[82] Lemon et al. "Biofilm development with an emphasis on Bacillus subtilis". In: *Current Topics in Microbiology and Immunology* 322 (2008), pp. 1–16.

[83] Lewis. "Persister cells, dormancy and infectious disease". In: *Nature Reviews Microbiology* 5.1 (2007), pp. 48–56.

[84] Linnaeus. *Systema naturae, sive regna tria naturae systematice proposita per classes, ordines, genera and species.* Leiden: Haak, 1735.

[85] Liu et al. "Asymmetric drop coalescence launches fungal ballistospores with directionality". In: *Journal of The Royal Society Interface* 14.132 (2017), p. 20170083.

[86] Lopez, Vlamakis, and Kolter. "Biofilms". In: *Cold Spring Harb Perspect Biol* 2 (2010), pp. 1–11.

[87] Lopez et al. "Cannibalism Enhances Biofilm Development in Bacillus subtilis." In: *Molecular Microbiology* 74 (2008), pp. 609–618.

[88] Lowe. "Distinctive Image Features from Scale-Invariant Keypoints". In: *International Journal of Computer Vision* 60.2 (Nov. 2004), pp. 91–110.

[89] Mah and O'Toole. "Mechanisms of biofilm resistance to antimicrobial agents". In: *Trends in Microbiology* 9.1 (2001), pp. 34–39.

[90] Maira-Litrán et al. "Immunochemical properties of the staphylococcal poly-N-acetylglucosamine surface polysaccharide." In: *FEMS Microbiology Letters* 70.8 (Aug. 2002), pp. 4433–4440.

[91] Mao et al. "Heat-induced aging of agar solutions: Impact on the structural and mechanical properties of agar gels". In: *Food Hydrocolloids* 64 (2017), pp. 59–69.

[92] Mason and Weitz. "Optical Measurements of Frequency-Dependent Linear Viscoelastic Moduli of Complex Fluids". In: *Physical Reviev Letters* 74 (7 Feb. 1995), pp. 1250–1253.

[93] Matsuhashi. *Food gels*. Ed. by Harris. Elsevier Applied Food Science Series. Springer, Dordrecht, 1990. Chap. Agar.

[94] Matsukawa and Greenberg. "Putative exopolysaccharide synthesis genes influence Pseudomonas aeruginosa biofilm development." In: *Journal of Bacteriology* 186.14 (July 2004), pp. 4449–4456.

[95] John S. Mattick. "Type IV Pili and Twitching Motility". In: *Annual Review of Microbiology* 56.1 (2002), pp. 289–314.

[96] McCarthy. "Mariotte's bottle." In: *Science* 80.2065 (1934), p. 100.

[97] McKnight and Roundy. "Optimal gill packing in agaric sporocarps". In: *Journal of Theoretical Biology* 150.4 (1991), pp. 497–528.

[98] Molle et al. "The Spo0A regulon of Bacillus subtilis". In: *Molecular Microbiology* 50.5 (2003), pp. 1683–701.

[99] Money. "More g's than the Space Shuttle: ballistospore discharge". In: *Mycologia* 90.4 (1998), pp. 547–558.

[100] Money. "Osmotic Pressure of Aqueous Polyethylene Glycols: Relationship between Molecular Weight and Vapor Pressure Deficit". In: *Plant Physiology* 91.2 (1989), pp. 766–769.

[101] Morikawa. "Beneficial biofilm formation by industrial bacteria Bacillus subtilis and related species". In: *Journal of Bioscience and Bioengineering* 101.1 (2006), pp. 1–8.

[102] Nijenhuis. *Thermoreversible networks: Viscoelastic properties and structure of gels*. Berlin: Springer-Verlag., 1997. Chap. 11.

[103] Noblin, Yang, and Dumais. "Surface tension propulsion of fungal spores". In: *Journal of Experimental Biology* 212.17 (2009), pp. 2835–2843.

[104] Normand et al. "New Insight into Agarose Gel Mechanical Properties". In: *Biomacromolecules* 1.4 (2000), pp. 730–738.

[105] O'Gara. "ica and beyond: biofilm mechanisms and regulation in Staphylococcus epidermidis and Staphylococcus aureus." In: *FEMS Microbiology Letters* 270.2 (May 2007), pp. 179–188.

[106] O'Toole and Kolter. "Initiation of biofilm formation in Pseudomonas fluorescens WCS365 proceeds via multiple, convergent signalling pathways: a genetic analysis". In: *Molecular Microbiology* 28.3 (1998), pp. 449–461.

[107] O'Toole and Kolter. "Flagellar and twitching motility are necessary for Pseudomonas aeruginosa biofilm development." In: *Molecular Microbiology* 30.2 (Oct. 1998), pp. 295–304.

[108] Oates, Lucas, and Lee. "How brittle are gels?" In: *Carbohydrate Polymers* 20.3 (1993), pp. 189–194.

[109] Pennisi. "1000 Genomes Project Gives New Map of Genetic Diversity". In: *Science* 330.6004 (2010), pp. 574–575.

[110] Pernodet, Maaloum, and Tinland. "Pore size of agarose gels by atomic force microscopy". In: *Electrophoresis* 18.1 (1997), pp. 55–58.

[111] Persat et al. "The mechanical world of bacteria". In: *Cell* 161.5 (2015), pp. 988–997.

[112] Peterson et al. "Viscoelasticity of biofilms and their recalcitrance to mechanical and chemical challenges". In: *FEMS Microbiology Reviews* 39 (2 2015), pp. 234–245.

[113] Piggot and Hilbert. "Sporulation of Bacillus subtilis." In: *Current Opinions in Microbiology* 7.6 (Dec. 2004), pp. 579–586.

[114] Pratt and Kolter. "Genetic analysis of Escherichia coli biofilm formation: roles of flagella, motility, chemotaxis and type I pili." In: *Molecular Microbiology* 30.2 (Oct. 1998), pp. 285–293.

[115] Prince et al. "Lipid-II Independent Antimicrobial Mechanism of Nisin Depends On Its Crowding And Degree Of Oligomerization". In: *Scientific Reports* 6.37908(2016) (Feb. 2017).

[116] Pringle et al. "The captured launch of a ballistospore". In: *Mycologia* 97.4 (2005), pp. 866–871.

[117] Purcell. "Life at low Reynolds number". In: *American Journal of Physics* 45.1 (1977), pp. 3–11.

[118] Purevdorj, Costerton, and Stoodley. "Influence of hydrodynamics and cell signaling on the structure and behavior of Pseudomonas aeruginosa biofilms." In: *Applied Environmental Microbiology* 68.9 (Sept. 2002), pp. 4457–4464.

[119] Rahbani et al. "Characterization of internal structure of hydrated agar and gelatin matrices by cryo-SEM". In: *Electrophoresis* 34.3 (2013), pp. 405–408.

[120] Ramzi, Rochas, and Guenet. "Structure-Properties Relation for Agarose Thermoreversible Gels in Binary Solvents". In: *Macromolecules* 31.18 (1998), pp. 6106–6111.

[121] Rani et al. "Spatial Patterns of DNA Replication, Protein Synthesis, and Oxygen Concentration within Bacterial Biofilms Reveal Diverse Physiological States". In: *Journal of Bacteriology* 189.11 (2007), pp. 4223–4233.

[122] Rani et al. "Spatial patterns of DNA replication, protein synthesis, and oxygen concentration within bacterial biofilms reveal diverse physiological states." In: *Journal of Bacteriology* 189.11 (2007), pp. 4223–4233.

[123] Rogers, van der Walle, and Waigh. "Microrheology of Bacterial Biofilms In Vitro: Staphylococcus aureus and Pseudomonas aeruginosa". In: *Langmuir* 24.23 (2008), pp. 13549–13555.

[124] Rubinstein et al. "Osmotic pressure can regulate matrix gene expression in Bacillus subtilis". In: *Molecular Microbiology* 86.2 (2012), pp. 426–436.

[125] Rusconi et al. "Laminar flow around corners triggers the formation of biofilm streamers". In: *Journal of the Royal Society Interface* 7 (2010), pp. 1293–1299.

[126] Sacks. "A pH gradient agar plate." In: *Nature* 178.4527 (1956), pp. 269–270.

[127] Schmitz. "Beiträge zur Anatomie und Physiologie der Schwamme. I-IV". In: *Linnaea* 17 (1843).

[128] Scriven and Sternling. "On cellular convection driven by surface-tension gradients: effects of mean surface tension and surface viscosity". In: *Journal of Fluid Mechanics* 19.3 (1964), pp. 321–340.

[129] Seminara et al. "Osmotic spreading of Bacillus subtilis biofilms driven by an extracellular matrix". In: *Proceedings of the National Academy of Sciences* 109.4 (Jan. 2012), pp. 1116–1121.

[130] Shemesh and Chai. "A Combination of Glycerol and Manganese Promotes Biofilm Formation in Bacillus subtilis via Histidine Kinase KinD Signaling". In: *Journal of Bacteriology* 195.12 (2013), pp. 2747–2754.

[131] Singh et al. "Quorum-sensing signals indicate that cystic fibrosis lungs are infected with bacterial biofilms". In: *Nature* 407 (2000), pp. 762–764.

[132] Skeel and Berzins. "A Method for the Spatial Discretization of Parabolic Equations in One Space Variable". In: *SIAM Journal on Scientific and Statistical Computing* 11.1 (1990), pp. 1–32.

[133] Sonenshein, Hoch, and Losick. *Bacillus subtilis and its closest relatives: from genes to cells.* Ed. by Bayston et al. ASM Press; Washington DC, 2002.

[134] Spoering and Gilmore. "Quorum sensing and DNA release in bacterial biofilms". In: *Current Opinion in Microbiology* 9.2 (2006), pp. 133–137.

[135] Spormann. "Physiology of microbes in biofilms". In: *Romeo T. (eds) Bacterial Biofilms. Current Topics in Microbiology and Immunology* 322 (2008), pp. 17–36.

[136] Stanley and Lazazzera. "Defining the genetic differences between wild and domestic strains of Bacillus subtilis that affect poly-gamma-dl-glutamic acid production and biofilm formation". In: *Molecular Microbiology* 57.4 (Aug. 2005), pp. 1143–1158.

[137] Stanley and Lazazzera. "Environmental signals and regulatory pathways that influence biofilm formation". In: *Molecular Microbiology* 52.4 (2004), pp. 917–924.

[138] Stephenson and Stephenson. "Bioaugmentation for enhancing biological wastewater treatment". In: *Biotechnology Advances* 10.4 (1992), pp. 549–559.

[139] Stewart and Franklin. "Physiological heterogeneity in biofilms". In: *Nature Reviews Microbiology* 6 (2008), pp. 199–210.

[140] Stolze-Rybczynski et al. "Adaptation of the spore discharge mechanism in the Basidiomycota". In: *PLoS ONE* 4.1 (2009), pp. 1–6.

[141] Stoodley et al. "Biofilm material properties as related to shear-induced deformation and detachment phenomena." In: *Journal of Industrial Microbiology and Biotechnology* 29.6 (Dec. 2002), pp. 361–367.

[142] Stoodley et al. *Biofilms: The Good, the Bad, and the Ugly*. Ed. by Bayston et al. BioLine, Cardiff, UK, 1999, pp. 323–330.

[143] Stoodley et al. "Structural deformation of bacterial biofilms caused by short-term fluctuations in fluid shear: An in situ investigation of biofilm rheology". In: *Biotechnology and Bioengineering* 65.1 (1999), pp. 83–92.

[144] Storm et al. "Nonlinear elasticity in biological gels". In: *Nature* 435 (2005), pp. 191–194.

[145] Sun et al. "Motor-driven intracellular transport powers bacterial gliding motility". In: *Proceedings of the National Academy of Sciences* 108.18 (2011), pp. 7559–7564.

[146] Tako and Nakamura. "Gelation mechanism of agarose". In: *Carbohydrate Research* 180.2 (1988), pp. 277–284.

[147] Tanaka. "Kinetics of phase transition in polymer gels". In: *Physica A: Statistical Mechanics and its Applications* 140.1 (1986), pp. 261–268.

[148] Tanaka. "Viscoelastic model of phase separation". In: *Physical Review E* 56 (4 Oct. 1997), pp. 4451–4462.

[149] Tielker et al. "Pseudomonas aeruginosa lectin LecB is located in the outer membrane and is involved in biofilm formation." In: *Microbiology* 151 (May 2005), pp. 1313–1323.

[150] Towler et al. "Viscoelastic properties of a mixed culture biofilm from rheometer creep analysis." In: *Biofouling* 19.5 (Oct. 2003), pp. 279–285.

[151] Trejo et al. "Elasticity and wrinkled morphology of Bacillus subtilis pellicles". In: *Proceedings of the National Academy of Sciences* 110.6 (2013), pp. 2011–2016.

[152] Trinschek, John, and Thiele. "From a thin film model for passive suspensions towards the description of osmotic biofilm spreading". In: (2016), pp. 1–22.

[153] Trinschek et al. "Continuous versus Arrested Spreading of Biofilms at Solid-Gas Interfaces: The Role of Surface Forces". In: *Physical Review Letters* 119.7 (2017), pp. 1–5.

[154] Ursell et al. "Motility Enhancement through Surface Modification Is Sufficient for Cyanobacterial Community Organization during Phototaxis". In: *PLOS Computational Biology* 9.9 (Sept. 2013), e1003205.

[155] Vallet et al. "The chaperone/usher pathways of Pseudomonas aeruginosa: Identification of fimbrial gene clusters (cup) and their involvement in biofilm formation." In: *Science* 98.12 (June 2001), pp. 6911–6916.

[156] Valle et al. "SarA and not σB is essential for biofilm development by Staphylococcus aureus". In: *Molecular Microbiology* 48.4 (2003), pp. 1075–1087.

[157] *Vapor Pressure Osmometry (Paraphrased from the instructions for the Wescor Osmometer)*. http://panza.uchicago.edu/Phys.261/materials/Osmometer/. Accessed: 2019-06-22.

[158] Vert et al. "Terminology for biorelated polymers and applications (IUPAC Recommendations 2012)". In: *Pure Applied Chemistry* 84.2 (Jan. 2012), pp. 377–410.

[159] Vlamakis et al. "Control of cell fate by the formation of an architecturally complex bacterial community". In: *Genes and Development* 22.7 (2008), pp. 945–953.

[160] Vlamakis et al. "Sticking together: Building a biofilm the Bacillus subtilis way". In: *Nature Reviews Microbiology* 11.3 (2013), pp. 157–168.

[161] Wainright et al. "Monophyletic Origins of the Metazoa: An Evolutionary Link with Fungi". In: *Science New Series* 260 (5106 Jan. 1993), pp. 340–342.

[162] Wales. "Device for constant flow of liquids." In: *Science* 79.2059 (1934), pp. 545–546.

[163] Walters et al. "Contributions of Antibiotic Penetration, Oxygen Limitation, and Low Metabolic Activity to Tolerance of Pseudomonas aeruginosa Biofilms to Ciprofloxacin and Tobramycin". In: *Antimicrobial Agents and Chemotherapy* 47.1 (2003), pp. 317–323.

[164] Wang and Zhang. "Review of mathematical models for biofilms". In: *Solid State Communications* 150 (21-22 2010), pp. 1009–1022.

[165] Watnick and Kolter. "Steps in the development of a Vibrio cholerae El Tor biofilm." In: *Molecular Microbiology* 34.3 (Nov. 1999), pp. 586–595.

[166] Watnick et al. "The absence of a flagellum leads to altered colony morphology, biofilm development and virulence in Vibrio cholerae O139". In: *Molecular Microbiology* 39.2 (2001), pp. 223–235.

[167] Webster, Davey, and Ingold. "Origin of the liquid in Buller's drop". In: *Transactions of the British Mycological Society* 83.3 (1984), pp. 524–527.

[168] Webster, Davey, and Turner. "Vapour as the source of water in Buller's drop". In: *Mycological Research* 93.3 (1989), pp. 297–302.

[169] Webster and Weber. *Introduction to Fungi. Third edition*. Cambridge University Press, 2007.

[170] Webster et al. "Mannitol and hexoses are components of Buller's drop". In: *Mycological Research* 99.7 (1995), pp. 833–838.

[171] Whitchurch et al. "Extracellular DNA Required for Bacterial Biofilm Formation". In: *Science* 295.5559 (Feb. 2002), p. 1487.

[172] Whittaker. "New concepts of kingdoms of organisms". In: *Science* 74 (Jan. 1969), pp. 150–160.

[173] Whytock and Finch. "The substructure of agarose gels as prepared for electrophoresis". In: *Biopolymers* 31.9 (1991), pp. 1025–1028.

[174] Wilking et al. "Biofilms as complex fluids". In: *MRS Bulletin* 36.5 (2011), pp. 385–391.

[175] Wright, Seed, and Hultgren. "Development of intracellular bacterial communities of uropathogenic Escherichia coli depends on type 1 pili." In: *Cellular Microbiology* 9.9 (Sept. 2007), pp. 2230–2241.

[176] Xiong et al. "Topology Evolution and Gelation Mechanism of Agarose Gel". In: *The Journal of Physical Chemistry B* 109.12 (2005), pp. 5638–5643.

[177] Xu et al. "Spatial physiological heterogeneity in Pseudomonas aeruginosa biofilm is determined by oxygen availability". In: *Applied and Environmental Microbiology* 64.10 (1998), pp. 4035–4039.

[178] Yan et al. "Extracellular-matrix-mediated osmotic pressure drives Vibrio cholerae biofilm expansion and cheater exclusion." In: *Nature Communications* 8.327 (2017).

[179] Yildiz and Schoolnik. "Vibrio cholerae O1 El Tor: Identification of a gene cluster required for the rugose colony type, exopolysaccharide production, chlorine resistance, and biofilm formation". In: *Proceedings of the National Academy of Sciences* 96.7 (1999), pp. 4028–4033.

[180] Zack, Rogers, and Latt. "Automatic measurement of sister chromatid exchange frequency." In: *J Histochem Cytochem.* 25.7 (July 1977), pp. 741–753.

[181] Zaldivar, Nielsen, and Olsson. "Fuel ethanol production from lignocellulose: a challenge for metabolic engineering and process integration". In: *Applied Microbiology and Biotechnology* 56.1–2 (2001), pp. 17–34.

[182] Zhao et al. "Psl trails guide exploration and microcolony formation in early P. aeruginosa biofilms". In: *Nature* 497.7449 (May 2013), pp. 388–391.

[183] Zogaj et al. "The multicellular morphotypes of Salmonella typhimurium and Escherichia coli produce cellulose as the second component of the extracellular matrix." In: *Molecular Microbiology* 39.6 (2001), pp. 1452–1463.

[184] Zottola and Sasahara. "Microbial biofilms in the food processing industry - Should they be a concern?" In: *International Journal of Food Microbiology* 23.2 (Oct. 1994), pp. 125–148.